Optical and Crystal Structure Characterizations of Nanowires for Infrared Applications

by

Minghua Sun

A Dissertation Presented in Partial Fulfillment
of the Requirements for the Degree
Doctor of Philosophy

Approved August 2011 by the
Graduate Supervisory Committee:

Cun-Zheng Ning, Chair
Hongbin Yu
Ray W. Carpenter
Shane Johnson

ARIZONA STATE UNIVERSITY

December 2011

ABSTRACT

Semiconductor nanowires (NWs) are one dimensional materials and have size quantization effect when the diameter is sufficiently small. They can serve as optical wave guides along the length direction and contain optically active gain at the same time. Due to these unique properties, NWs are now very promising and extensively studied for nanoscale optoelectronic applications. A systematic and comprehensive optical and microstructural study of several important infrared semiconductor NWs is presented in this thesis, which includes InAs, PbS, InGaAs, erbium chloride silicate and erbium silicate. Micro-photoluminescence (PL) and transmission electron microscope (TEM) were utilized in conjunction to characterize the optical and microstructure of these wires.

The focus of this thesis is on optical study of semiconductor NWs in the mid-infrared wavelengths. First, differently structured InAs NWs grown using various methods were characterized and compared. Three main PL peaks which are below, near and above InAs bandgap, respectively, were observed. The octadecylthiol self-assembled monolayer was employed to passivate the surface of InAs NWs to eliminate or reduce the effects of the surface states. The band-edge emission from wurtzite-structured NWs was completely recovered after passivation. The passivated NWs showed very good stability in air and under heat.

In the second part, mid-infrared optical study was conducted on PbS wires of subwavelength diameter and lasing was demonstrated under optical pumping. The PbS wires were grown on Si substrate using chemical vapor deposition and have a

rock-salt cubic structure. Single-mode lasing at the wavelength of ~3-4 μm was obtained from single as-grown PbS wire up to the temperature of 115 K.

PL characterization was also utilized to demonstrate the highest crystalline of the vertical arrays of InP and InGaAs/InP composition-graded heterostructure NWs made by a top-down fabrication method. TEM-related measurements were performed to study the crystal structures and elemental compositions of the Er-compound core-shell NWs. The core-shell NWs consist of an orthorhombic-structured erbium chloride silicate shell and a cubic-structured silicon core. These NWs provide unique Si-compatible materials with emission at 1.53 μm for optical communications and solid state lasers.

ACKNOWLEDGMENTS

I want to thank my advisor Prof. Cun-Zheng Ning, who has been helping me in my study and research during the past four years. Prof. Ning always has strong enthusiasm in science and he gave me very critical support for my research work. I benefited significantly from his deep understanding of semiconductor physics and optoelectronics. I appreciate all his contributions to make my Ph.D. experience very productive and stimulating. I not only obtained a lot of experience in optics lab but also in electron microscope lab. The experience is very precious for my future career.

I enjoyed and benefited a lot from the continuous help and friendship of my colleagues in the Nanophotonics Group: Debin Li, Leijun Yin, Ding Kang, Zhicheng Liu, Patricia Nichols, Derek Caselli, Sunay Turkdogan, Dr. Hua Wang, Dr. Ruibin Liu, Dr. Anlian Pan, Dr. Eunice Sok ping Leong, and Dr. Martin Hill. I appreciate their support, numerous discussions, and valuable comments. Especially, Leijun and Zhicheng helped me a lot in the optics lab; Debin discussed numerous theoretical problems with me; Patricia Nichol prepared samples for my PL experiments; Hua taught me a lot in EBL operation.

I benefited significantly from the strong faculty members and kind staff in LeRoy Eyring Center for Solid State Science. I would like to express my appreciation for Prof. Ray W. Carpenter and Prof. David Smith. They are always very patient to answer all my questions on TEM no matter how trivial the questions are. I would also like to thank Dr. Zhenquan Liu, who taught me to operate JOEL 2010F TEM machine and provided many helps to me in my study

and research. Many thanks to David Wright who helped me a lot in InAs NW passivation experiments. I want to gratefully acknowledge the use of facilities in Center for Solid State Electronics Research and LeRoy Eyring Center for Solid State.

For this dissertation, I would like to thank my defense committee members: Cun-Zheng Ning, Hongbin Yu, Ray W. Carpenter, Shane Johnson, for their time, interest and supports.

Lastly, I wish to thank my parents and my brother for their love and encouragement through my life. I am also very grateful to my beloved, supportive and encouraging boyfriend Xiaobo Zhang. He has been supporting and encouraging me during my Ph. D study and helped me a lot in modifying this thesis.

TABLE OF CONTENTS

TABLE OF FIGURES

Figure Page

LIST OF TABLES

CHAPTER 1

INTRODUCTION

Nanophotonics is a multi-disciplinary frontier research, dealing with nanoscale optical process, optical field confinement, and light-matter interaction. Recently, much attention has been paid to preparing nanostructured optical materials, studying nanoscale optical interactions, and fabricating nanoscale optical functional devices such as lasers, solar cells, detectors, waveguides, and sensors. Top-down[1] and bottom-up[2] are two philosophically distinct approaches for the fabrication of nanoscale optical devices. In the top-down approach, small features are fabricated by a combination of lithography, etching and deposition to make devices and integrated systems. The top-down method is often used for large scale fabrication and can produce very complicated structures. In the bottom-up approach, functional structures are assembled from well-defined, chemically or physically synthesized building blocks. To utilize this bottom-up approach, three key research areas are required and developed.[3] Firstly, precisely controlled nanoscale building blocks are needed, which should possess tunable chemical compositions, structures, sizes, and morphologies; secondly, it is critical to develop and explore the limits of the functional devices based on these building blocks; thirdly, high-density integration with predictable functions needs to be achieved. So it is very important to obtain high-quality nanostructure materials such as zero-dimensional nanodots and one-dimensional nanowires (NWs) for both of the approaches. Semiconductor NWs have been successfully used to fabricate electrical interconnects[4] and nanodevices including field-effect

transistors,[5, 6] solar cells,[7, 8] complementary metal oxide semiconductor (CMOS),[9] sensors,[10, 11] superlattice,[12] lasers,[13, 14] detectors,[15, 16] logic gates and computation circuits & memories.[17, 18, 19] On the other hand, the fabricated NWs need to be characterized to determine their crystal quality and optical properties for optoelectronic device applications. High-quality single crystal NWs are indispensable for making efficient optical devices. Accordingly, advanced and accurate characterization tools are required. Take InAs and PbS NWs for example. They are both narrow-band-gap (0.354 eV for InAs and 0.4 eV for PbS at 295 K) semiconductors with direct bandgaps. These two materials are very promising for making mid-infrared (MIR) optoelectronic nanodevices. Photoluminescence (PL) spectroscopy is a very effective method to provide a wealth of information including bandgap, defect states, radiative efficiency, carrier densities, impurity levels, recombination mechanisms, and composition of ternary or quaternary alloys. However, to our knowledge, there have been no reports on systematic and comprehensive PL characterizations for these two NW materials, due to the weak PL signal output associated with narrow-band-gap semiconductors, a lack of high-efficiency PL measurement system, or the difficulties to obtain high-quality NWs. Micro-PL will be the prime characterization tool for different kinds of infrared NWs in this thesis.

Besides PL, other powerful characterization methods will also be discussed in this thesis. Raman scattering spectroscopy is another important optical characterization method, which can provide important information about element composition, crystal structure, crystal quality, bonding effects, and material strain.

Transmission Electron Microscopy (TEM) is a very powerful tool for microstrctural and elemental characterization. It mainly includes three techniques: imaging, diffraction and microanalysis. Nowadays, with the help of aberration correctors, the resolution of high-resolution TEM (HRTEM) imaging can reach below one angstrom, which can uncover a lot of crystal structure details. The selected area electron diffraction pattern (SAED) taken by TEM can help determine the crystal structure of nanostructure. Energy dispersive X-ray spectroscopy (EDX) equipped in TEM is a useful elemental analysis tool for nanostructures. In my work, all these characterization methods will be utilized together to study in depth the optical properties and the associated crystal structures of several infrared NWs including InAs, PbS, InGaAs/InP composition-graded heterostructure, erbium chloride silicate/Si and erbium silicate/Si core-shell NWs.

1.1 Physical properties of nanowires

NWs have a one-dimensional structure and have unique size-dependent electronic and optical properties associated with low dimensionality and quantum confinement effects, especially when the size is smaller than the Bohr radii of the corresponding materials. Numerous methods have been applied to synthesize high-quality NWs, including vapor-liquid-solid (VLS), chemical vapor-phase deposition (CVD), metal-organic chemical vapor deposition (MOCVD), pulsed laser ablation (PLD), and molecular beam epitaxy (MBE).[23-28]

Semiconductor NWs have many novel properties compared to their bulk counterpart. Quantum confinement is one of their most important properties.[29] Bohr radius provides an approximate critical dimension for the onset of quantum-confinement effects. When an electron-hole pair is squeezed into a nanostructure that has one or more dimensions approaching the bulk exciton Bohr radius, the effective bandgap will increase. In general, the smaller the size is, the larger the effective bandgap is. The magnitude of quantum confinement is known to depend on the size, shape and composition of the nanocrystal. Polarization dependence of light emission intensity is another important property of NWs. For example, the InP NWs showed very high PL polarization dependence.[30] The PL intensity showed a maximum for polarization parallel to the length direction of the NWs. This polarization anisotropy is caused by the sharp dielectric contrast between a NW and its surroundings, which is very promising for making polarization-sensitive photo-detectors.

Semiconductor NWs are very promising materials for nanolaser fabrication because they can serve as both waveguide and gain media at the same time. The end facets of the NWs provide natural optical reflectors.[31] NWs have many advantages compared to their thin-film counterparts, such as one-dimensional geometry, high-quality single-crystalline, high refractive index, high end-facet reflectivity[31] and strong photon confinement. Optically pumped laser emission has been obtained from many semiconductor NWs, including ZnO,[14, 32, 33, 34] ZnS,[35] CdS,[13, 36] GaN,[37, 38] GaSb,[39] CdSe,[40] InGaAs.[41] Amplified spontaneous emissions can change to laser oscillation when cavity round-trip gain equals the round-trip

losses. The scattering losses at the end facets are dominated in NWs, which are caused by scattering. Part of the optical field can extend outside the NWs when their diameters are smaller than the wavelength of the emission light.[31] The following process shows the transition from spontaneous emission to laser oscillation emission. Before the excitation intensity reaches the threshold, the spectrum is broad and the light is emitted isotropically along the NW. In this regime, spontaneous emission is dominant, so the output intensity depends linearly on the excitation intensity. With further increase of the pumping level, a sharp peak will appear above the broad band emission. This means the population inversion starts to build up and meanwhile amplified spontaneous emission begins. In this regime, the PL intensity exhibits a superlinear increase with excitation intensity, which means the laser threshold is approached. When the pump power is further increased, sharp emission lines with intensity that is several orders of magnitude larger than spontaneous emission background will dominate the PL spectra. In this regime, the output intensity depends linearly on pump laser power.

1.2 Optical characterization methods

1.2.1 Photoluminescence spectroscopy

Photoluminescence contains two processes, one is optical excitation and the other is luminescence. A photon (usually produced by laser) is absorbed by the semiconductor during the optical excitation process, creating an electron-hole pair. This e-h pair then recombines and emits another photon during the luminescence process. The energy of emitted photon is determined by the band structure of the

semiconductor which is generally different from the energy of the absorbed photon. PL spectroscopy is a contactless and nondestructive technique for studying the optical and electronic properties of semiconductors. It provides direct information about recombination and relaxation processes. The recombination can be divided into two processes: radiative and nonradiative processes. In radiative process, a photon is emitted, while in nonradiative process, either a phonon or a long-wavelength photon together with a phonon, will be emitted, which reduce the luminescence efficiency of optoelectronic devices.

The most important generation and recombination processes include: optical generation/recombination (optical transitions), Shockley-Read-Hall generation/recombination (phonon transition), Auger generation/recombination (three particle transitions) and impact ionization. The photon transition is a direct generation or recombination process from one energy band to another energy band. In the band-to-band-recombination process, an electron from the conduction band falls back to the valence-band and releases its energy in the form of a photon. In the generation process, an electron-hole pair is generated by absorbing a photon which excites a valence band electron to the conduction band leaving a hole behind. The photon energy for this process needs to be higher or equal to the energy of the bandgap. Several fundamental optical transitions including conduction band to valence band, donor to valence band, conduction band to acceptor band, and donor to acceptor are shown in Fig. 1.1.

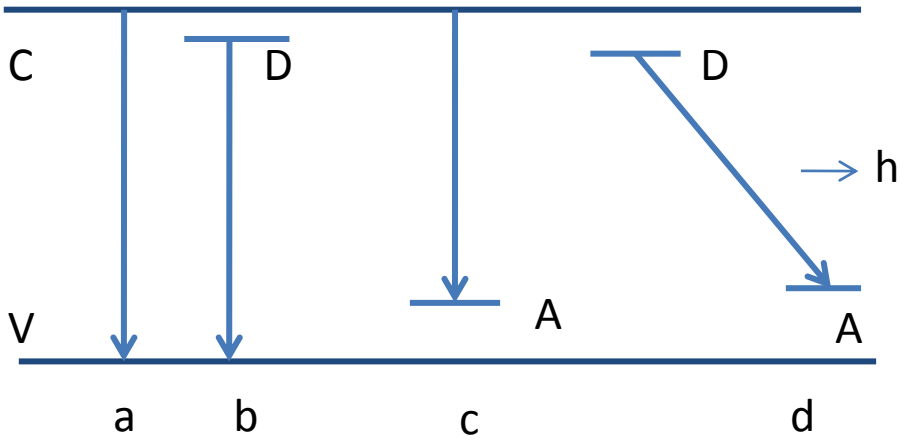

FIG. 1.1 Four kinds of different optical transition mechanism for recombination (a) Direct transition. (b) Donor-to-valence-band transition. (c) Conduction-band-to-acceptor transition. (d) Donor-acceptor-pair transition.

The most important recombination processes are summarized in the following:

(1) Exciton recombination

In a sufficiently pure material and at temperature $kT < E_x$, (k is the Boltzmann constant, T is temperature, and E_x is exciton bonding energy), the electrons and holes will pair into excitons which then recombine and produce a narrow spectral emission line. The energy of the emitted photon (hν) in direct-band-gap material is equal to $E_g - E_x$, where E_g is bandgap. Exciton has a series of excited states with ionization energy $(1/n^2)\ E_{x1}$, where n is integer and E_{x1} is the ground state corresponding to n=1. Hence, the free-exciton emission consists of a series of narrow lines with energy $E_g - (1/n^2)\ E_{x1}$ and the intensity decreases rapidly as n^{-3}. In indirect-band-gap material, the energy of emitted photon is $E_g - E_x - E_p$, where E_p is the energy of the phonon involved to satisfy momentum and energy

conversation law during optical transition. A direct transition can also occur by emitting one or more optical phonons but the transition probability is much lower.

The bound excitons can also be obtained in the presence of impurities. They produce a narrow PL emission peak with a lower energy than that of the free excitons and they often occur simultaneously with free excitons. With the increase of temperature, the exciton density will decrease due to the thermal ionization and accordingly the electrical conductivity of the material will increase. The temperature dependence of the emission intensity of bound excitons obeys the following equation:

$$\frac{L(T)}{L(0)} = \frac{1}{1 + CT^{-2/3}\exp(-\frac{E_i}{kT})},$$

where E_i is ionization energy and is equal to the sum of free-exciton binding energy and the additional energy binding free exciton to the center.

(2) Conduction-band-to-valence-band transition

In direct-band-gap materials, the recombination occurs between the states with the same k-value to satisfy momentum conservation. If the recombination occurs by generating a photon with the same frequency, propagation direction and phase as the stimulating photon, it is called stimulated emission. If the generated photons propagate in random directions and phases, it is called spontaneous emission. The spontaneous emission rate per unit volume per unit energy interval ($S^{-1}cm^{-3}eV^{-1}$) is given by

$$R^{sp}(E = \eta\omega) = \frac{8\pi n_r^2 E^2}{h^3 c^2} C_0 \frac{2}{V} \sum_{ka} \sum_{kb} \left| \hat{e} \cdot \vec{p}_{ba} \right|^2 \delta(E_b - E_a - E) f_b (1 - f_a)$$

and the net stimulated emission rate per unit volume per energy interval is given by

$$R^{stim}(E=\eta\omega)=\frac{8\pi n_r^2 E^2}{h^3 c^2} C_0 \frac{2}{V}\sum_{ka}\sum_{kb}\left|\hat{e}\cdot\vec{p}_{ba}\right|^2 \delta(E_b-E_a-E)(f_b-f_a),$$

where $\vec{p}$ is the momentum matrix element; f_b and f_a are Fermi-Dirac distributions of initial and final state, respectively; E_b is the energy of initial state; E_a is the energy of finial state.

In indirect-band-gap semiconductor, the transition needs to be mediated by an intermediate process to conserve momentum. Phonon emission or absorption is the most likely intermediate process. The shape of the emission spectrum can be affected by self-absorption. Assume the recombination occurs uniformly inside of the material, the radiated spectrum in one direction is

$$L(\nu)=(1-R)\frac{L_0(\nu)}{t}\int_0^t e^{-\alpha x}dx,$$

where R is exit surface reflectance, α is absorption coefficient, t is the thickness of the material.

(3) Transition between an energy band and an impurity level

In direct-band-gap semiconductor, deep transitions include a conduction-band-to-acceptor transition which produces emission peak at $h\nu=E_g-E_A$ and a donor-to-valence-band transition which produces emission peak at $h\nu=E_g-E_D$, where E_A and E_D are acceptor ionization energy and donor ionization energy respectively. Usually, the donor ionization energy is lower than the acceptor ionization energy, because the electron has smaller effective mass than the hole in

most semiconductors. In this case, the energy of the emission peak is often a function of the impurity concentration. Very deep levels in the band gap will be formed when the impurities have large ionization energies.

(4) Donor-acceptor-pair (DAP) recombination

If an electron is located at the donor level and a hole is located at the acceptor level, they can recombine by photon emission or phonon absorption if their wave functions overlap. After recombination, the donor has a positive effective charge and the acceptor has a negative effective charge and therefore, there is Coulomb interaction between them. So the photon energy produced in DAP emission is

$$h\omega_{DA} = E_g - E_D - E_A + \frac{e^2}{4\pi\varepsilon\varepsilon_0 r_{DA}} - mh\omega_{LO}$$

where r_{DA} is the distance between the donor and acceptor in the e-h pair, which reflects the Coulomb energy of the ionized centers after recombination. This coulomb-interaction term may push the donor and acceptor levels out of the energy gap. The last term is longitudinal optical (LO) phonon replica. When r_{DA} is small, the pairs give rise to sharp and discrete lines. When r_{DA} is large, the discrete lines merge together to form continuum and broad bands. This DAP recombination located inside the intrinsic band is usually strong enough to compete with conduction-to-valence-band recombination. An important characteristics of DAP emission is that these peaks shift toward higher energy with the increase of excitation intensity.

To get a deep understanding of these recombination mechanisms in semiconductors, PL measurements including low-temperature, temperature- and excitation-intensity-dependence are very useful.

(1) Low-temperature and temperature-dependent PL

An optoelectronic device usually operates over some temperature ranges, so it is critical to understand the temperature-dependent PL properties of the semiconductor. As we know, bandgap depends on temperature because of thermal expansion of crystal lattice. As the temperature of a semiconductor increases, the crystal lattice expands and the oscillation magnitude of the atoms about their equilibrium lattice points increases. This dilation of inter-atomic spacing leads to smaller energy gap, which causes band-edge emission peak shift to lower energy at higher temperature. In addition, the increased motion of atoms makes the energy level broader. This effect can be quantified by the linear expansion coefficient of a material. The temperature dependence of the bandgap can be fitted by the empirical Varshni Formula.[30]

$$E_g(T) = E_g(0) - \frac{\alpha T^2}{T + \beta}$$

where $E_g(0)$ is the bandgap value at 0 K, α and β are constants corresponding to different materials. A host of different processes might contribute to the changes of the PL features versus the increase of temperature such as thermal release of trapped carriers, followed by capture in a nonradiative recombination. Temperature dependence of the integrated intensity I (T) of PL peaks is often described using the following equation:

$$I(T) = \frac{I_0}{1 + \alpha \exp(-E_T / kT)}$$

where α is the radiative rate parameter, T is temperature, and E_T is the activation energy. By fitting the integrated intensity obtained from the experimental measurements with this equation, one can get the value of E_T, which indicates the mid-band-gap energy level contributing to the light emission.

Another dominant effect of temperature is the change of carrier population of conduction and valence bands. Large concentration of free carriers results in screened coulomb interaction between carriers, which perturbs the band edge and induces a "tail" of the band states into the energy gap. Low-temperature PL spectrum features can provide more information about mid-gap energy levels corresponding to excitons bound to specific impurities, or other transitions such as free-to-bound or DAP recombination. Exciton-related emission can only be observed when the thermal energy is lower than the exciton binding energy ($kT < E_x$).

The temperature-dependent PL spectrum from a semiconductor can help determine the bandgap, recombination mechanisms, and elemental composition of alloy semiconductors. Impurities and defects strongly affect material quality and device performance. Growth methods and preparation conditions strongly affect optical properties of NWs in terms of emission intensity, spectral width, peak position, and the presence of long wavelength components from impurity states that produce radiative emission. Thus PL, especially low-temperature PL spectrum is a very sensitive method for impurity identification. The NW materials

with narrow and pure PL spectra are extremely critical for making high-efficiency photoelectronic devices.

(2) Excitation-intensity-dependent PL

Some underlying recombination mechanisms can be identified from excitation-intensity- dependent PL measurements. The power-dependent PL intensity can be described by the empirical formula[43]: $I \sim L^k$ (L is varied over a range of less than two orders of magnitude), where I is the luminescence intensity, L is excitation laser intensity, and k is the scaling index , usually $1< k < 2$ for the free- and bound-exciton emissions, when excitation laser has energy exceeding bandgap of the material; $k < 1$ for free-to-bound and DAP recombination; k is equal to 1 for the free exciton emission when excitation laser has the same energy with bandgap. The nonlinear behavior of the bound-exciton emission intensity is due to the increase of the population of neutral impurities by photo-excited carriers, so it often suggests an impurity related origin. A rapid quenching of the peak intensity with the increase of temperature and the rapid saturation with the increase of excitation density imply a transition involving an impurity or defect. In the case of free electrons recombining with acceptors, such dramatic temperature dependence cannot be expected.

1.2.2 Raman scattering spectroscopy

Raman scattering spectroscopy is a very useful, fast, and nondestructive semiconductor characterization tool with rich information about element composition, crystal structure, crystal quality, bonding effects, environment and stress of the material. For alloy semiconductors, the phonon modes can provide

critical information about alloy composition and crystallinity. Moreover, phonon frequencies and scattering intensities, determined by Raman spectroscopy, provide important information about microscopic parameters such as lattice structure or the presence of structural defects.

When monochromatic radiation is incident onto a material, it may be reflected, absorbed, or scattered. As shown in Fig. 1.2, there are two possible scattering mechanisms: Rayleigh scattering that has no energy change and Raman scattering that has energy change. In the case of Raman scattering, if the material absorbs energy, it is Stokes scattering; if the material loses energy, it is anti-Stokes scattering. Raman spectrum is generally plotted in terms of wavenumber. So the Raman shift can be expressed using the following formula:

$$\Delta k = (\frac{1}{\lambda_0} - \frac{1}{\lambda_1}),$$

where Δk is the Raman shift in wavenumber and the units is cm^{-1}, λ_0 is the excitation wavelength, and λ_1 is the Raman spectrum wavelength.

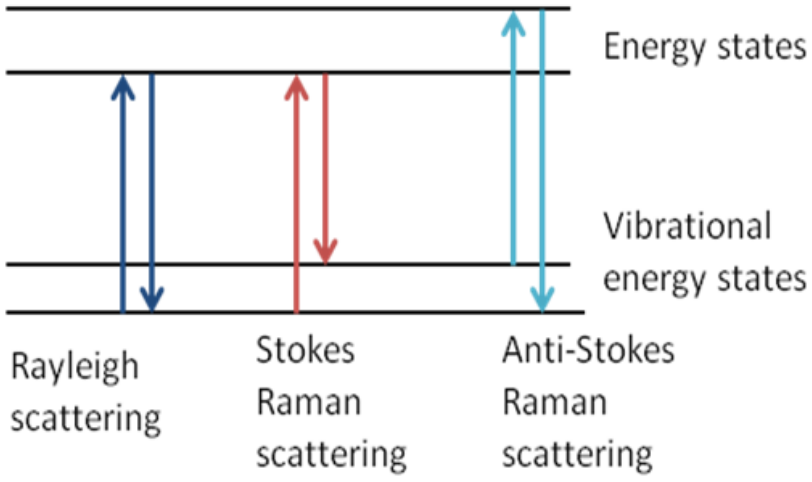

FIG. 1.2 Energy level diagram showing three kinds of Raman scattering mechanisms.

The Raman spectrum is closely related to the crystal structure. Damaged and defective crystal has poor Raman signal (lower intensity, broad peaks etc). Different arrangements of constituent atoms usually give very different Raman spectra. The reason could be a decrease of the phonon lifetime or relaxation of momentum conservation in Raman scattering. Non-uniform stress arising from external forces or non-uniform temperature distribution within the spot of the probe laser beam may also cause inhomogeneous broadening. The plasmon-LO-phonon coupled modes show asymmetric line shapes, which reveals some information of carrier concentration and mobility.

The anisotropy of the Raman scattering intensity depends on the polarization of the incident and scattered light relative to the crystal axes as shown in the formula: $I \sim \left| \hat{e}_i \cdot R \cdot \hat{e}_s \right|^2$, in which $\hat{e}_i$, $\hat{e}_s$ are unit vectors, giving the directions of the incident and scattered electric field respectively; R is the Raman tensor which carries the geometric information about the crystal. This law determines which

phonon modes are allowed or forbidden for different orientations. These selection rules could be broken if the crystal quality is bad. Polarization rules hold exactly for off-resonant conditions in perfect crystals and break down in imperfect crystals containing disorder and randomly oriented microcrystals. Therefore, relaxation of the selection rule provides information on disorder and imperfection in materials. The selection rule helps to determine the crystallographic orientations.

1.3 Basic semiconductor laser theories

1.3.1 The laser structure: optical cavity

The optical cavity is a resonator or resonant cavity in which the photons are reflected many times and the photon density is built up. Fabry-Perot resonator is the most widely used cavity for semiconductor lasers. It has two mirror surfaces which are made perfectly plane and parallel to produce resonant modes in the cavity. Standing wave modes can be formed in the cavity when photons propagate perpendicularly to the two plane facets. For cavity with length l, the condition to form the longitudinal mode is that the cavity length is an integral number of half-wavelength of the propagated photon, which can be expressed by $m\frac{\lambda}{2n} = l$ where n is the refractive index of the cavity, $\frac{\lambda}{n}$ is the wavelength of the radiation in the semiconductor and m is an integer. The spacing between modes is given by

$$\Delta\lambda = \frac{\lambda^2}{2l(n - \lambda\frac{dn}{d\lambda})}.$$

In addition to the longitudinal modes, transverse modes can also exist. The active region of cavity, where the electrons and holes recombine and light emission occurs, has a higher refractive index than the adjacent regions. The refractive index will be decreased in the cavity when the carrier density is increased. In fact, the active region may only occupy a small fraction of the optical cavity, which makes it important to make large fraction of optical wave overlap with the active region. Optical confinement factor Γ is the fraction of the optical intensity overlapping with the gain medium and gives the fraction of optical wave in the active region, which can be expressed as:

$$\Gamma = \frac{v_{ph}\iint_{active} w_e dxdy}{V_{E,z}\iint_{waveguide} dxdy(w_e + w_m)/2},$$

where v_{ph} is the phase velocity in the active medium; w_e and w_m are the stored electrical and magnetic energy of the field, respectively; v_E is the energy velocity of the waveguide.[44, 45]

1.3.2 Optical absorption, gain and loss

When an electromagnetic wave travels through a semiconductor, the optical intensity can be described as

$$I_{ph} = I_{ph}^0 \exp(-\alpha x)$$

where α is absorption coefficient and I_{ph}^0 is the incident optical intensity. When the semiconductor is electrically or optically pumped, electrons and holes will be

generated. Assuming quasi-equilibrium state, two quasi-Fermi levels, F_c and F_v for electrons and holes, can be used. So the absorption coefficient can be given as[46, 47]

$$\alpha(\eta\omega) = C_0(\hat{e}.p_{cv})^2 \int \frac{2d^3k}{(2\pi)^3} \delta(E_g + \frac{\eta^2 k^2}{2m_r} - \eta\omega)\left[f_v(k) - f_c(k)\right]$$

$$C_0 = \frac{\pi e^2}{n_r c \varepsilon_0 m_0{}^2 \omega}$$

$$f_v = \frac{1}{1+e^{(E_v(k)-F_v)/k_BT}}$$

$$f_c = \frac{1}{1+e^{(E_c(k)-F_c)/k_BT}}$$

where f_v and f_c are Fermi-Dirac distributions for electrons in the valance and conduction band, respectively. If $f_v(k) - f_c(k) < 0$, $\alpha(\hbar\omega)$ becomes negative, there will be gain in the medium, which can be given by $g(\hbar\omega) = -\alpha(\hbar\omega)$. Since $f_v(k) - f_c(k) < 0$, we can get $F_c - F_v > E_c - E_v = \hbar\omega$. This condition is called Bernard-Duraffourg inversion condition. If it holds, the population inversion condition is satisfied, absorption is negative and gain will be obtained. The gain here is called the material gain, which comes from the active region where recombination occurs. When the active region is of a small dimension, cavity gain will be defined. The cavity is equal to $g(\hbar\omega)\Gamma$, where Γ is optical confinement factor and $g(\hbar\omega)$ is the material gain.

In order to get laser oscillation, the gain associated with the cavity should be equal to the loss due to absorption. So the threshold condition is determined by

$$g_{th} = \alpha_i + \alpha_m$$

$$\alpha_i = \alpha_0 (1 - \Gamma) + \alpha_g \Gamma$$

$$\alpha_m = \frac{1}{2L} \ln \frac{1}{R_1 R_2}$$

where α_i is the intrinsic loss due to absorption inside the guide α_g and outside α_0, α_m is the loss at the two end facets. The gain will increase with the increase of the carrier density n. When the threshold condition is reached, the carrier concentration will be pinned at the threshold n_{th} and the gain will be pinned at the threshold g_{th}. So

$$n_{th} = n_{tr} + \frac{(\alpha_i + \alpha_m)}{a\Gamma},$$

where a is the differential gain and n_{tr} is a transparency concentration when gain is zero. The carrier lifetime τ_e when carrier density is equal to n_{th} is

$$\tau_e(n_{th}) = \frac{1}{A_{nr} + Bn_{th} + Cn_{th}^2},$$

where the first term is due to nonradiative processes, the second term is due to the spontaneous radiative recombination rate and the third term accounts for nonradiative Auger recombination. Below the threshold, the output light is mainly spontaneous emission and is governed by Bn^2. When the injected carrier density is increased above threshold, the stimulated emission will be obtained.

1.4 Morphology, crystal structure and element composition characterizations

1.4.1 Scanning electron microscope (SEM)

SEM is a type of electron microscope that images the sample surface by scanning it with a high-energy electron beam. When the electrons interact with the atoms of a sample, they will produce a series of signals that contain information about surface topography and composition of the sample. These signals include secondary electrons, back scattered electrons, transmitted electrons, characteristic x-rays, cathodoluminescence and electron-beam-induced current. They can be used to modulate the monitor intensity, build up a two-dimensional map of the near-surface topography, and analyze element composition and electrical conductivity. In the standard detection mode, SEM can produce high-resolution images of the sample surface using secondary electron imaging. The spatial resolution can reach about 1 to 5 nm. The SEM measurements in this thesis were carried out using field-emission environmental scanning electron microscope (ESEM-FEG XL30) from FEI Company. The ESEM-FEG XL30 utilizes Schottky field emission gun as source with an acceleration voltage of 30 kV. It offers a very high resolution of 3 nm in secondary electron imaging. The typical electron probe focused onto the specimen is around 2-50 nm. Compared to conventional high vacuum SEM, the ESEM-FEG XL30 has many advantages. It has very high resolution and excellent signal to noise ratio at pressure as high as 10 Torr and at temperature as high as 1000 ℃. This make it an outstanding tool to observe the

performance of potentially problematic samples, such as wet, oil, dirty, outgassing and non-conductive samples, without significant sample preparation.

1.4.2 Transmission electron microscope

TEM is another type of electron microscope that forms the images by a beam of electrons interacting with the ultra thin specimen as they transmit through it. A TEM consists of electron source and a series of electromagnetic lenses which can change their focal lengths by varying the current (Fig. 1.3). There are two main imaging systems in TEM: imaging mode and diffraction mode (Fig. 1.4). The sample holder lies in the front focal-plane of the objective lens. A magnified image was produced by the objective lens. Then it serves as an object of the diffraction lens and forms the second intermediate image, which is further magnified by a projector lens. The final image is projected on the fluorescent viewing system and displays on an imaging screen. This is the imaging mode. The TEM can be easily converted to diffraction mode by a console selection. When an electron beam passes through the crystalline lattice of very thin sample, it will undergo Bragg scattering. The diffraction pattern (DP) is formed by the dispersed electrons in the back focal plane of the objective lens. A lot of crystal structural information can be obtained through DP, including crystal lattice structure, lattice constant and crystal defects. The DP contains all the electrons from the whole specimen that the beam illuminates. The specimen is often buckled, which make the DP not useful. Furthermore, the direct beam is so intense that it can destroy the viewing screen. So a basic TEM operation is performed by selecting a specific area of the specimen to contribute to the DP and to reduce the pattern intensity.

This operation is called selected-area electron diffraction (SAED), in which a selected area aperture is used at the image plane of the objective lens and is centered around the optical axis of the objective lens. The SAED allows observation of DP from small areas of the samples. In this way, the crystallography of the sample will be well correlated to the diffraction pattern.

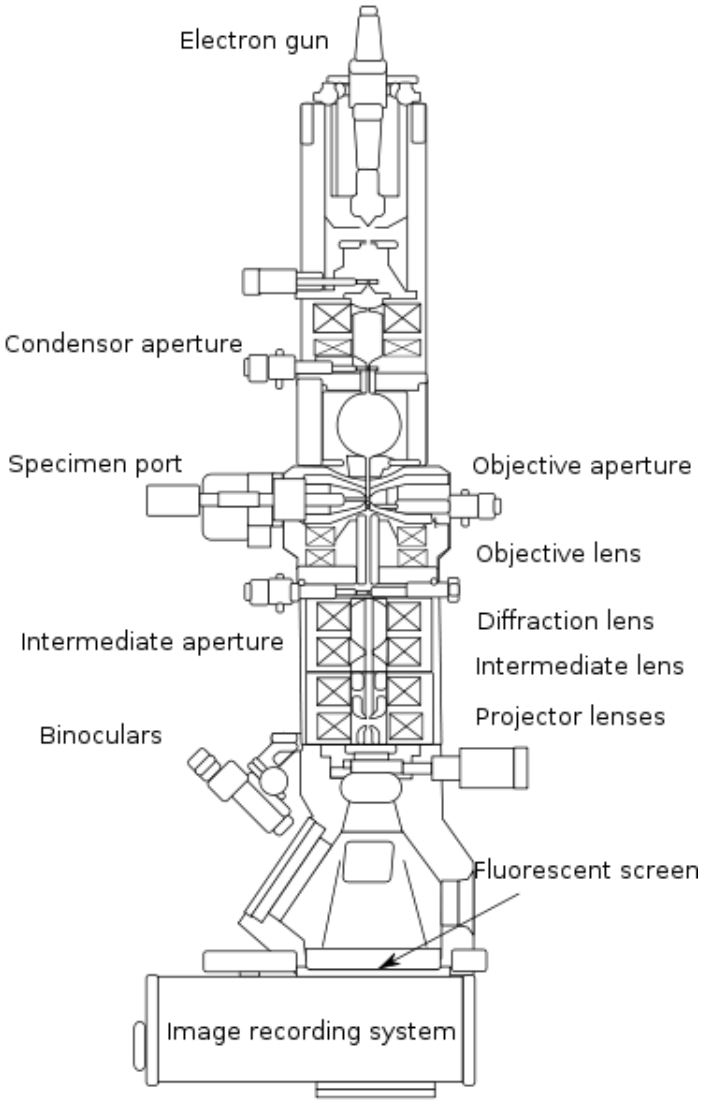

FIG. 1.3 Internal component diagram of a basic TEM system. (From Wikipedia）
http://en.wikipedia.org/wiki/Transmission_electron_microscopy

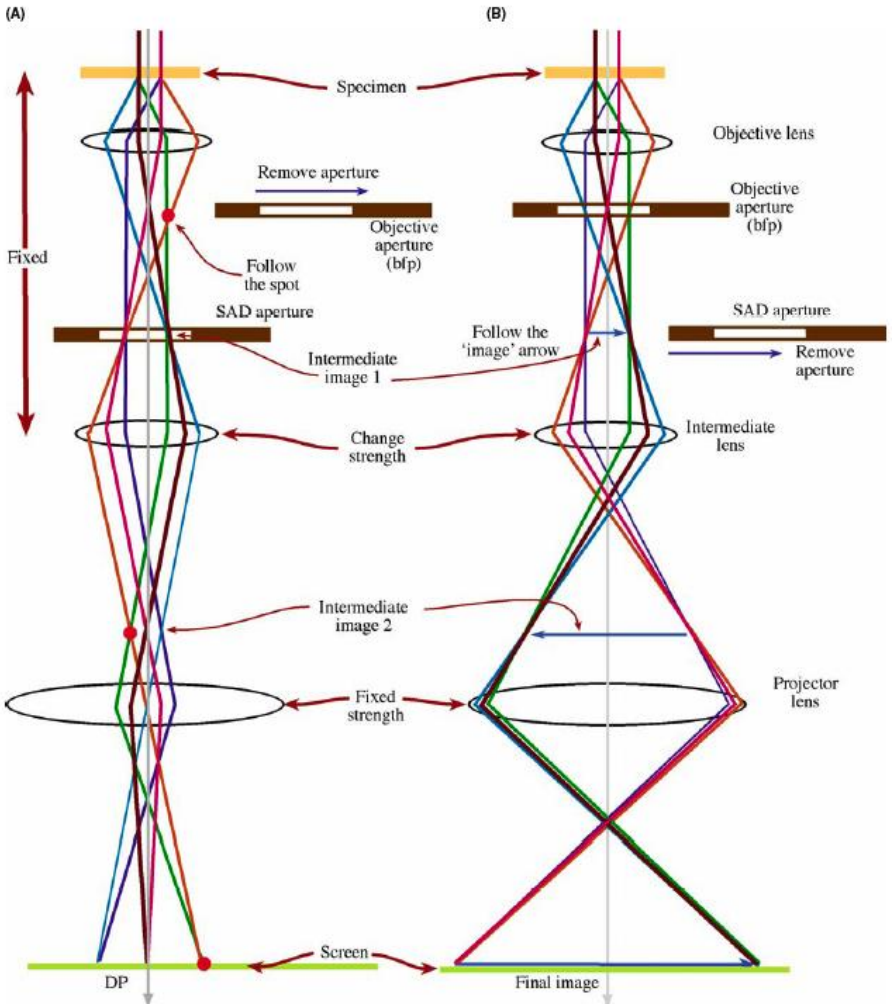

FIG. 1.4 Two basic operation modes of the TEM imaging system involve (A) diffraction mode: projecting the DP onto the viewing screen and (B) image mode: projecting the image onto the screen. In each case the intermediate lens selects either the back focal plane (A) or the image plane (B) of the objective lens as its object. The imaging systems shown here are highly simplified. Most TEMs have many more imaging lenses, which give greater flexibility in terms of magnification and focusing range for both images and DPs. The SAD and objective diaphragms are also shown appropriately inserted or retracted. Note: this is a highly simplified diagram showing only three lenses. Modern TEM columns have many more lenses in their imaging systems.[48]

There are two basic imaging operations in TEM: bright-field (BF) image and dark-field (DF), using the SAED pattern projected onto the viewing screen. Usually SAED pattern contains a bright central spot which consists of the direct electrons and some scattered electrons. The direct beam comes through the specimen parallel to the direction of the incident beam. A general TEM image is formed by inserting the objective aperture around the incident beam in the back focal-plane of the objective lens and then projecting the images onto the viewing screen. In this way, most of the diffracted beams will be excluded, which means only the central diffraction spot which consists of direct electrons is selected. So vacuum area will appear bright, the resultant image is called BF image. If the incident beam is blocked and only the electrons scattered outside the central spot of the DP are selected, the vacuum area will appear dark and resultant image is called DF image.

There are two TEM operation modes: TEM and STEM as shown in Fig. 1.5. In TEM mode, parallel electron beams are used in illumination system, which controls the convergence angle of the electron beam. In standard STEM mode, the beam is focused onto the specimen, which means the illumination system operates in convergent-beam mode and the images are formed by scanning beams. The process has the same principle as used in SEM. The scanning of the beam across the sample makes TEM a good microanalysis tool such as EDX and electron energy loss spectroscopy (EELS) element mapping. Because these signals can be obtained simultaneously with the images, a direct relationship of image and quantitative data will be built. The STEM mode can also be operated to obtain

atomic resolution images in the aid of high-angle detectors. The contrast of such images is directly determined by the atomic number, so it is called z-contrast image. One advantage of forming images by this way is that the lenses are not used. This avoids the aberration defects in the imaging lenses that affect the resolution of the image. However, in practice, the aberration of the STEM probe-forming lens limits its performance, thus the STEM images are usually nosier than TEM images, but they have larger contrast than TEM images. Creating STEM images is much slower than TEM ones because it is a serial instead of parallel recording. The DF images in STEM are formed by collecting most of the scattered electrons using annular dark field (ADF) detectors while DF images in TEM are formed by collecting a fraction of scattered electrons going through objective lens. Therefore, DF images in TEM mode have better resolution while DF images in STEM mode have better contrasts.

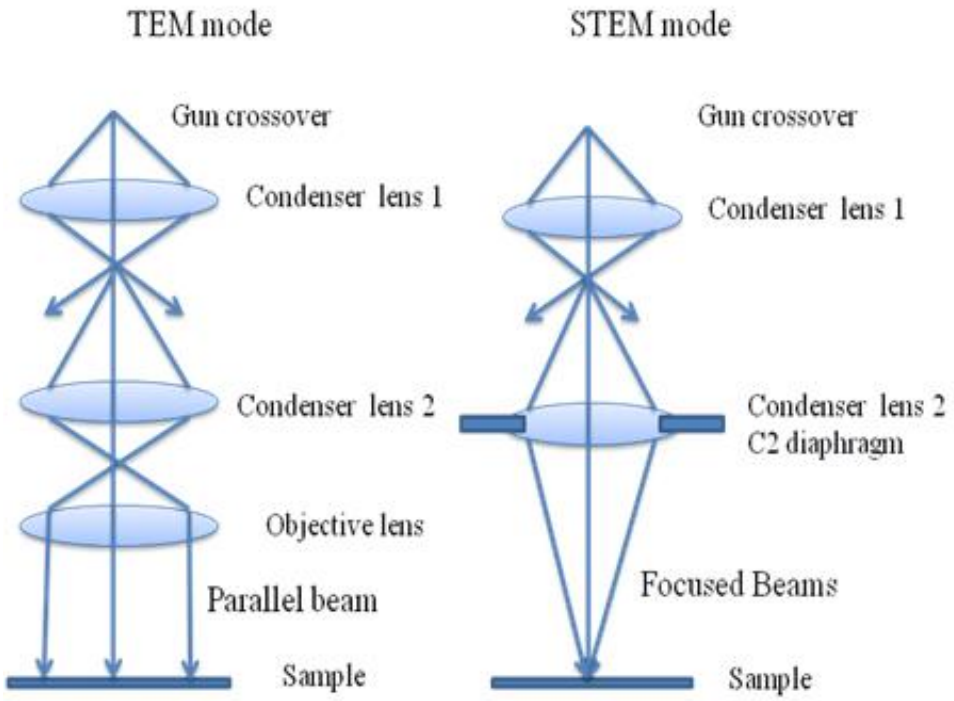

FIG. 1.5 Ray diagrams for TEM and STEM modes.

1.4.3 Energy dispersive X-ray spectroscopy (EDX) and electron energy loss spectroscopy (EELS)

EDX is a stable, compact and robust element analysis instrument and it is very easy to use and interpret. The typical EDX spectra are plots of X-ray counts versus X-ray energy. The principle scheme of EDX is shown in Fig. 1.6. When electrons penetrate through outer electron shells and interact with the core electrons, two kinds of X-rays are generated. One is characteristic X-ray caused by the ionization of atoms and the other is the continuous Bremsstrahlung X-ray produced by the interaction of high-energy electrons and nucleus. In the ionization process, an inner-shell (or core) electron is ejected from the atoms by the high-energy electron and a hole is left behind. Then an outer-shell electron will fill in this hole and emit an X-ray that has unique energy related to the ionized atom. Hence, the obtained EDX spectrum is the characteristic X-rays with Gaussian-shaped peaks superimposed on the Bremsstrahlung X-rays background.

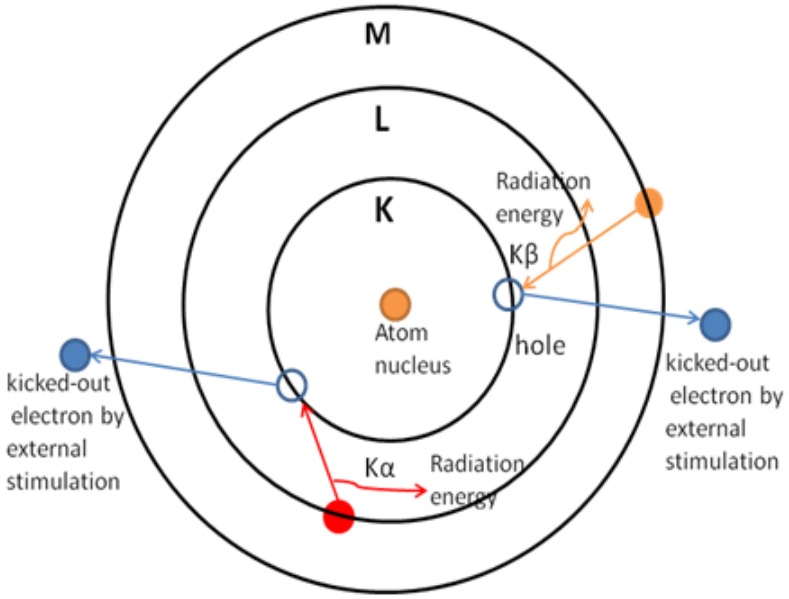

FIG. 1.6 Atomic energy level diagram for characteristic x-ray signal generation in EDX

When a high-energy electron beam with very narrow range of kinetic energies passes through a thin specimen, the electrons will be inelastic scattered or and lose their energies by a variety of processes. The EELS separates these inelastically scattered electrons into a spectrum, which can be interpreted and quantified. By detecting the energy loss in the inelastic electron-electron interaction, the EELS spectrum can provide information on atomic composition, chemical bonding, valence and conduction band electronic properties, surface properties, and element-specific pair distance distribution functions. Compared to EDX analysis, EELS works better at materials with relatively low atomic numbers. The principal inelastic interactions include phonon excitation, inter- and intra-band transition, plasmon excitations and inner-shell ionization. Therefore, the typical EELS spectrum consists of the following parts: zero-loss peak, low-loss

spectrum including plasmon, inter- and intra-band transition, and high-loss spectrum including inner-shell ionization. Some characteristic peaks in the energy loss of up to ~25 eV are produced when an electron in the excitation beam transfers sufficient energy to a core electron and changes its orbital states. This kind of low-loss spectrum can be used for phase identification by checking with the existing, complied collection of the low-loss spectra from all the elements stored in the computer. The high-loss spectrum above ~50 eV is produced by inner-shell ionization when an electron transfers sufficient energy to a K, L, M, N or O shell electron and moves it out of the attractive field of the nucleus. The ionized atom will decay back to its ground state by producing a characteristic X-ray or an Auger electron. The typical high-loss energy peak shows a sharp rise to a maximum at E_c, which is the minimum ionization energy, followed by a slowly decreasing intensity toward to the background.

Chemical microanalysis in TEM has two techniques including linescan and element mapping in STEM mode. “linescan in STEM” means displaying the distribution of an element or elements along a single line and “Mapping in STEM” means in two dimensions in an sample area of interest. Element mapping is one of the most important applications of STEM. Any signal conveying information such as EDX and EELS can be mapped. To do the mapping, a “window” is defined in an X-ray energy range which corresponds to a characteristic peak of an element. As the electron probe scan slowly across the specimen, a pulse will be produced and detected whenever an X-ray with energy in the defined window is detected by the X-ray analyzer. This is the process of element mapping in STEM. In fact,

many windows corresponding to the interested X-ray can be defined and the map of each window is stored separately. The probe will scan over an array of discrete points, pausing for a predefined time at each point. The counts number recorded in each window will be stored in the memory of computer. In this way, the maps for all the elements can be acquired simultaneously. Any other available signal, such as BF or ADF STEM images can also be obtained simultaneously. Sample drift and contamination built-up during the process are the two issues that require more attentions.[48]

CHAPTER 2

EXPERIMENT SETUPS

2.1 Micro-photoluminescence (PL) setups

We have three micro-PL setups in our lab aimed at different premium measurement wavelength ranges including ultraviolet (UV)/visible, near-infrared (NIR) and MIR. A schematic of the MIR micro-PL setup is shown in Fig. 2.1. The other two setups have similar constructions.

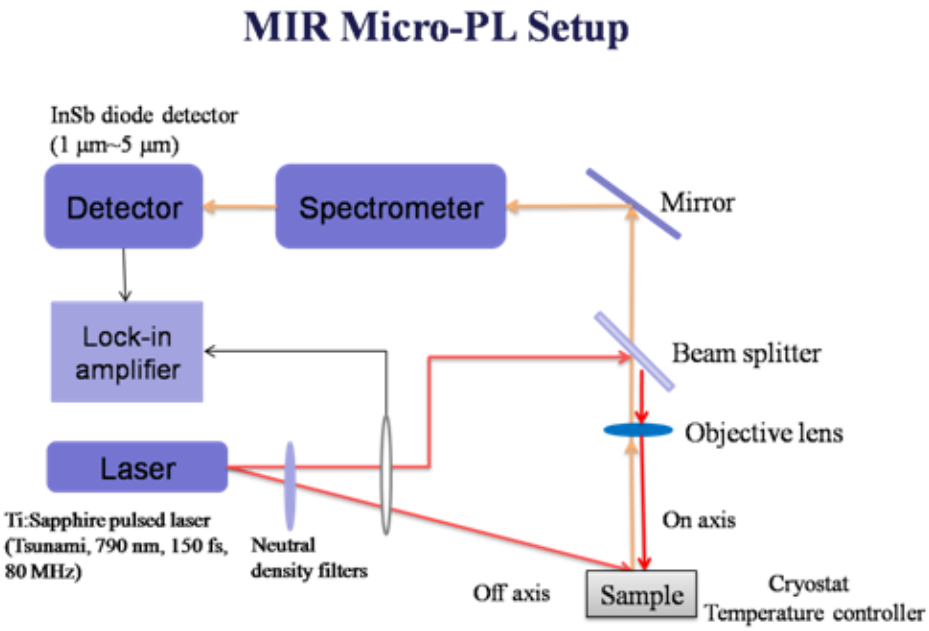

(a)

(b)

FIG. 2.1 The MIR micro-PL setup in our lab. There are two laser exciting modes: on axis and off axis as shown in the schematic (a) and also in the real picture (b).

The key components of a typical PL measurement system (based on the setups in our lab) include:

(1) Excitation sources - lasers

There are two laser sets together with a tripler system in our lab. One is Spectra-Physics mode-locked Ti:Sapphire pulsed laser system (Tsunami), which delivers a range of wavelength from 690 nm to 1080 nm and a range of pulse lengths continuously varying from 80 ps to 50 fs. It is operated at 790 nm, 150 fs, 80 MHz in my experiments. A tripler system is utilized to obtain the 2nd (~395 nm) and 3rd (~266 nm) harmonic pump wavelength source. There is also an optical parametric oscillator (OPO) that can be used to generate the wavelength of a few micrometers. The other is Quanta-Ray INDI pulsed Nd:YAG Laser. It is Q-switched, nanosecond, frequency quadrupled Nd:YAG pulsed laser and has built-in second, third, and fourth harmonic generators to generate ns-pulse laser sources at wavelengths: 1064 nm, 532 nm, 355 nm, and 266 nm.

(2) Detectors

Different kinds of detectors are necessary to cover different wavelength ranges. The InGaAs array detector cooled by liquid nitrogen is equipped for both NIR and MIR PL setups covering the wavelength range from 700 nm to 1800 nm. The InSb detector cooled by liquid nitrogen for MIR PL measurements can cover the wavelength range from 1 μm to 5 μm. The InSb detectors used in our lab are the IS series cryogenic photodiode/amplifier made by Electro-Optical systems Inc. A lock-in amplifier is connected with the InSb detector to reduce the noise in the PL signal. The laser beam is modulated by a chopper and the lock-in amplifier is

referenced to the laser chopper frequency to extract the modulated signal. A CCD open electrode detector is fixed in UV/visible PL setup, which can cover the wavelength range from 200 nm to 900 nm.

(3) Spectrometers

The PL signal is collected through an objective lens then collimated and focused into a slit on a spectrometer. The spectrometers used in our lab are the TRIAX series from JOBIN YVIN INC, which include an optional triple grating turret to satisfy different scan wavelength ranges. The three selectable gratings are 600 g/mm, 150 g/mm, and 300 g/mm for MIR and NIR setups and 2400 g/mm, 1200 g/mm, 300 g/mm for UV/visible setup.

(4) Delivery systems

To deliver laser beams to the samples and to collect the excited PL signal to spectrometer and detectors, much optics is needed such as mirror, lens and beam splitter. Because different optics has different absorption, transmission, and reflection efficiency, the three PL setups aimed at different wavelength ranges utilize different optics for premium performances. Take the selection of mirrors for example, silver protected mirrors which allow good reflection at the wavelength range of 0.45~12 μm are utilized for NIR system. The gold protected mirrors are good for MIR system and the aluminum protected mirrors are good for UV/visible setup.

As shown in Fig. 2.1, the excitation laser beam can be directed to the sample in two different directions. One is on-axis incidence or bright-field illumination, in which the laser beam is focused by a high-magnification objective lens and

delivered vertically onto the substrate surface. So it has very small probe size and very high power. The other is off-axis incidence or dark-field illumination, in which the laser beam is focused by a long focal-length lens and directed at an angle of around 45 °with respect to the substrate surface normal direction.

(5) Cryostat and temperature controller

The ST-500 Microscopy system cryostat made by Jenis Research Company together with a synchronous temperature controller is used to load samples for temperature-dependent PL measurements at temperatures ranging from 4 K to 400 K. Continuous liquid helium flow keeps temperature as low as 4 K and the heater in the temperature controller allows temperature to be as high as 500 K.

(6) Imaging systems

Very high resolution is required to measure small size nanostructures. So high-magnification objective lenses were utilized to help to locate the nanostructures and focus the collecting objective lens during PL measurements. A schematic of a typical imaging system in the micro-PL setups is shown in Fig. 2.2. A light source goes through all the MIR-fitted optics before illuminates the sample and then the reflected light is collected by the camera. The camera sends the image signal to the computer so we can immediately and clearly see the image of the sample in the computer.

Different objective lenses are used in different setups. For MIR setup, all-reflective objective lens (15×) is fixed and the spatial resolution is around 1.2 μm; For NIR setup, three Mitutoyo objective lenses (5×, NIR 50× and NIR 100×) with

spatial resolution around 1 μm are equipped; For UV/visible setup, a NUV 100× Mitutoyo objective lens with the spatial resolution of 1 μm is used.

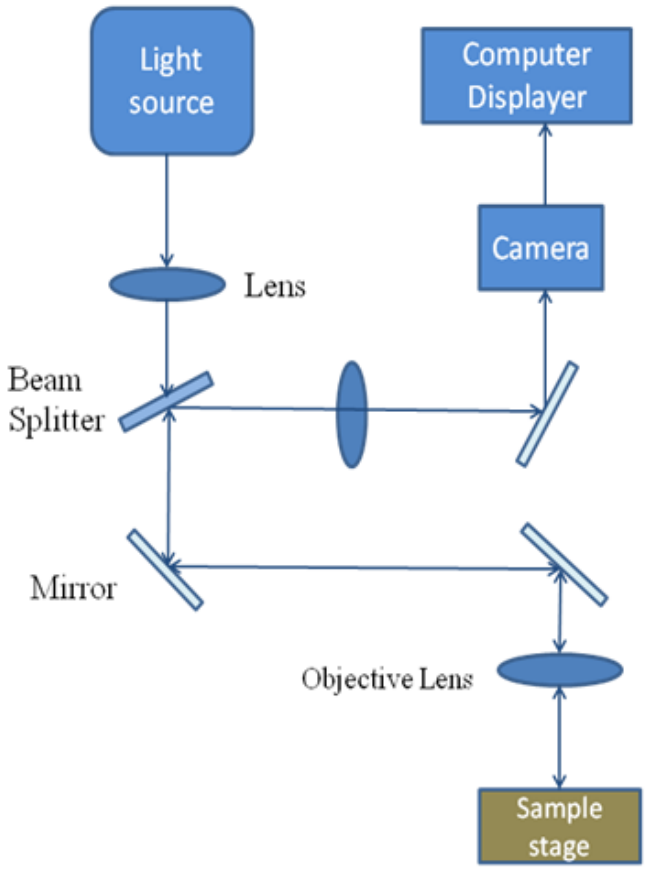

FIG. 2.2 A schematic diagram of imaging system in MIR micro-PL setup.

The PL measurements for narrow-band-gap semiconductors such as InAs NWs, PbS NWs and InGaAs/InP heterostructure NWs were performed using the MIR micro-PL setup illustrated in Fig. 2.1. The sample is loaded in the cryostat and then pumped to high vacuum if low-temperature measurements are needed. Then the cryostat is fixed onto a sample stage that allows very precise displacement control in three different directions. A temperature controller is connected with the cryostat to enable temperature-dependent PL measurements and some optical attenuators are added to modulate the incident laser power for excitation-intensity-dependent PL measurements. The excitation laser beam is directed to the sample in the form of on-axis or off-axis illumination. The PL light emission is collected along the substrate normal direction by an objective lens and then directed to the TRIAX series spectrometer and the corresponding detectors. Both liquid nitrogen cooled InGaAs and InSb detectors are equipped in this setup. An optical chopper in the excitation laser beam and a lock-in amplifier connected to the InSb photodiode were used to suppress detector noise. Compressed nitrogen gas is used to purge the PL light path to reduce water and air absorption if needed.

2.2 Micro-Raman scattering setup

A schematic of the Micro-Raman scattering setup is shown in Fig. 2.3, which consists of the following components:

(1) Excited monochromatic laser

Diode pumped single-frequency CW 532 green laser is used to excite sample.

(2) Optical microscope

A Mitutoyo objective lens (×50) is fixed into the system to collect the Raman spectra from a very small volume (1 μm) for NW measurements. The imaging system introduced above is also incorporated into the system to locate the samples and bring the objective lens in focus.

(3) High-resolution spectrometer and high sensitivity detector

The high-resolution TRIAX series spectrometer from JOBIN YVIN INC and liquid nitrogen cooled open electrode CCD detector are equipped in the setup.

(4) Holographic notch filter

The holographic notch filter is very important for Raman spectroscopy, which helps to reject all the unwanted lights including laser light, Rayleigh scattering light, stray lights and fluorescence light. Those unwanted peaks are very strong and close to the Raman peaks.

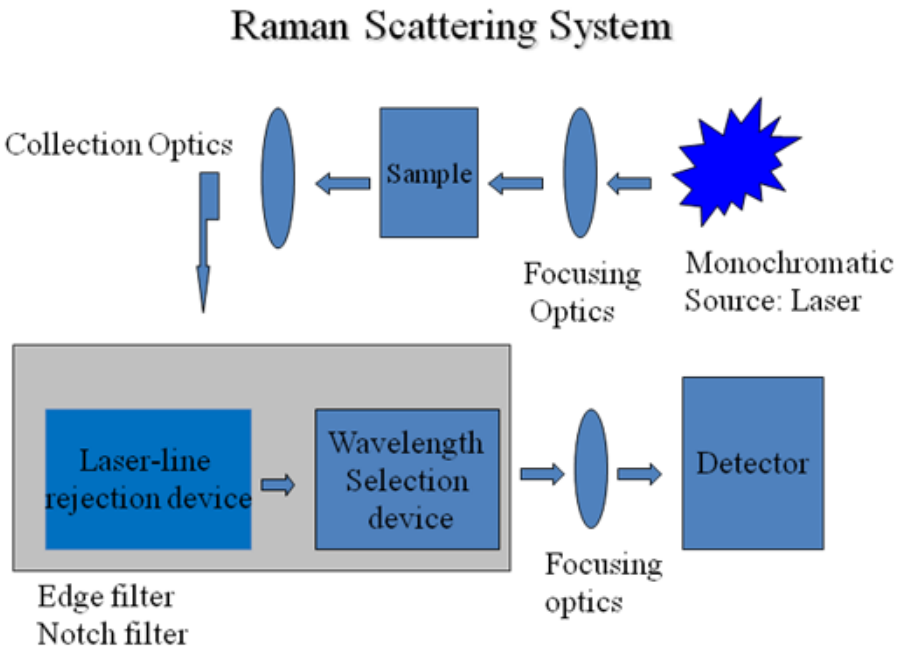

FIG. 2.3 A schematic diagram of Raman scattering spectroscopy.

2.3 Electron microscope related techniques

All the TEM-related measurements were performed in a JEOL 2010F field emission TEM, which has two imaging modes: TEM and STEM. It is operated at the accelerating voltage of 200 kV. The spherical aberration of the machine is 0.5 mm, the resolution is 0.19 nm and the focused probe is 0.2 nm. The microscope can be operated in annular dark-field STEM mode and has an instrumental resolution of 0.14 nm. The NWs were detached from the substrate and placed on a carbon-coated 3 mm copper grid.

2.31 High resolution TEM

It is necessary to figure out what information is of interest before doing HRTEM imaging. For example, the lattice fringes in a high resolution image carry information about the crystal structure on a fine scale. To obtain a phase-contrast HRTEM, the following steps are needed.

(1) Select TEM with low spherical aberration Cs and small wavelength λ;

(2) Perform good alignment and make sure the beam is on the zone axis;

(3) Use an under-saturated LaB_6 filament and small condenser aperture;

(4) Work at high magnification and frequently perform current and voltage centering of objective lens;

(5) Correct condenser and objective lens astigmatism;

(6) Find minimum contrast focus setting for objective lens;

(7) Record DP at the same setting of the condenser lens.

Specimen thickness and orientation are very critical for HRTEM imaging, so thin, flat and clean sample is needed. In addition, contamination and damage caused by the electron beam should be taken good care of.

2.32 Calibration of the imaging system

To carry out accurate measurements of images and diffraction pattern, it is important to calibrate TEM machine before every measurement. A set of standard calibration conditions (e.g. objective lens current, eccentric height and other lens setting) must be specified.

(1) Magnification calibration

Magnification calibration is very important, because the lens strength in the TEM imaging system is not stable and it changes with ambient temperature, lens hysteresis and efficiency of cooling system of lenses. A standard specimen is required for the calibration. The TEM is set to its standard conditions with the specimen at the eccentric height and the image focused. Then the images of the standard specimen at some magnification settings are recorded, so the magnification can be calculated experimentally from these images. In addition, the magnification calibration is so sensitive to many variables that some users put the standard materials together with the specimen into the TEM for exactly the same conditions.

(2) Camera-length calibration

The magnification of the DP by camera length also needs calibration. The camera length in the TEM is a calculated value instead of a physical distance. Assuming R is the separation of the direct and diffracted beams as measured on

the screen, d is crystal spacing, L is camera length and λ is the wavelength of the beam electrons, they satisfy the equation $Rd=\lambda L$. The DP of a standard specimen with known d is recorded. If the pattern is a ring, then measure the ring radius R for any diffraction plane. If it is diffraction dots, R is the distances between dots for any diffraction planes and central dot. Then L will be determined if λ is known.

2.33 Detectors

To satisfy all kinds of characterization demands, the JEOL 2010F is equipped with CCD camera, Gatan Enfina energy-loss spectrometer, thin-window light-element-sensitive X-ray detector, double-tilt holder, and Gatan EDAX acquisition system for high-spatial-resolution microanalysis, as shown in Fig. 2.4. The detectors which are included in JEOL 2010F are the following:

(1) Axial bright field detector

The acceptance angle is around 1-5 mrad, which is defined by the collector aperture size and the post-specimen lens effects.

(2) Annular dark field detector

It has a mask to block the direct signal and collect the scattered signal among 15-150 mrad.

(3) High angle ADF detector

It receives most diffracted beams through 50-150 mrad.

(4) Secondary electron detector

(5) Annular backscattered detector

It collects signal with scattering angle around 400-1200 mrad on the entrance side.

(6) Diffraction detector

It shows the angular distribution of transmitted electrons at 0-120 mrad.

(7) EDX detector

(8) EELS detector

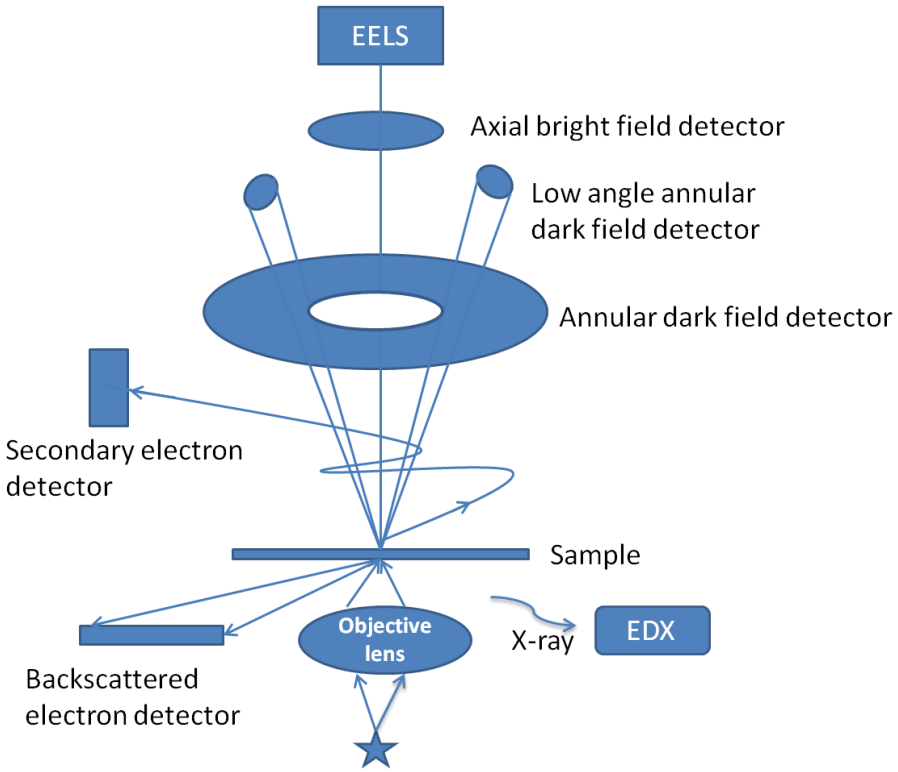

FIG. 2.4 Different detectors equipped in TEM chamber that meet different imaging and microanalysis requirements.

CHAPTER 3

CHARACTERIZATION OF InAs NWS OF DIFFERENT STRUCTURES

3.1 Introduction to bulk InAs and NWs

InAs has many attractive electronic and optical properties that can be utilized for optoelectronic applications. As a direct, narrow-band-gap semiconductor with very high electron mobility, InAs has long being considered an ideal material for middle wave IR detectors and lasers. In the NW form, its size quantization and optical waveguide make InAs NWs promising materials for nanoscale optoelectronic applications. With a large Bohr radius of 34 nm,[49] InAs NW is a good candidate material to study one dimensional quantum confinement effects.[50] Furthermore, the larger tolerance for lattice mismatch in NW growth than that for thin film epitaxial growth results in more flexibility in substrate selection for InAs NWs; NWs also have the additional flexibility of a wide range of diameter control by varying the growth conditions. Regarding growth studies, both MBE[51, 53] and MOCVD[52, 54, 59] grown InAs NWs have been reported. Wurtzite (WZ) as well as zinc blende (ZB) crystal phase has been observed in InAs NWs[51, 53, 56-58] The surprising formation of the WZ phase in InAs and other NWs of cubic ZB III-V materials is usually explained by a lower surface energy of particular sidewall facets of WZ NWs[55, 59, 60] and the specific growth properties of sufficiently thin NWs such as the nucleation at the triple line.[61, 62] Different band gaps for the two phases were predicted by Zanolli et al..[63] Regarding device studies, electrical measurements of InAs NWs have been reported recently.[64, 65, 66] However, there

has not been any optical characterization study, such as PL study, reported to my knowledge. This lack of a PL study of InAs NWs is likely due to a combination of factors that increase the difficulty of performing the optical characterization of InAs NWs: weak light emission in narrow-band-gap materials, limited detector availability for mid-infrared wavelengths, atmospheric absorption in the infrared region, and difficulties associated with the growth of InAs NWs of high enough quality to emit observable PL signal. It is important to characterize such basic optical properties of InAs NWs in order to assess their use in optoelectronic devices. So we have carried out a systematical optical characterization of InAs NWs as part of my effort in developing IR NW optoelectronics.

3.2 Growth and characterization methods of InAs

The InAs NWs were grown by G.E. Cirlin et al. in Ioffe Physical Technical Institute in Russia. Three samples A, B and C were grown by the Au-assisted MBE technique on the GaAs (111) B and Si (111) substrates. GaAs substrates were epi-ready (surface deoxidation was performed at 610 ^{o}C in a high-vacuum growth chamber) and Si substrates were treated in a HF (10 %) water solution for about 1 min (with surface deoxidation performed at 650 ^{o}C). Their MBE growth chamber is equipped with In, As, and Au effusion cells, which allows them to deposit the gold catalyst layer under high-vacuum conditions, in order to avoid surface contamination issues. After surface deoxidation, they deposited Au with nominal thickness ~ 0.5 nm at the temperature of 500 ^{o}C. Subsequently, the samples were cooled down to the desired temperature to initiate InAs NW growth:

480 ^{o}C for GaAs substrates and 300 ^{o}C for Si substrates. InAs deposition was initiated with the nominal growth rate of 0.4 nm/s and As/In fluxes ratio around 2. In both cases, the nominal growth time was limited to 15 min (~ 0.36 μm of InAs was deposited). The growth of the InAs NWs was monitored in situ with a reflection high-energy electron diffraction (RHEED) system. Usually, RHEED patterns converted from streaky to spotty (i.e., amorphous to crystalline) after the growth of about 20 nm of InAs. After completion of growth, the samples were immediately quenched down to room temperature.

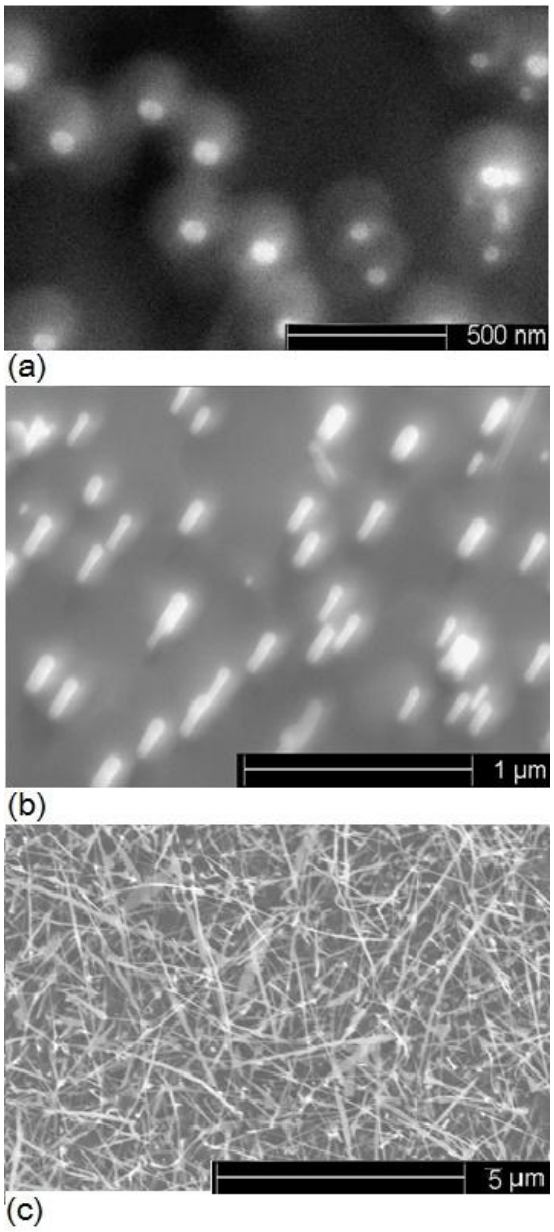

FIG. 3.1 (a) Top-view and (b) 10 degree-tilted view SEM images of sample A. (c) Top-view SEM image of sample C.

Samples A and B were grown on GaAs substrates, with dimensions of 20-40 nm in diameter and 300-500 nm in length for sample A and 40-70 nm in diameter and 700-1000 nm in length for sample B. Fig. 3.1 shows top-view (a) and 10 degree-tilted view (b) of SEM images of sample A, where the NWs are grown vertically on a GaAs substrate. The SEM images of sample B showed similar vertical growth. Sample C is grown on a Si substrate, with NWs lying on the substrate with random orientations, as shown in Fig. 3.1 (c). The lengths of NWs of sample C are about 5 μm and the diameters are over 80 nm. HRTEM and SAED patterns were used to determine the crystal structure of the NWs.

The MIR micro-PL setup in our lab was used to study the PL properties of the InAs NW samples. The samples were illuminated by the Ti:Sapphire laser. Samples are placed in a microscope cryostat (under vacuum) with liquid helium cooling for PL measurements at 4 K. An optical attenuator was used to modulate the incident laser power for excitation-intensity-dependent PL measurements. The excitation laser was directed to the samples at 45 degrees from the substrate surface normal (off-axis incidence, or dark-field illumination). The PL light emission was collected along the substrate normal direction by an all-reflective objective lens. The excitation laser beam was focused by a long focal-length lens before reaching the samples. PL from the samples was detected using a liquid nitrogen cooled InSb photodiode detector. An optical chopper in the excitation laser beam and a lock-in amplifier connected to the InSb photodiode were used to suppress detector noise. The detector was coupled to a monochromator with a 300 grooves/mm grating to yield a 0.2 nm spectral resolution. Compressed nitrogen

gas was used to purge the PL light path to reduce water and air absorption. In this chapter, low-temperature, temperature-dependent, and excitation-intensity-dependent PL measurements were performed on four InAs NW samples (grown on either GaAs or Si substrate) in order to elucidate the nature of various PL features.

Raman scattering spectra of sample A and B were recorded by the high spatial resolution Micro-Raman setup in our lab at room temperature (shown in Fig. 3.2). The 532 nm green CW laser was used as excitation source. The operational laser beam was focused in submicron scale. A 50× objective lens is utilized in the imaging and collection system. Strong first-order transverse optic mode[67] was observed at the position of 217 cm^{-1}. It is found that sample A have much stronger Raman scattering than sample B, indicating better crystal quality of sample A.

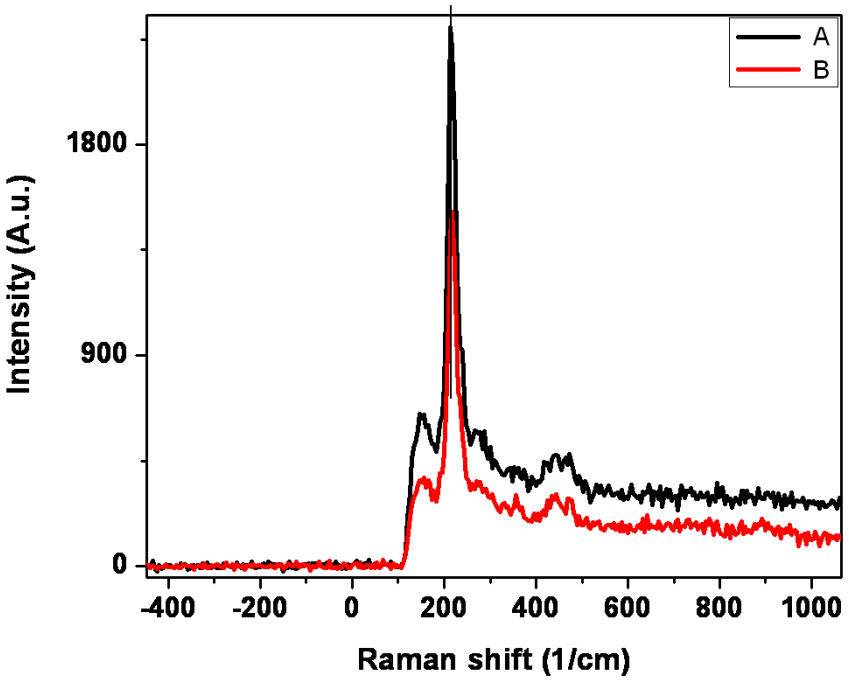

FIG. 3.2 Micro-Raman scattering spectra of samples A and B measured at room temperature.

A few words are in order about the PL measurement from as-grown samples. First, since the samples were grown on GaAs or Si substrate, PL contribution from the substrate is in a different wavelength range. Second, there is sometimes a thin layer of to-be-grown semiconductor being deposited on the substrate before wires are grown and they would contribute to the PL signals. Indeed in our MBE samples, a thin 2D InAs layer is formed; but this 2D layer was amorphous as indicated by the RHEED pattern. High lattice mismatch for both hetero-pairs: InAs/GaAs - 7%, InAs/Si - 11.6% leads to a 2D layer with a high density of dislocations. The relatively low growth temperature (300 ℃, in the case of Si substrate) is definitely too low to grow thin film with good crystalline quality. To

make sure that the 2D layers do not contribute to the detected PL signal, the PL for samples grown with the same procedure but without gold deposition was checked. In this case the 2D layer appeared after the very first stage of quantum dots formation. Those samples did not show any noticeable PL signal. Thus the PL measurement from the as-grown sample is from the NWs, with negligible contribution from the underlying thin layer.

3.3 PL features and their correlation with microstructures

The SAED pattern (upper left corner in the left image of Fig. 3.3) was obtained from sample A and can be indexed as the <01-10> zone axes of WZ structure. The higher magnification inset in the HRTEM image in the left image of Fig. 3.3 clearly shows the growth axis along <0001> direction. All of these indicate that sample A is single crystal with WZ structure. Sample B has the same crystal structure as sample A. The HRTEM image together with fast Fourier transforms (FFT) pattern in the right image of Fig. 3.3 shows that sample C is also single crystal, but with ZB structure, which is the crystal structure of bulk InAs. The growth direction of these NWs is <01-1>.

As pointed out earlier, the diameter of InAs NWs grown on GaAs substrates is smaller than the diameter of those grown on Si substrate. This difference in diameters is attributed to different growth mechanisms caused by different substrates. For the epitaxial Au-assisted growth on the lattice mismatched substrates,[60, 68] the NW formation requires a replication of certain crystal planes of the substrate to ensure the elastic stress relaxation on the sidewalls. During the

very early stage of the Au-assisted epitaxial growth, the diameter of the NW must be limited to a small value in order to maintain the coherence of the NWs with the substrate, due to lattice mismatch between InAs and GaAs. The growth mechanism is responsible for the tolerance of epitaxial NW growth to very large lattice mismatch, which is impossible in thin-film growth (and even in quantum dots). This lattice mismatch tolerance provides much more flexibility in integrating different material for various device applications than the epitaxial thin-film approach. Larger lattice mismatch will result in smaller diameter of epitaxial NWs to maintain the coherence the lattice planes with the substrate during the early stage of epitaxial growth.[68] It should be noted that the epitaxial growth strongly depends on the growth conditions. For example, InAs NWs epitaxially grown on Si (111) substrate was also reported.[57, 68] On the other hand, in non-epitaxial growth, such as the growth under our growth conditions on Si substrates, there is no such limitation and the diameter mainly depends on the initial Au-catalyst size. The strain could be relaxed at the sidewalls of vertically freestanding NWs very quickly after very short time growth. Once the growth direction is established, NWs will continue to grow in the same growth direction for the entire growth period.

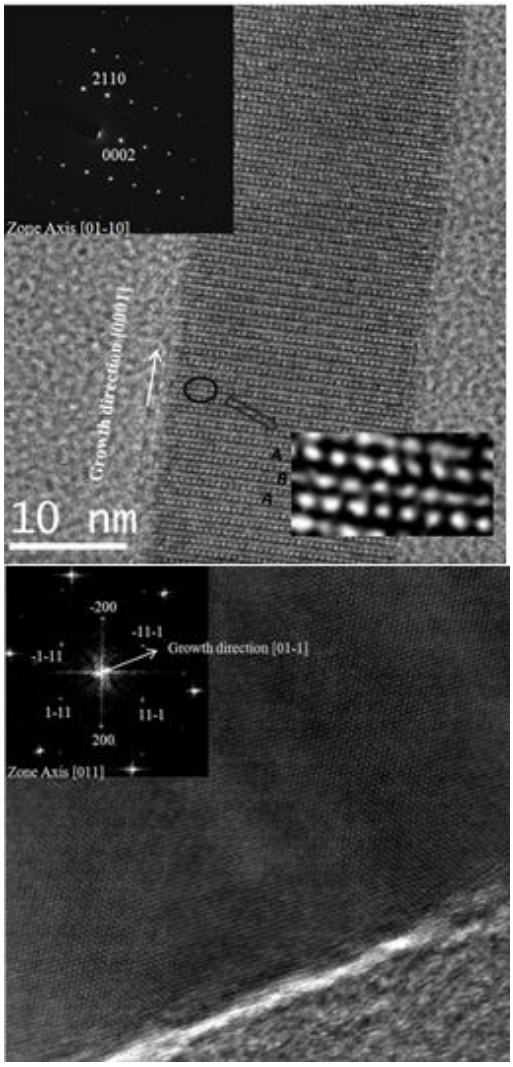

FIG. 3.3 Upper: HRTEM image of sample A with SAED pattern as inset (upper left corner). Down: HRTEM image of sample C with FFT pattern as inset in the upper left corner. The gray amorphous parts in the two images are from carbon films.

The PL measurements of samples A, B and C were performed at temperature as low as 4 K, with the excitation laser at a wavelength around 790 nm, and with average excitation powers up to 700 mw. The NW PL data in Fig. 3.4 is taken at 4 K with 700 mW average excitation power, with PL measurement on an InAs wafer at the same excitation level shown for comparison. The InAs wafer (purchased from MTI Corporation) is unintentionally doped n-type with carrier concentration of 1.8×10^{16} /cm^3 and its growth direction is (100). InAs wafer has a PL peak at around 2970 nm (0.417 eV), as shown in Fig. 3.3 a. This peak is consistent with the known temperature dependence of the InAs band gap: E_g (T) =415-[0.276T^2/ (T+83)] (in meV, *T* in K)[69] and corresponds to the band-edge emission of InAs. The PL spectra of the NW samples in Fig. 3.4a have complex shapes and features and are much wider than the PL spectrum of bulk InAs. In addition, samples A and B show significantly blue-shifted PL peaks compared to the bulk InAs PL peak. In general, several factors could lead to the blue-shifted peaks or more complex PL spectral shapes for NWs than for bulk: quantum confinement, surface or defect state effects, and different crystal structures. As the sizes of the NWs in sample A are comparable to the InAs Bohr radius (~34 nm), quantum confinement effects could play a role. Furthermore, since the diameters of the NWs are very small, surface effects become important because most of the photo-generated carriers in a NW are close to the NW surface. In addition, different crystal structures of NWs in samples A and B from the bulk InAs could also be responsible for the difference in the NW PL features relative to the bulk PL.

To extract more information from the PL spectra, each of the measured spectra was fitted by multiple Gaussians. The spectral fits are shown in Fig. 3.3 (b), (c), and (d). The two samples grown on GaAs substrates can be fitted by three Gaussians, centered at 2785 nm (0.445 eV, peak A1), 2910 nm (0.426 eV, peak A2) and 3160 nm (0.392 eV, peak A3), respectively for sample A and centered at 2825 nm (0.439 eV, peak B1), 2925 nm (0.424 eV, peak B2) and 3160 nm (0.392 eV, peak B3) for sample B. From the peak positions, it seems that the corresponding ones in sample A and B have similar origins. The higher energy peaks A1 and B1 have full-width-at-half-maxima (FWHM) around 23 meV and 17 meV respectively, which are much narrower than A2 and B2. All four peaks (A1, A2, B1, and B2) have peak wavelengths shorter than the band-edge peak from the InAs wafer. The small and broad low-energy peaks A3 and B3, which have the same peak positions, are consistent with the DAP recombination emission observed by Lacroix et al.[70] and the peaks I observed are weaker and broader.

The PL spectrum of sample C can be de-convoluted into four Gaussians, centered at 2865 nm (0.433 eV, C1), 3050 nm (0.406 eV, C2), 3270 nm (0.379 eV, C3) and 3580 nm (0.346 eV, C4), respectively, as shown in Fig. 3.3 (d). The NWs in sample C have the same crystal structure as the bulk material and much larger diameters than the Bohr diameter, so no quantization effects were expected here. The InAs NW PL spectra on sample C were compared with bulk InAs PL to identify the origins of the four peaks. The highest energy peak C1 has higher energy than the band-edge peak of the bulk material at the cryogenic temperature

of 4 K. Further analysis on this peak will be provided later. Peak C2 seems to be consistent with the reported neutral-donor-bound exciton and free-exciton emission peaks. It has been observed previously[70] and attributed to a shallow defect. Theys et al.[73] found that hydrogen passivation could remove this peak, and conjectured that it came from a structural defect-related acceptor state. Peak C3 has been found in some reports,[71, 74] where it was attributed to a deep impurity, or defect-related acceptor level, around 35 meV above the top of the valence band. Peak C4, which is from far below-bandgap recombination, has not been observed in the bulk or film material before to our knowledge. However, we also observed this peak when measuring the InAs NWs grown on Si substrate using the method of MOCVD,[68] as shown in Fig. 3.4. The samples were provided by L. Chuang and C. Chang-Hasnain in University of California, Berkeley. This peak does not shift with temperature. The small diameter (10-20 nm) of these NWs indicates that the recombination is dominated by surface events. It would be interesting to study the PL after surface passivation, which is currently underway.

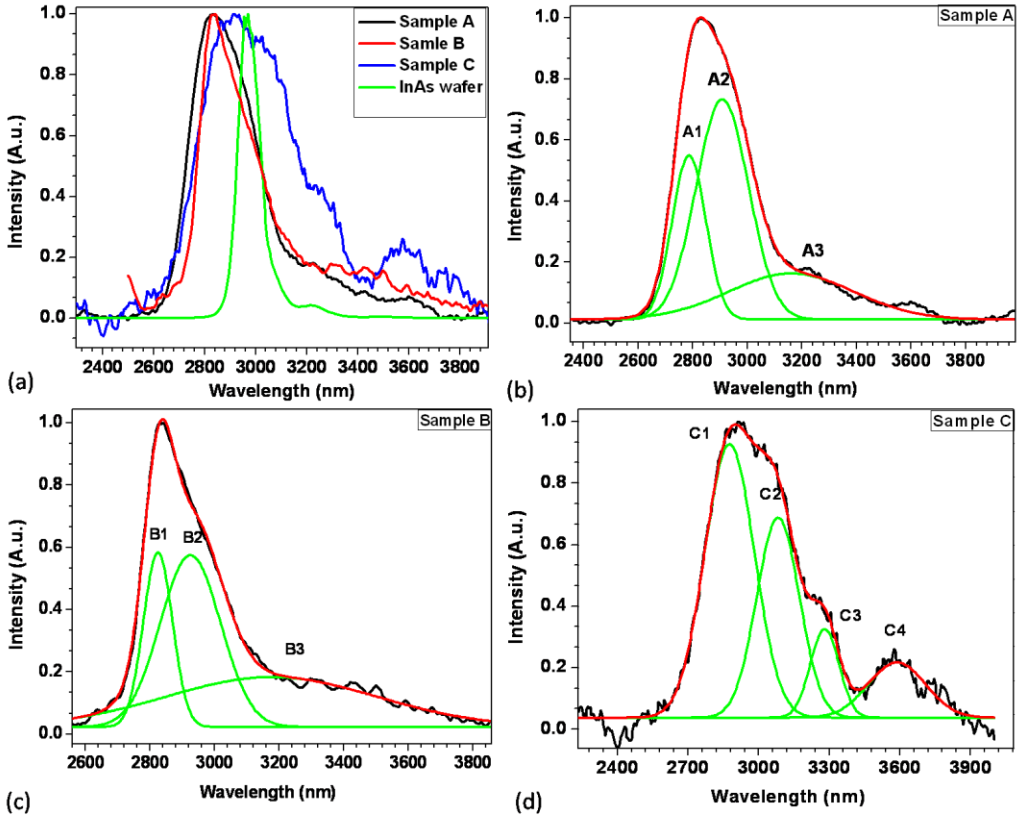

FIG. 3.4 Normalized PL Spectra measured at 4 K for samples A, B and C and an InAs wafer (a); for sample A fitted with Gaussians A1, A2 and A3 (b); for sample B fitted with Gaussians B1, B2 and B3 (c); for sample C with fitted Gaussians C1, C2, C3 and C4 (d).

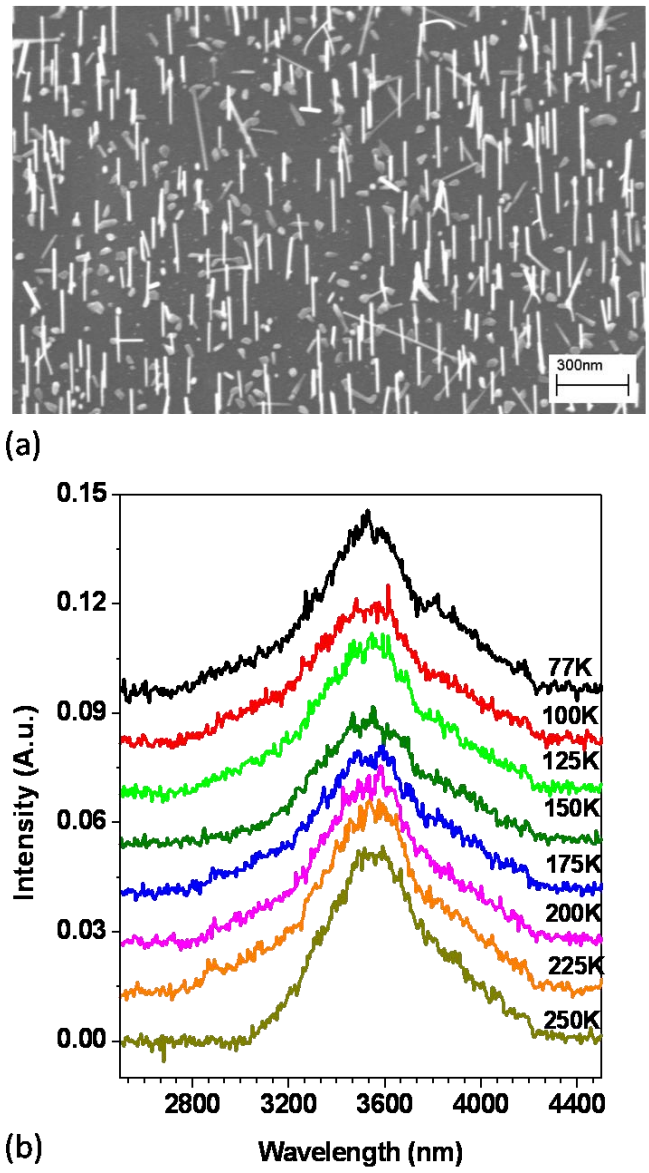

FIG. 3.5 (a) 20 degree tilt SEM image of InAs NWs grown on (111) Si substrate using the method of MOCVD. The NW diameters are around 10-20 nm and the NW lengths are around 500 nm. (b) Temperature-dependent PL measurements of the as-grown InAs NWs.

Temperature and excitation-intensity-dependent PL measurements for both sample A and B were performed to shed more light on the origins of the PL peaks. Sample B showed similar results to sample A, so only the results of sample A was discussed here. Fig. 3.6 (a) shows the temperature-dependent PL measurements of sample A and the corresponding multi-Gaussian fittings. Fig. 3.6 (b) shows how the two fitting Gaussians change with temperature. Peak A1 with higher energy shows no significant shift, suggesting that it most likely originates from some defect states rather than from band-edge emission. Peak A2 shows an obvious red-shift as the temperature increases and likely the band-edge related emission. If this is the case, peak A1 should come from the above-band-edge emission, which may be related to some surface state emission. We also performed temperature dependent PL measurements on InAs wafer at the same pumping level as for NW measurements. The results are shown in Fig. 3.6 (c) together with corresponding multi-Gaussian fittings. Fig. 3.6 (d) shows the two fitting Gaussians at various temperatures. Peak D2 has obvious red shift with increasing temperature. It is related to the band-edge emission of InAs. Peak D1 does not shift with temperature and has higher energy than the band-edge emission peak. This peak resembles peak A1 for the NWs. It is well-known that electron accumulation can be easily formed on even very clean InAs surfaces.[75-77] These surface states pin the Fermi energy level above the conduction band minimum (CBM). Angle-resolved photoelectron spectroscopy (ARPES) measurements[76] showed the existence of charge accumulation on InAs surface and the surface states excitation in InAs above the CBM. In their work, various surfaces were examined. Their

results showed that the energy spectrum of intrinsic surface states of InAs is determined by surface reconstruction and the surface states stemmed from native point defects. These conclusions are consistent with the high-resolution electron-energy-loss spectroscopy (HREELS) measurement results.[77] According to HREELS measurements, the valence band maximum is 0.58-0.65 eV below E_F for As-stabilized surface. The above-band-edge surface states have also been identified in other material such as GaN NWs.[78] The observed peaks A1, B1, and C1 in NWs are very likely originated from above-band-edge surface states, as D1. But since the surface states of wires exist mostly on the side walls of wires and there are several surfaces involved in general, further experiments are needed to make a definitive conclusion about the origin of A1 and B1.

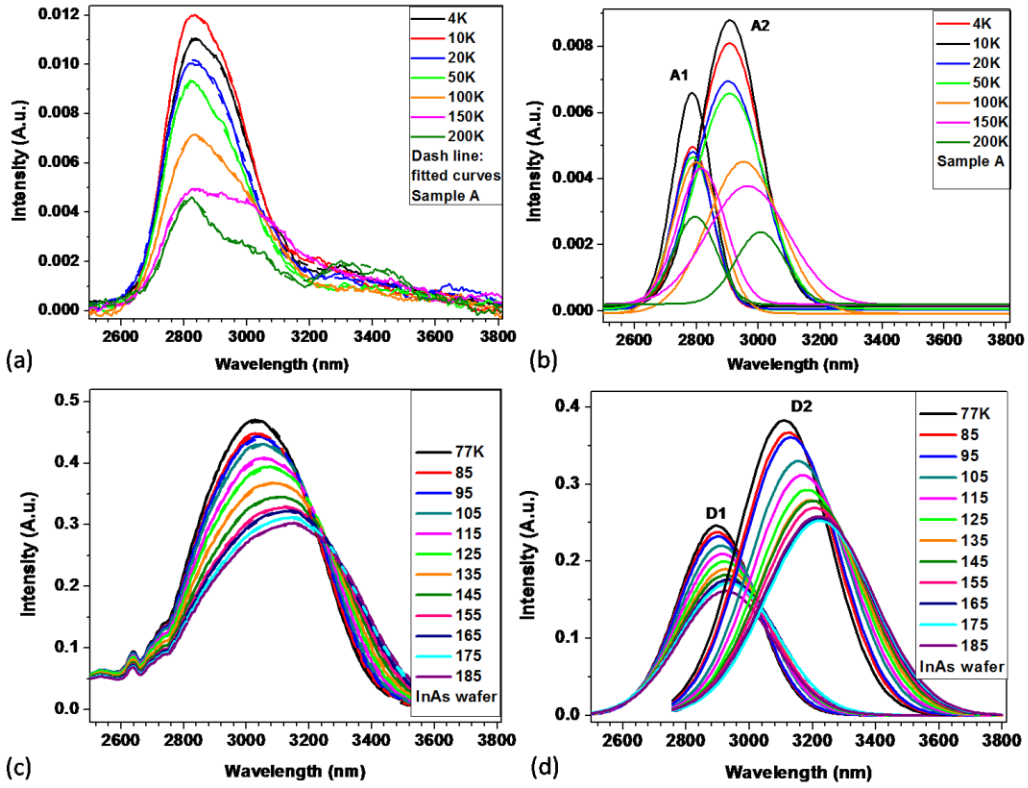

FIG. 3.6 (a) Temperature dependent PL spectra of sample A. The dashed lines are fitted curves. (b) The corresponding individual Gaussians (peak A1 and A2) whose superposition fit the PL spectra of figure (a). (c) Temperature dependent PL spectra of InAs wafer. The dashed lines are fitted curves. (d) The corresponding individual Gaussians (peak D1 and D2) whose superposition fit the PL spectra of figure (c).

Fig. 3.7 (a) shows temperature-dependence of the peak-wavelengths of the Gaussians from both NWs and wafer. The black curve is the temperature dependent band gap of bulk InAs according to the Varshni formula.[69] Obviously, both peaks A1 and A2 are blue-shifted from the band-edge of bulk InAs. As we mentioned earlier, peak A1 is likely due to surface-related above-band-edge emission and shows no significant shift with temperature. Both samples A and B have WZ crystal structure while bulk InAs has ZB crystal structure. Zanolli et al[63] theoretically predicted an increase of band gap for the WZ phase with respect to the ZB phase using the dynamically screened exchange or GW approximation (based on a model dielectric function theory). However, the predicted blue-shift for WZ InAs is around 50 meV from ZB, which is much larger than the blue-shifts (of 9 meV) we measured here. Another possibility is size-dependent quantization effects, since the diameters of the NWs from sample A are on the order of the Bohr radius of InAs. A calculation to determine the band-edge shift due to size quantization has been performed. The NW has been modeled as cylindrical structure with infinite barriers using effective-mass approximation. The energy gap between the quantized ground states of conduction band and valence band is given by

$$E = E_g + \frac{\eta^2 \chi_{ns}^2}{2D^2}\left(\frac{1}{me} + \frac{1}{mh}\right),$$

where E_g is the bulk band gap; χ_{ns} is the s-th root of the Bessel function, $J_0(x)$ and the first root (2.4048) was chosen in our calculation; me ($=0.0265m_0$) and m_h ($=0.41m_0$) are the effective masses of electrons and holes[78] of InAs; D is the

diameter of NWs. The calculation result based on this model was shown in Fig. 3. 7 (b) at temperature of 4 K. Peak A2 is 2910 nm and it corresponds (from the calculated curve) to a diameter of 33 nm (red dot), which is in the range of diameters measured of sample A. Peak B2 is 2925 nm and it corresponds to 39 nm (green dot). Even though this diameter is near the lower limit of the range of diameters I measured for sample B, I notice that larger diameters closer to the measured value would not change the peak wavelength significantly, since the wavelength changes very little at the large diameter values as can be seen in Fig. 3.7 (b). Therefore, my calculation shows that peak A2 and B2 are very likely due to quantization effects. I also marked in the same figure the wavelengths of peak A1 and B1. Obviously these peaks are far removed from the quantization values. The large difference from the calculated band gaps and the insensitive temperature dependence shown in Fig. 3.7 (a) is another evidence that peak A1 and B1 are from the surface related states. Similarly, C1 also likely comes from the above-band-edge surface states emission. For ease of reference, Table 3.1 summarizes the peak positions, FWHM, and a brief description of assignments of various PL peaks observed in InAs NWs in my work.

PL peak is very often used as a measure of band gap for direct gap semiconductors. But I see from Fig. 3.7 (a), peak A2 shows much less red-shift than the bulk bandgap as temperature is raised. In fact, PL peak does not correspond to the band gap in general, especially for narrow gap materials. Assuming parabolic band, momentum conservation, and the Boltzmann distribution of carriers, one can show that the band gap energy is red shifted by

$k_BT/2$ from the PL peak energy, where k_B is the Boltzmann constant and T the temperature. While this value is much smaller typically, it becomes a significant contribution for narrow gap semiconductors, especially when temperature dependence is concerned. To account for such difference, we corrected PL peaks A2 and D2 by $k_BT/2$ as shown in Fig. 3.7 (a). After this correction, we can see that the tendency is more similar with the band gap change (black curve). Thus, a shift of $k_BT/2$ is significant for InAs especially at high temperature. To obtain a more precise correction, a better model can be used. For example, we can change the carrier distribution from Boltzmann to Fermi-Dirac statistics, where the chemical potential is needed. The latter is related to the temperature and carrier density, which is not directly measured in my case. Further measurements are therefore necessary to find out the exact band-edge positions of the InAs NWs. There may be also a possibility that the excitation laser may locally raise the temperature of the NWs, so the NW temperature may be higher than that of the substrate.

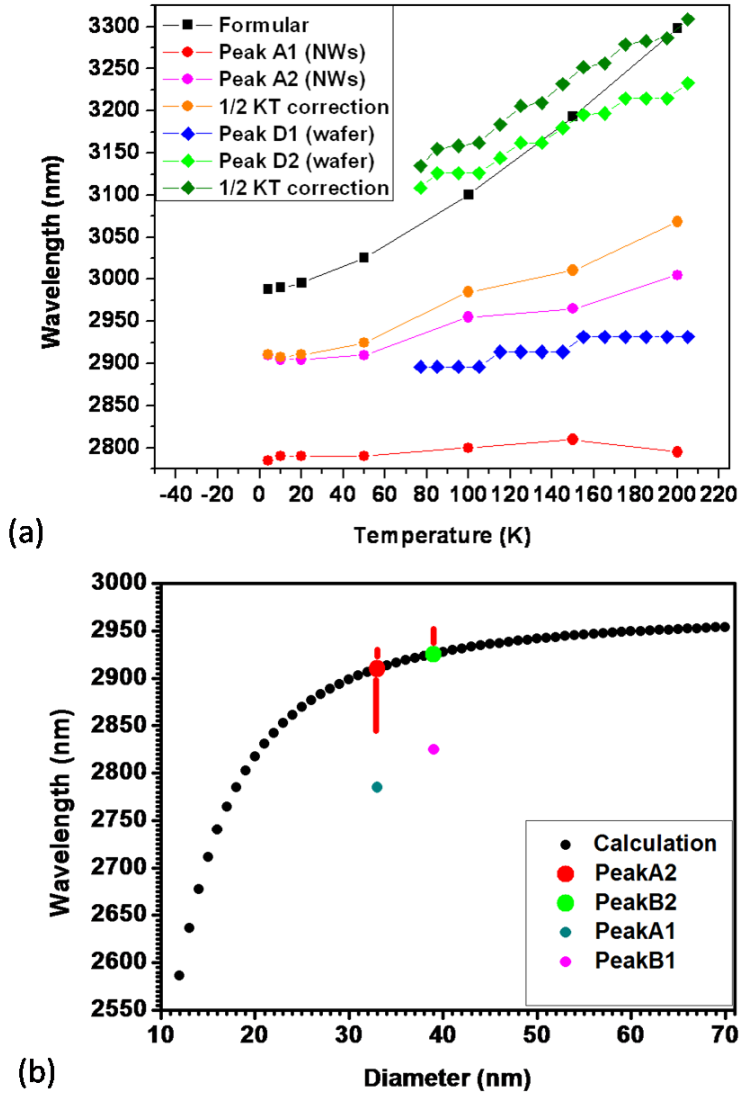

FIG. 3.7 (a) Temperature dependence of the wavelength of peak A1, A2, D1 and D2. The black line is obtained from the Varshni formula for the bandgap of bulk InAs. The green and orange lines are obtained by a correction of $k_BT/2$ from the PL peaks. (b) Quantized bandgap (in terms of wavelength) as calculated as a function of diameter of NWs (black dots). The peaks A1, A2, B1, B2 are dotted with different colors. The vertical (red) bars indicate the range of wavelength values corresponding to the range of diameters as measured.

Table 3.1 InAs NWs PL peak positions at 4 K with assignments and references

Peak Symbol	Peak λ (nm)	Peak (eV)	FWHM (meV)	Assignments and comments
A1	2785	0.445	23	Above-band-edge surface-states-related recombination. These peaks have little shift with change of temperature. See Fig. 3.4, 3.6.
B1	2825	0.439	17	
C1	2865	0.433	29	
A2	2910	0.426	34	Band-edge emission, blue-shifted due to size quantization, which shows obvious red shift with increasing temperature. See Fig. 3.6.
B2	2925	0.424	33	
A3	3160	0.392	80	Donor-acceptor-pair recombination. See Ref.70.
B3	3160	0.392	93	
C2	3050	0.406	35	Neutral-donor-bound exciton and free-exciton recombination. See Ref. 70, 72, 73
C3	3270	0.379	12	Recombination of deep impurity or defect-related acceptor. See Ref. 71, 74.
C4	3580	0.346	20	Not reported before, but observed in InAs NWs grown on Si substrates using both MBE and MOCVD.

To gain insights into other effects of surface-states and crystal quality of the NWs, we also performed excitation-intensity-dependent PL measurements on sample A and C at the temperature of 4 K. Fig. 3.8 presents the excitation intensity dependent PL spectrum of sample A (a), the corresponding Gaussians for the best fit (b), and the excitation intensity dependent PL spectrum of sample C (c). There is no obvious peak shift with laser power for the both peaks A1 and A2. Fig. 3.8 (b) shows how the intensities of peak A1 and A2 change with the excitation power. We can clearly see that peak A2 is stronger and saturates at a much higher level than peak A1. The saturation of surface state emission being slower than band-edge may indicate that most of the non-radiative recombination centers lie in the NW body and not on NW surface and that the number of surface states is large. Surface states are very important for NWs, due to the large surface to volume ratio and due to the fact that they can act as radiation recombination centers. The saturation excitation power for sample C (366 mW) is much smaller than that of sample A (700 mW). This together with the smaller peak intensity, noisier PL spectrum, and weaker band-edge emission from sample C than from sample A all show that sample C grown on Si substrate has a poorer crystal quality than sample A and B grown on GaAs substrate. Chuang et al.[68] reported that the critical diameter of epitaxial InAs NWs on Si substrate (lattice misfit = 11.6 %) was about 26 nm in the case of Au-assisted MOCVD. In the case of Au-assisted MBE, the reported value of critical diameter equals 24 nm.[80] The sizes of the NWs in sample C are far above this, consistent with the fact that the InAs NWs were not grown epitaxially on the Si substrate in our case. For sample A and

B, the NWs have smaller lattice mismatch (7.1%) with GaAs substrates and much smaller size (many NWs are smaller than critical diameter for coherent growth of approximately 45 nm.[80] The vertical growth and the high material quality indicate that most of these NWs are grown epitaxially on GaAs substrates, consistent with the strong PL emission in our experiments (particularly in Sample A). No band-edge emission was observed from InAs NWs grown using the method of MOCVD, which means their lower crystal quality than NWs grown using MBE.

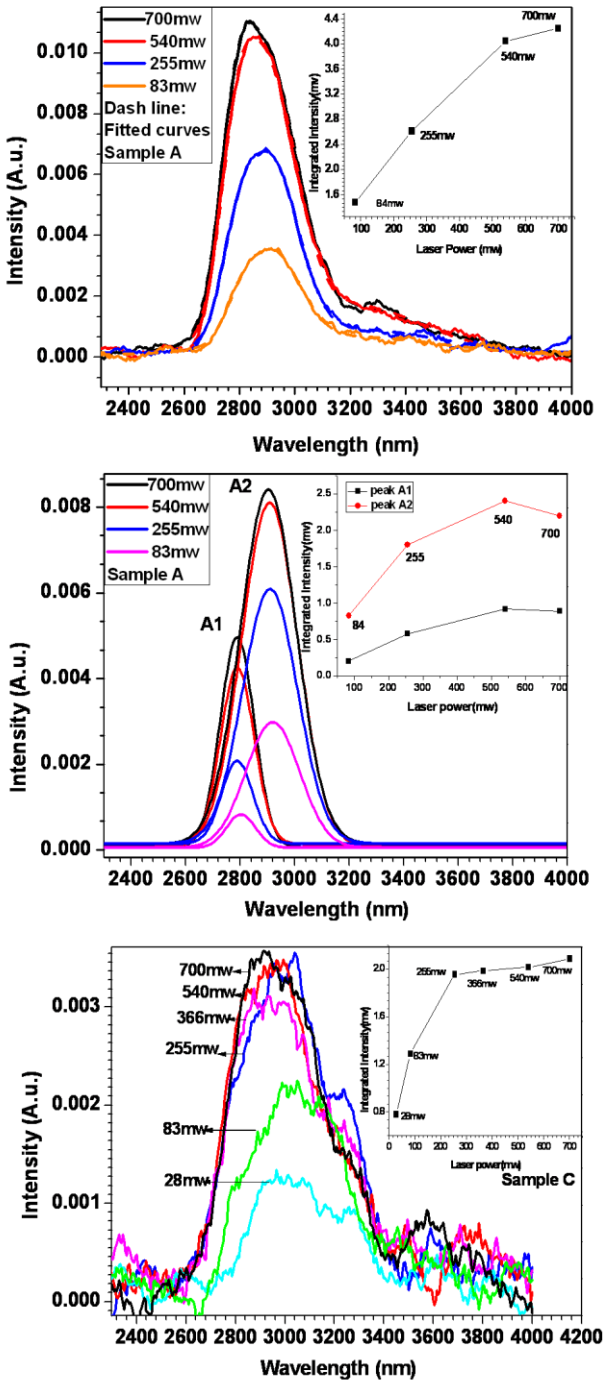

FIG. 3.8 The excitation intensity dependent PL measurements of sample A (a), the corresponding Gaussian fittings at different pumping levels (b), and PL spectra at several excitation levels for sample C (c). The insets in the three figures show the integrated intensity versus laser power.

3.4 Summary

The origins of low-temperature PL emission peaks from MBE- and MOCVD-grown samples of InAs NWs were investigated using micro-PL and correlated to structural characterization using SEM, HRTEM, and SAED. The HRTEM and SAED pattern shows InAs NWs grown on GaAs substrates have a WZ crystalline structure while InAs NWs grown on Si substrates have a ZB structure. The PL measurements shows MBE grown InAs NWs on a GaAs substrates have higher crystal quality than those grown on Si substrates and both of them have higher quality than MOCVD InAs NWs. Based on the systematic excitation-intensity and temperature dependent PL measurements and analysis, We can classify three types of PL peaks: The first is the above-band-edge peaks such as A1, B1, and C1. These are most likely related to the surface states and they exist also in the bulk InAs (D1). The second peak is the band-edge related peaks such as A2, B2. Peaks A2 and B2 are blue shifted by 60 nm and 45 nm from that of bulk InAs at 4 K, respectively, and are most likely due to quantization effects. The consistency of our calculation and experimental measurements supports such an assignment. The blue shift is much smaller than what is expected from the wider gap calculated for WZ structure and thus is less likely due to the difference of WZ crystal structure. The band gap of the bulk InAs in the WZ phase remains an unresolved issue at this point. The third group of peaks is related to below-band-edge states, which are attributed to various donor or acceptor bound states. Even though more studies on better samples are still needed, we believe that our systematic investigation

sheds light on the light emission properties and the crystal quality of InAs NWs. All these results have been published in *Nanotechnology*.[81]

CHAPTER 4

SURFACE PASSIVATION AND OPTICAL CHARACTERIZATION OF InAs NWs

4.1 Introduction to surface states and surface passivation

Surfaces and interfaces strongly affect the optical and electrical properties of semiconductor and device performance. InAs is a very interesting direct narrow-band-gap material and has important applications in high-speed circuits and optoelectronic devices such as lasers, detectors and sensors in the MIR wavelengths. However, the existence of large densities of surface states on InAs has a strong negative effect on its device applications because of Fermi-level-pinning and the degradation of electrical and optical properties. This becomes more and more important for small-size optoelectronic devices because of their large surface-volume ratio. Surface-states radiative recombination plays an important part in the optical properties of InAs NWs.[81] These surface states can lie above or below bandgap and they can compete with band-edge emission, which greatly reduce the luminescence efficiency. Therefore, effective passivation is very important to eliminate the undesirable surface states, decrease surface recombination velocity and prevent the new formation of surface states. In addition, passivation can help to build a chemically inactive surface. Surface passivation has been utilized on many semiconductor MWs to improve their optical or electrical performances such as ZnO,[82, 83, 84] Si,[85] Ge,[86] and InP.[87, 88] There are two main passivation directions: one is to deposit insulator layers to

form a semiconductor-insulator heterojunction; the other is to modify the surface atomic structure by foreign atoms. Functionalization of semiconductor surfaces with organic self-assembled monolayer (SAM) can take the advantages of these two passivation methods, since it can tune device properties, improve performance, and provide a thin insulating layer for good surface stability. The sulfide passivation technology has been widely used to improve the performance of III-V semiconductor devices,[89] such as bipolar transistors,[90] field-effect transistors,[91] p-n structures,[92] lasers.[93, 94] The sulfidization requires the formation of bonds between sulfur atoms and surface atoms of the semiconductor, which can help to greatly slow down the oxidation of surface in the atmosphere. So the passivated surface will have long-time stability in atmosphere, water and heat, which is very important for further device applications. Experiments demonstrated that the passivation using organic sulfide such as thioacetamide[95] and octadecylthiol (ODT: $C_{18}H_{38}S$)[96 - 99] had better stability against reoxidation in air than inorganic sulfide. In this chapter, surface states in ZB-structured InAs NWs were totally eliminated by surfaces passivation and the ODT SAM showed very good stability.

4.2 Passivation methods

InAs NWs were grown on InAs substrate (see Fig. 4.1) using MOCVD. The growth method, growth mechanism and crystal structure characterization of these InAs NWs have been published.[100] Two different structured samples were used for passivation experiment, one has ZB structure and the other has WZ structure.

The WZ NW has cylinder shape with a diameter of around 70 nm. The ZB NW has a tapered shape with the diameter around 50 nm at tip and more than 100 nm at bottom. So quantization effects should not be expected here. To avoid collecting PL signal from InAs substrate, the NWs were dispersed onto Si substrate for passivation and PL measurement.

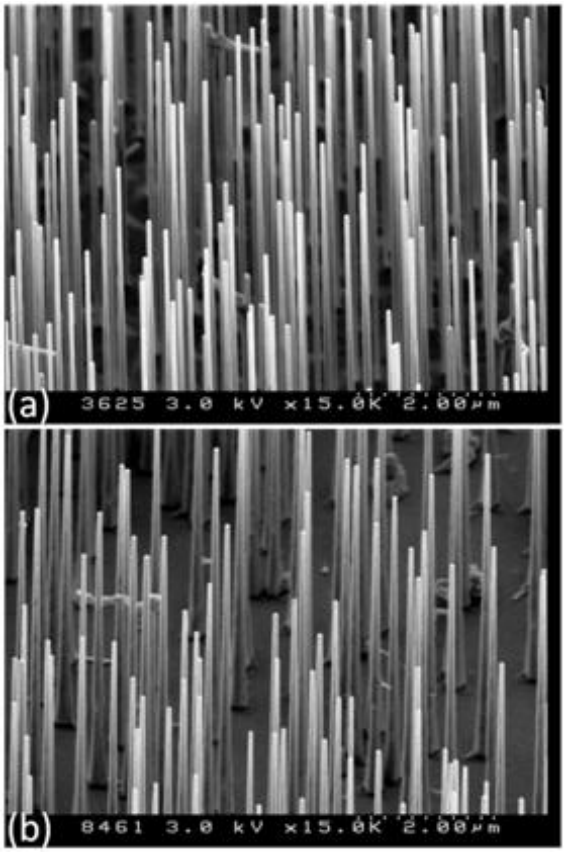

FIG. 4.1 SEM images of as-grown InAs NWs with two different structures (a) wurtzite and (b) zinc blende.

Different recipes were tested to identify the optimum procedure, including the acid or base for surface etching, reaction temperature and concentration of ODT solution. The following introduced the optimum recipe we used for surface passivation is 5 mM ODT/ethanol/NH_4OH solution. To prepare it, 143 mg of ODT (purchased from Alfa Aesar) was dissolved in 100 ml anhydrous ethanol, then 9 parts of this solution were mixed with 1 part aqueous ammonium hydroxide (NH_4OH 30%, ACS plus grade). Anaerobic environment during processing was rigorously controlled to form a stable, thin, dense and defect-free surface. The samples were first extensively degreased by rinsing in high purity organic solvents acetone and isopropanol (IPA) respectively for more than half hours, and then dried in helium gas flow. Removal of native oxide layers can improve the bonding of the adsorbing ODT molecules to the NW surfaces. The native oxides were etched by rinsing in aqueous hydrofluoric acid, which has been demonstrated to be a very effective oxidation layer removal method for III-V semiconductor.[101] Because freshly etched III-V semiconductor surfaces can be quickly reoxidized in air, it is important to remove the dissolved oxygen in all the solutions including deionized (DI) water, ethanol, IPA, hydrofluoric acid and the ODT/ethanol/NH_4OH. These solutions were bubbled with dried helium gas for more than 40 min, then immediately sealed in the airtight stainless steel containers. These containers were sent to nitrogen-purged glovebox where the samples were etched by hydrofluoric acid etching and rinsed in the ODT solution. The samples were dipped in the 1:1 (v/v) solution of DI water and 49 wt % hydrofluoric acid in plastic beaker for 2 s, rinsed in air-free DI water, and then

rinsed in air-free anhydrous ethanol. After that, the samples were immediately placed in the fused quartz ampoule with ODT solution. A freeze-pump-thaw method is utilized to degas the solutions and create a strict anaerobic environment. The open end of the ampoule was closed by means of an o-ring union/stopcock-valve assembly. The closed ampoules/stopcock with samples and solution were then transferred to the high vacuum manifold, where the sample/solution was frozen under liquid nitrogen. This freezing process was done gradually from the bottom up so any dissolved gases could be excluded by solidification. All the gases released during solidification were evacuated by dynamic pumping to high vacuum and then the ampoule was sealed using the H_2/O_2 glassblowing torch. The sealed ampoule was incubated in a drying oven at temperature of 60 ℃ for more than 24 hours. It required 26 hours to achieve the fully covered ODT film.[114] After that, the samples were taken out of the ampoule, rinsed with ethanol to remove the physically absorbed ODT molecules and blown dry with helium gas. Then the samples were ready for PL measurements.

PL measurements were carried out before and after passivation using the MIR micro-PL setup. The InAs NWs were excited by the Ti:Sapphire laser. Focused by a long focal-length lens, the laser beam was directed onto the sample at off-axis incidence. The PL signal was collected along the substrate normal direction by the all-reflective lens (15×). Then it was coupled to the spectrometer with a 300 grooves/mm grating and directed into liquid nitrogen cooled InSb photodiode detector. An optical chopper in the excitation laser beam and a lock-in amplifier connected to the detector were used to suppress detector noise. Samples were

placed in a microscope cryostat (under vacuum) with liquid helium cooling for low-temperature PL measurements. A temperature controller is used to enable temperature-dependent PL measurements.

4.3 PL Characterizations before and after passivation

PL measurements were performed on both WZ- and ZB-structured InAs NWs before passivation together with an InAs wafer for comparison at the temperature of 10 K. Many spots were measured over the samples and PL spectra from four different spots on WZ and ZB samples were shown in Fig. 4.2 (a) and (b). As shown in Fig. 4.2, the PL emission from InAs wafer has a peak position of around 2.97 μm and a FWHM of around 95 nm. Compared to the very narrow peak from InAs wafer, the PL peaks from unpassivated WZ and ZB NWs cover a very large wavelength range from ~ 2.6 μm to ~ 4.3 μm, which may come from surface states emissions. In general, there are two kinds of surfaces state emissions in InAs: one is near-band-edge and the other is deep-in-band-gap. The native surface defects such as antisite, vacancy, and dangling bond in InAs can pin the Fermi level above the bandgap due to the electronic and lattice rearrangement at the surface.[102] The Fermi-level pinning as well as the surfaces or interfaces states can be caused by the interaction between oxygen adatoms and the semiconductor.[103] Therefore, the deep-in-band-gap emissions from InAs NWs may be caused by the existence of large density of chemisorbed oxygen on the surfaces. After passivation, PL signals were collected from many different spots of the two NW samples at 10 K to test the uniformity of ODT layer. Fig. 4.2 (c) and (d)

respectively show four typical PL spectra observed from fresh-passivated WZ and ZB samples. Obviously, the very wide PL peaks completely disappeared after passivation instead very strong and narrow peaks were observed. This confirmed the origins of surface states emission from unpassivated NWs.

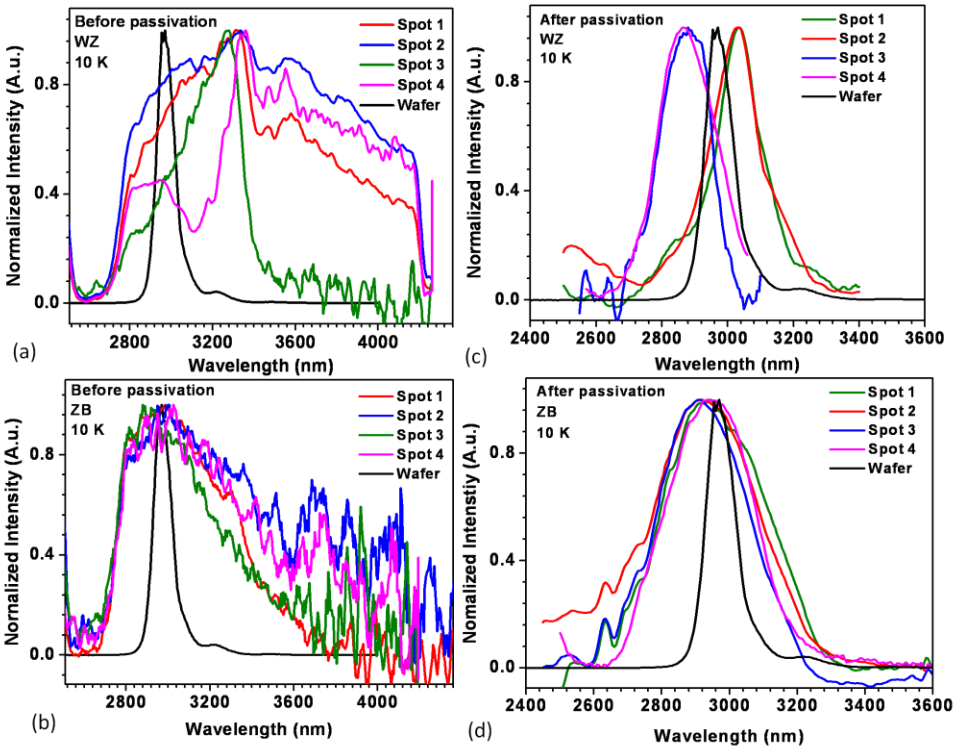

FIG. 4.2 PL spectra of WZ and ZB InAs NWs compared with InAs wafer: (a), (b) before passivation and (c), (d) after passivation. The spectra from different measured spots for each sample are shown.

As shown in Fig. 4.2 (c), two different PL peaks were observed on the passivated WZ NWs at 10 K. One of them (peak a) is very strong, narrow and located at 2.98 μm with a FWHM of 88 nm. It has similar peak position and width with the one from wafer which is located at 2.97 μm with a peak width of around 95 nm. Fig. 4.3 (a) shows how this peak changed after a series of treatments. To test the stability of the ODT monolayer and its resistance to surface reoxidation in air, PL measurements were performed again after the sample was stored in the air for 21 days at room temperature. The obtained peak has a FWHM of 92 nm, which is almost same with the 88 nm from fresh-passivated sample. Thus these passivated NWs are very stable in air. After that, the sample was stored in air for another two weeks and then annealed in air for half hour at 100 ℃. The peak became wider and moved deeper into the band gap. The reappearance of these deep-in-band-gap surface states after annealing may be caused by the reduced surface coverage of ODT layer, lower percentage of ODT-InAs surface bonds and the formation of oxide at the InAs surface. So we can see that passivation was very effective to eliminate deep-in-band-gap surface states. The other peak (peak b) is located at 2.86 μm and has higher energy than band-edge emission of InAs wafer (2.97 μm). It has a FWHM of 174 nm, wider than peak a (88 nm) and the band-edge peak from wafer (95 nm). After 21 days stored in air, the obtained PL peak has a FWHM of 182 nm, only 8 nm wider than before, which means very good air stability. After storing in air for another two weeks, the sample was annealed in air for half hours at 100 ℃. The obtained PL peak was much weaker and wider with a FWHM of around 314 nm. As shown in Fig. 4.3 (b), the peak

shape of the higher energy edge changed very little through these treatments, but the lower energy edge becomes much wider after annealing. The reappearance of lower energy emissions confirmed again that the passivation was very effective to remove the deep-in-band-gap surface states. The annealing in air can desorb parts of the ODT layers, so portion of the NW surfaces may be reoxidized. But most of the ODT-InAs bonds still exist because the peak is still much narrower than the one before passivation.

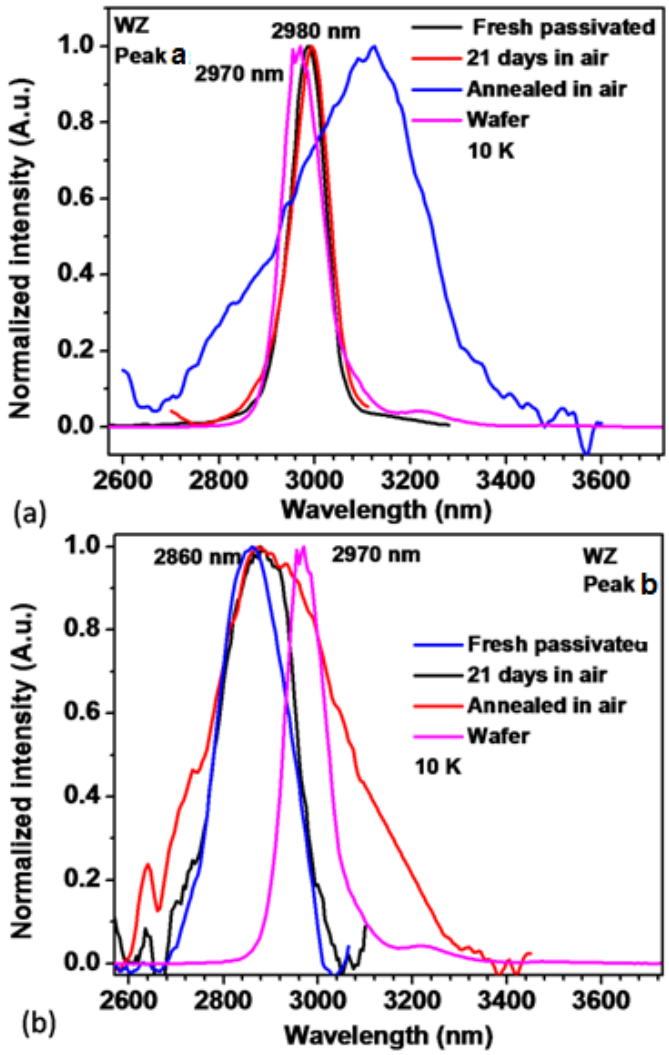

FIG. 4.3 PL spectra of two kinds of peaks (a) and (b) observed on WZ InAs NWs after the following treatments: fresh passivated, exposed in air for 21 days and annealed in air.

Temperature-dependent PL measurements were performed to find out the origins of the two peaks from WZ NWs. Fig. 4.4 (a) shows peak a has obvious red shift with increasing temperature. Fig. 4.4 (c) shows how the peak positions change with temperature compared with Varshni formula. Assuming parabolic band, momentum conservation and Boltzmann distribution of carriers, the PL peak energy is blue-shifted from bandgap by $k_BT/2$, where k_B is the Boltzmann constant and T is temperature. After correcting the measured peak position of peak a with $k_BT/2$, a very good agreement with the empirical Varshni formula[104] was obtained which describes the relationship of bandgap energy and temperature. Thus the peak a is from band-edge emission of InAs. As shown in Fig. 4.4 (b) and (c), peak b has red shift with increasing temperature, which indicates that it should be related with band-edge emission. It has higher energy than the band-edge emission, so it should contain above-band-edge emissions. Also because this peak is much wider than band-edge peak (see Fig. 4.4 (d)) and cannot be fitted with one Gaussian peak, we can conclude that peak b contain both above-band-edge surface state emission and band-edge emission.

.

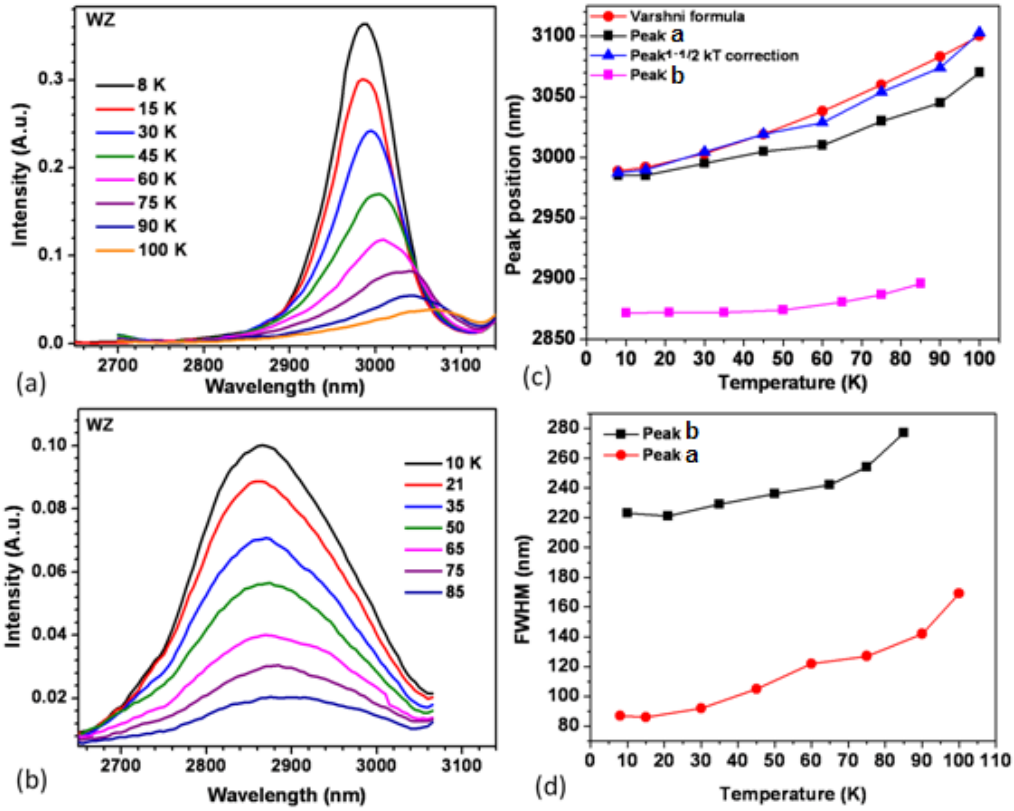

FIG. 4.4 Temperature-dependent PL spectra of the two peaks: peak a (a) and peak b (b) after 26 days stored in air. (c) and (d): the peak position and width change with temperature.

The same passivation procedure was also carried out on ZB NWs. A PL peak at around 2.85 μm with a FWHM of 255 nm was observed from the fresh-passivated NWs (See Fig. 4.5). The PL peak became much narrower after passivation. The high-energy edge of the peak is much stronger and the low-energy tail is totally disappeared, which further confirms that passivation has effectively eliminated the deep-in-band-gap surface states. The peak width has almost no change after stored in air for more than 5 months, indicating the very good stability of ODT layer in air. The stability in aqueous solutions is another very critical property for applications of SAMs-protected material. To test the humidity stability of the ODT layer, the sample was rinsed in DI water for 15 hours at room temperature after stored in air for 27 days. Then the sample was dried using nitrogen gas and put into the cryostat for PL measurements. As shown in Fig. 4.5, the FWHM of the peak changed from 255 nm to 310 nm after water rinse. Such small widening means most ODT-InAs bondings are not broken, which is more stable than the reported ODT-passivated InAs film.[105] According to their characterization, the ODT films were completely removed by soaking in DI water for 17 hours. The passivated ZB NWs samples were annealed at 100 ℃ in ambient air for half hours to test their thermal stabilities. The FWHM of the peak changes from 255 nm to 380 nm after annealing. Similar to the peak after water rinse, the high-energy edge of the peak changed very little, but the lower-energy edge moves toward lower energy, which makes the peak wider. So some deep-in-band-gap surface states reappeared after annealing or rinsing in water. But the peak is still much narrower and stronger than the one before passivation, which

means the ODT-InAs bonds were not completely broken though the molecular packing density of ODT was reduced. Fig. 4.5 (b) shows the temperature-dependent PL spectra from the passivated ZB sample. The peak has red shift with increasing temperature and shows the similar tendency with Varshni formula, meaning that band-edge emission should be included. But this peak has much shorter wavelength than the calculated one from Varshni formula (See Fig. 4.5 (c)). Fig. 4.5 (d) shows that the peak is wider than peak a and b form WZ samples. As confirmed before, peak a comes from band-edge emission, and peak b consists of both band-edge and above-band-edge emissions. Therefore, the peak from ZB NWs should contain both above-band-edge surface states and band-edge emissions.

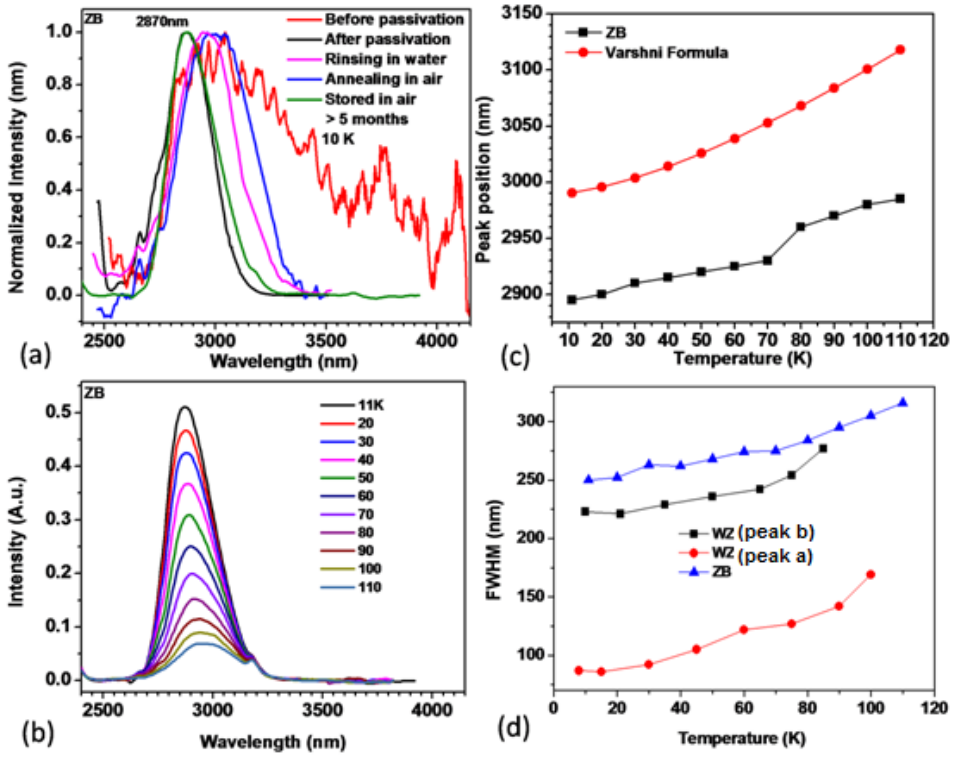

FIG. 4.5 (a) PL spectra of ZB InAs NWs after various treatments including fresh passivated, exposed in air more than 5 months, rinsed in water and annealed in air. (b) Temperature-dependent PL spectra from passivated ZB NWs. (c) The peak position changs with temperature compared to Varshni formula. (d) Peak width change with temperature compared to the ones from WZ NWs.

The peak widths measured on both WZ and ZB samples after various treatments were summarized in Table 2.

Table 2: Peak width of passivated InAs NWs after various treatments.

Sample	Fresh passivated (nm)	Store in air (nm)	Rinse in water (nm)	Anneal in air (nm)
WZ (peak a)	88	92 (21days)		675
WZ (peak b)	174	182 (21days)		314
ZB	255	260 (5 months)	310	380

The sulfur treated GaAs surface was found to be terminated with approximately a monolayer of sulfur bonded to both Ga and As atoms and the As-S bonds were removed while Ga-S bonding remained after annealing.[109] Ohno et al.[107, 108] reported a first-principles study of the structural and electronic prosperities of sulfur passivated GaAs surfaces. They found that the sulfur atoms were adsorbed on the bridge site on the GaAs surface and more tightly bonded to Ga atoms than As atoms. Similar with GaAs, three bonding states including In-S, As-S and S-S were observed on the surfaces of ODT-passivated InAs. The In-S bonds are much stronger and more stable upon annealing than As-S bonding.[111] Both experiment and theory calculation showed the sulfur passivation remarkably reduced midgap-surface-sates density.[107, 108] This is consistent with our results that deep level emissions in the band gap are totally removed after sulfur passivation. The sulfur passivation can greatly reduce the surface recombination

velocity[109] and the density of surface states, as evidenced by the increase of PL peak intensity and the narrowing of peak width in our experiments. The comprehensive examination of ODT layers prepared on InAs[114] demonstrated that the surface oxide was removed and the surface was covered with a SAM of sulfur with the thickness of around 2 nm. The sulfur-passivated InAs surfaces were explained by a "layer-cake" S/In/As structure model: the sulfur was chemisorbed on the In-terminated InAs surface and the alternating In and As atomic layers were formed.[106] They identified the components on the fresh passivated InAs surface: In-S (~1.5 ML), In-Ox (~1.2 ML), As-O (0.2~0.4 ML), As-S (possibly up to 0.2 MLs), where ML is monolayer. The very small amount of As-S component confirmed the exclusive sulfur bonding to In and the layer-cake model, which is likely a result of solubility differences between In-S and As-S in the basic passivating solutions. With increase of the air exposure, the In-S component and S coverage slowly decrease while the As-O_x and In-O_x increases. The sulfur lost in air exposure is through formation of volatile compounds. Therefore, we can see that the reappearance of light emissions from deep level in the band gap after annealing in air or rinsing in water in our experiments is probably caused by the broken As-S bonds and the reformation of As-O_x and In-O_x. As confirmed by our PL measurements, these sulfur passivated surfaces are very stable in air. The peak position and peak shape of surface state emissions are determined by the energy distribution of surface states and the quasi-Fermi energy level at the surface.[110] Typically, the maximum surface states density is distributed near the band-edge. [111, 112] Also because the Fermi energy of InAs was pinned above the conduction

band, the above- and near-band-edge emissions contribute most in the PL spectra and they cannot be easily and completely eliminated. This is consistent with our experiment result that the passivation can completely eliminate deep-in-band-gap surface state emission but sometimes some above-band-edge surface states still remain.

Because the surface can be easily re-oxidized during the deposition, it is very critical for a successful passivation to create an oxygen-free condition. As reported by Allara et al.,[114] the rigorous deoxygenation of the deposition solutions was very important to avoid the formation of an oxide layer before ODT molecules were attached to the surface. The presence of some oxides on the surface after the etching steps or reformed during the deposition process was found to be able to slow the formation of ODT layer. Shorter deposition time may also help to minimize the surface oxidation, but the thiol dimerization reaction is slow, so several hours or days are required. Therefore, a very strict procedure was utilized to create an oxygen-free environment in our experiments, including bubbling all the solutions, handling the process in glovebox, degassing the ODT solution by solidification and sealing the container during deposition. For comparison, a sample was obtained using a simplified procedure, in which degassing the ODT solution by solidification was not carried out. The samples were rinsed in the ODT solution, sealed in an airtight stainless steel container in the glovebox and then transferred to the oven at 60 ℃. It turned out that the obtained ODT layer had lower quality and worse stability. In addition, the ammonium hydroxide, which was added into the ODT/ethanol solution, helps to

further etch the native surface oxides during the deposition, thus minimize reoxidation and improve the binding of ODT molecules to NW surfaces.[96, 106] It found that the optimum ammonium hydroxide concentration was 3 vol % to form well-ordered SAMs,[96] which is the dose we used. Reaction temperature is another important parameter for depositing high-quality SAM of ODT. Two samples were treated strictly following the above procedure, except that one of them with reaction at room temperature and the other at 60 ℃. The PL results showed that the one at 60 ℃ had much stronger and narrower PL signal than the other one. The reason may be that surface of III-V semiconductor is very chemically active thus more energy is needed to compete against other surface reactions such as oxidation. In addition, the higher solution temperature can also help to increase the diffusion rate and assist the ODT molecules to fill the surface binding sites. The passivation was found to be very reproducible and reliable when all the conditions described above were satisfied.

4.4 Conclusions

By continuously etching away surface oxide and rigorous control of oxygen exposure during the procedure, InAs NWs were chemically passivated by the ODT SAM formation on the surface. The passivation process includes the following: wet chemical etch the surface with HF acid in the glovebox, degas all the solutions using helium purging, add ammonium hydroxide into the ODT solution, degas the reaction solution using freeze-pump-thaw method and seal the reaction container during deposition. Micro-PL measurements were performed to

characterize their optical properties before and after passivaiton. Before passivation, very wide surface states emissions are dominant. After passivation, the PL peaks become much narrower and stronger and the deep level surface states in the band gap were completely eliminated for both NWs. For WZ NWs, the band-edge emission was recovered when the surface states were completely removed. Those passivated NWs showed very good stability in very long time exposure in air, humidity and heat, which indicates the ODT layer can provide long-term chemical passivation to the surfaces. These passivated InAs NWs are very promising for their applications in optoelectronic and electrical devices. These results will be submitted to a journal soon.[116]

CHAPTER 5

CHARACTERIZATION OF LEAD SULFIDE MICROWIRES

5.1 Introduction to PbS

Lead sulfide (PbS) has many interesting properties and important applications in MIR optoelectronic devices including lasers, detectors and sensors. It has a rock-salt crystal structure with face-centered cubic unit cell. PbS is a direct narrow-band-gap semiconductor with a bandgap less than 0.5 eV at the L point of the Brillouin zone. PbS is very useful for fabricating lasers operating in the wavelength range from 2.5 to 4.5 μm. In this region, there are many gas absorption bands and lines such as CO and CO_2. So PbS lasers can be applied in high-resolution spectroscopy for scientific investigations especially in air pollution and toxic gas monitoring.[117] PbS exhibits many unusual properties with respect to other semiconductors. Due to the thermal expansion of crystal lattice and the interaction of electric carriers with phonons, PbS has a positive temperature parameter, which means its bandgap increases with the increase of the temperature.[118] The nonparabolic dispersion relationship has an important role in narrow-band-gap material, such as InAs,[119] InSb[120] and InN.[121] So a strong nonparabolic band structure should be taken into account for PbS. PbS has very high luminescence efficiency compared to the narrow-band-gap semiconductors in III-V group, because the Auger recombination efficiency of lead salt is one or two orders of magnitude lower than that of III-V materials with similar bandgaps.[122] One of the reasons for the low Auger recombination efficiency of

lead salt is that their approximate equality of the effective electron and hole masses, which makes it difficult to satisfy the laws of conservation of energy and momentum in triple collisions.[123] Auger recombination rate can be decided by the matrix elements of the Coulomb interaction.[124] So the large static dielectric constant (169) of PbS[125] results in longer Auger recombination lifetime. Lead salt diode lasers have been reported since 1960s.[126] The binaries PbS, PbSe, PbTe and their ternaries alloys such as PbSnTe, PbSnSe, PbCdSe, PbSSe have been used to fabricate lasers covering the wavelength range of ~3–30 μm.[127] Many kinds of PbS lasers have been made. Electrically pumped PbS diode laser with continuous wave (CW) emission at 4.32 μm was fabricated to operate at 4.2 K.[128] Stripe-geometry PbS diode lasers with large CW output power of around 50 mW and very high quantum efficiencies was developed in the 4.3 μm wavelength region at around 15 K.[129] The $Pb_{1-x}Sr_xS$/PbS double-heterostructure laser prepared by hot-wall epitaxy has an operation temperature of 245 K in pulsed emission and 174 K in CW emission at around 3 μm.[130] Optical pumped PbS laser was demonstrated to operate at CW mode up to 50 K and pulse mode up to 150 K.[131] Double-heterostructure $Pb_{1-x-y}Cd_xSr_yS$/PbS/$Pb_{1-x-y}Cd_xSr_yS$ lasers with PbS as an active layer grown by molecular beam epitaxy was reported to have the maximum operation temperature of 240 K.[132]

Semiconductor subwavelength wires (SWWs) are the wires with subwavelength cross-sectional dimension and they are demonstrated to be an ideal structure for lasers.[133-135] The SWWs can function simultaneously as gain materials, optical waveguides and Fabry-Perot cavities. Air around the wires

provides large electric and optical confinements, which can be utilized to make very high-efficient laser.[136] Different from planar heterostructure laser, the material choices for SWW laser are not limited by lattice mismatch to a substrate. For example, it is hard to mate PbS chip to a Si circuit chip because it is very difficult to grow PbS layer epitaxially and directly on Si substrate since their large lattice mismatch (9%). However, high-quality PbS wires have been synthesized on different substrates using many methods, including CVD, solution-phase, and template-assisted deposition.[137-142] In summary, PbS SWWs is a very promising candidate material for laser operating at MIR wavelength. However, to our best knowledge, no information about lasing emission from PbS wires has ever been reported. In this paper, laser oscillation was achieved from both dispersed single PbS SWW on sapphire substrate and as-grown PbS SWWs on silicon substrate by optical excitation using a mode-locked Ti:Sapphire laser.

5.2 Growth and characterization methods

PbS SWWs were grown in a 3-zone horizontal quartz tube furnace with stoichiometric PbS powder as the source material. The substrate, Si (100) with and without intentionally deposited catalysts (Au or Pb), was placed on a quartz plate at a low temperature zone of 400 ℃. The system was pumped to a pressure lower than 100 mTorr. During growth, 50 sccm (standard cubic centimeters per minute) nitrogen or argon including 5% hydrogen was introduced into the growth chamber which raised the pressure to ~15 Torr. After the furnace reached the target temperature, the PbS source boat was inserted into the center of the furnace

at high temperature zone of 600 ℃ via a magnetic loading rod. The PbS source powder was vaporized and deposited onto the substrates about 10 cm downstream from the source. A detailed description of the synthesis of PbS wires will be reported somewhere else.

The MIR micro-PL setup was utilized to study the MIR light emission properties of these PbS SWWs. A passively mode-locked Ti:Sapphire laser was used to optically excite the samples. The laser beam is directed towards the sample at normal incidence through an all-reflective objective lens (15×) and the laser beam diameter on the sample is around 5 μm. The PL signal was collected from the scattered light at surface normal direction through the same objective lens. After that, the signal was directed to a spectrometer with a 300 grooves/mm grating which yields a 0.2 nm spectral resolution. The spectrometer was coupled to a liquid nitrogen cooled InSb photodiode detector, which is connected to an optical chopper and a lock-in amplifier to suppress detector noise. The samples were mounted into a microscope cryostat (under vacuum) from Janis Research. The incident laser power was modulated by some neutral density filters for excitation-intensity-dependent PL measurements.

5.3 Band-edge emission and lasing

Fig. 5.1 (a) shows the SEM image of as-grown PbS SWWs on Si substrate with diameter of 1-4 μm and length of 10-50 μm. The wires stand on the substrate with a tilt angle. The HRTEM image (Fig. 5.1 (c)) shows that the fringe spacing of the lattice is around 0.298 nm, which matches with the [200] lattice spacing of

PbS. The SAD pattern of a typical wire shown in Fig. 5.1 (d) has a [001] zone axis and a rock-salt structure. The EDX spectrum in Fig. 5.1 (b) features the peaks corresponding to elements lead and sulfur with atom ratio of 56:43. It contains a little more lead than sulfur, which is caused by the lead rich ball-shaped tip of the SWWs. Some PbS wires were removed from Si substrate and dispersed onto a sapphire wafer for single wire PL measurements. The PL measurements were performed on both dispersed (Fig. 5.1 (e)) and as-grown (Fig. 5.1 (f)) PbS SWWs.

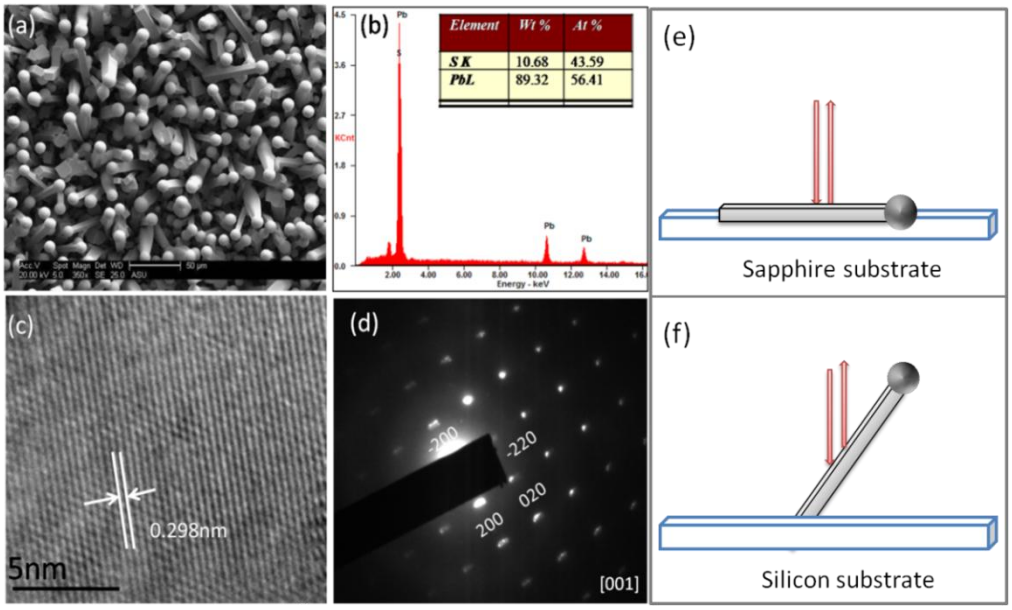

FIG. 5.1 (a) Top-view SEM image of the as-grown PbS SWWs and the (b) EDX spectrum. (c) HRTEM image and (d) SAED pattern of a typical PbS SWW. (e) Schematic of single SWW dispersed on sapphire substrate and (f) schematic of as-grown single SWW on silicon substrate. The laser beam excites the wire by on-axis incidence and the PL signal is collected along the sample normal direction through the same objective lens.

Temperature-dependent PL measurements were performed on the as-grown PbS SWWs from 77 K to 420 K at constant low level pumping. The obtained PL spectra are shown in Fig. 5.2 (a). The PL peaks have obvious blue shift with increasing temperature, which is a distinctive characteristic of band-edge emission of PbS. The PL spectra were simulated using a simple nonparabolic energy band model considering the direct and narrow bandgap of PbS. The anisotropy of PbS is very small, so isotropic average effective mass could be used: $m^*=0.085m_0$, m_0 is the free electron mass.[143, 144] Also because spin-orbit splitting of PbS is large compared to its bandgap, the nonparabolic energy-momentum dispersion relation from Kane' energy-wave-vector relation model is important here: $\hbar^2k^2/2m_e=E(1+\alpha E)$, where m_e is the effective mass of conduction-band-edge, α is the coefficient of nonparabolicity for the conduction band and can be approximated to $1/E_g$ assuming that spin-orbit splitting is large compared to the bandgap E_g. The temperature-dependence of the bandgap of PbS is determined by $E_g=263+(400+0.265\times T^2)^{1/2}$ (in meV, T in K).[117]

The temperature-dependent PL spectra of PbS were calculated based on the above nonparobolic energy band model and shown in Fig. 5.2 (b). A carrier density of $2.9\times10^{17}/cm^{-3}$ was used to obtain the best fit with the measured PL peak position. Same with the measured PL spectra, the calculated peaks have obvious blue shift with the increase of the temperature. Fig. 5.2 (c) shows a plot of central PL peak wavelength as a function of the temperature, determined from both measured and calculated PL spectra. Apparently, they match quite well with each other with a single density value, indicating that the PL emission from our SWWs

comes from band-edge emission of PbS. In addition, the PL emission intensity is still very strong even when the sample was heated to 420 K (see Fig. 5.2 (d)), which means these SWWs have very high crystal quality and luminescence efficiency.

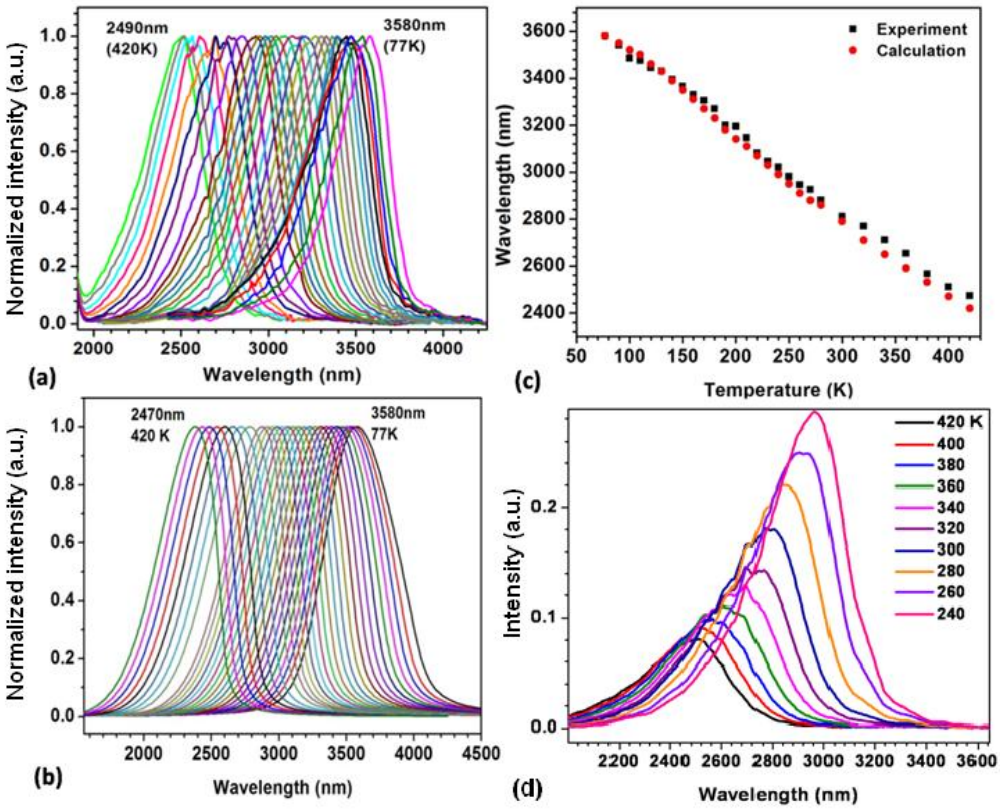

FIG. 5.2 Temperature-dependent PL spectra (normalized) of PbS SWWs obtained through (a) experiment measurement and (b) theoretical calculation. (c) shows the comparison of central peak positions from (a) and (b) as a function of temperature. (d) shows high-temperature PL spectra without normalization.

Lasing was observed from PbS SWW when the excitation intensity is higher than lasing threshold. Fig. 3 shows the laser oscillation of a single PbS SWW dispersed on sapphire substrate recorded at 10 K. The wire has a length of around 25 μm and a diameter around 1 μm. Fig. 3 (a) shows the near-threshold spectral evolution as a function of excitation laser power. Fig. 3 (b) shows the excitation-intensity dependence of the total emission peaks intensity below and after lasing threshold and (c) the same data on a log-log scale. At low pump laser power, a weak, broad and noisy PL peak was observed. The output intensity depends sublinearly on the excitation power, so it is dominated by spontaneous emission. When the pumping level increases to around 3.2 kW/cm^2, a narrow peak at around 4140 nm appears above the broad emission background, indicating that the population inversion starts to build up and amplified spontaneous emission begins. In this regime, the peak intensity exhibits a superlinear increase with pump laser power. As the laser power is increased further, a very sharp laser oscillation peak will finally dominate, which has intensity several orders of magnitude larger than spontaneous background. Such single-mode lasing peak originates from the longitudinal mode of Fabry-Perot resonant cavity formed by the two end surfaces of the wire. In this regime, the output intensity depends linearly on pumping laser power. According to these results, the lasing threshold for this PbS SWW is around 3.2 kW/cm^2 at 10 K, above which a sharp peak was observed with a FWHM of 4 nm, which is limited by the resolution of our detection system.

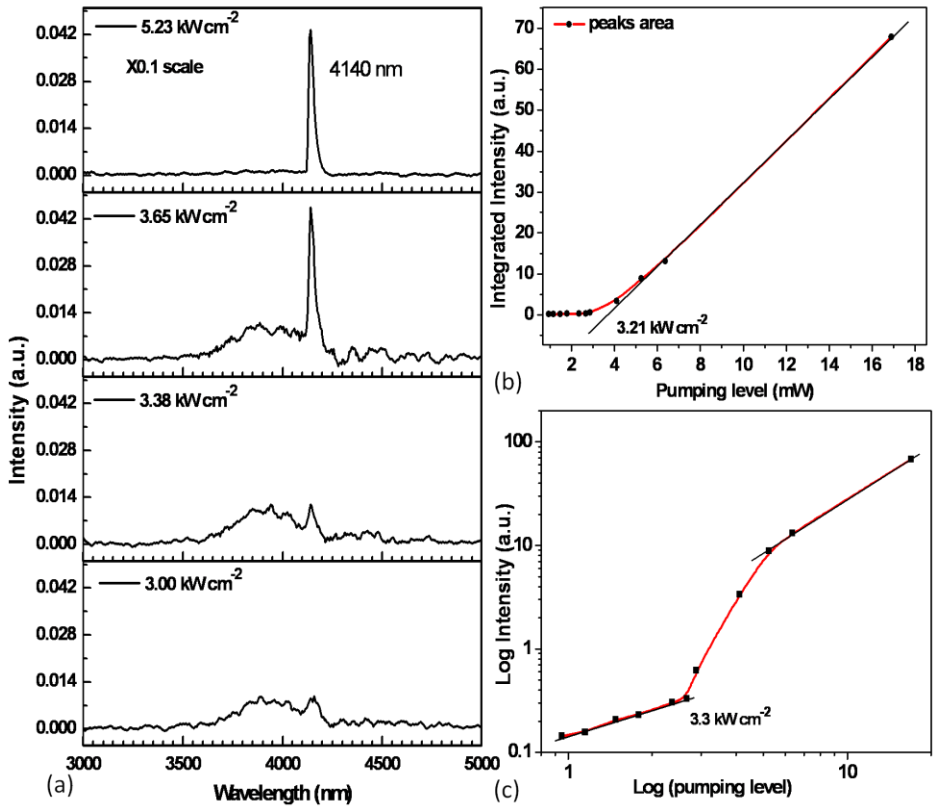

FIG. 5.3 Laser oscillation of a single PbS SWW dispersed on sapphire substrate recorded at 10 K. (a) Output spectra versus pump laser power near lasing threshold. (b) Excitation-intensity-dependence of PL peak intensity below and above lasing threshold. (c) The same data with (b) on a log-log scale.

The modes observed in the lasing spectrum as a function of power contains a very important implication of the quality factor and gain related with these modes. Fig. 5.4 shows the spectra of the cavity modes at pumping level well above the lasing threshold observed from a single PbS SWW dispersed on a sapphire substrate at 10 K. As shown in Fig. 5.4, two main lasing modes, peak 1 at around 3.58 μm and peak 2 at around 3.73 μm, were observed. With increasing pumping level, peak 1 with higher energy becomes stronger and narrower while peak 2 with lower energy becomes weaker and wider. This is caused by the blue shift of gain profile with the increase of the pump power due to band filling effects. In addition to the large shift between the lasing modes, a small blue shift of the individual cavity mode is also observed (Fig. 5.4). For each single mode, the peak position shifts to higher energy with increasing pump laser power, which is caused by the decrease of the refractive index due to the increase of carrier density.[145]

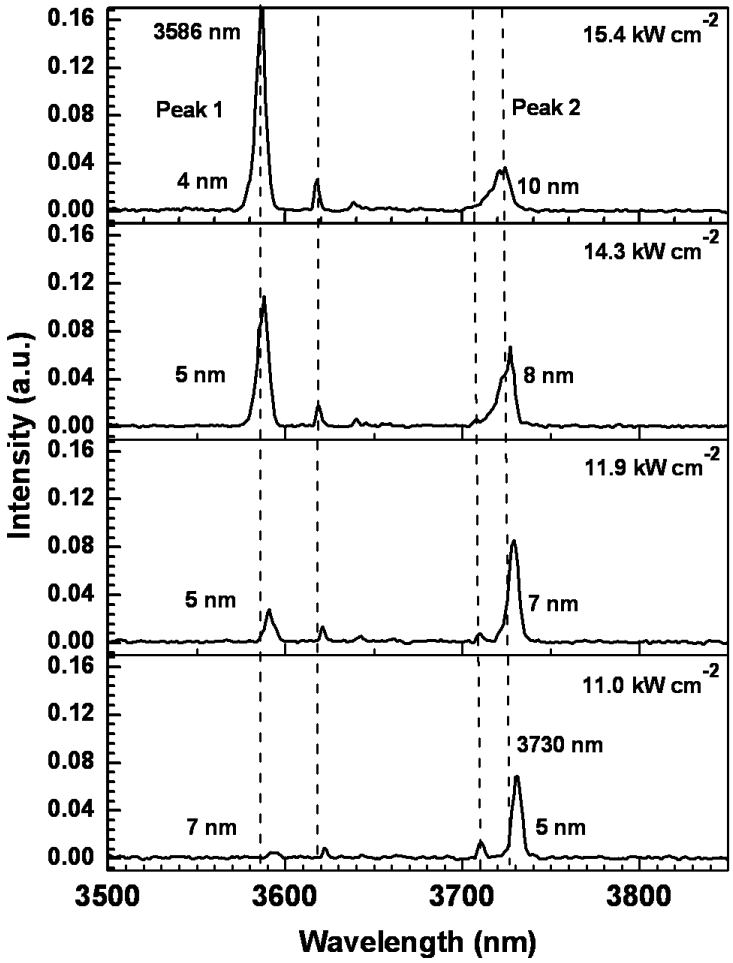

FIG. 5.4 PL spectra measured with pumping power higher than the lasing threshold for a single dispersed PbS SWW at different pumping laser powers at 10 K. Two main lasing modes were marked as peak 1 and 2. The FWHMs of the two peaks at different excitation intensity were indicated in the figures.

Fig. 5.5 demonstrated the excitation-intensity-dependent PL spectra collected from an as-grown PbS SWW on silicon substrate at 77 K, which clearly shows the transition from spontaneous emission to lasing. A very broad and noisy PL peak was observed at low pumping level. A sharp lasing peak with a FWHM of 4 nm appeared when the pumping intensity reaches around 25 kW/cm^2, which is higher than the lasing threshold of 3.2 kW/cm^2 at 10 K. This is consistent with higher threshold at higher temperature. Our measurements show the lasing threshold for the single as-grown SWW on silicon substrate is smaller than that of the single SWW on dispersed sapphire substrate. It may be caused by the large cavity loss due to the damages on the end surface during the sample preparation. The high cavity quality is very crucial to reduce cavity loss and initiate lasing. The cavity loss can also be caused by the smaller refractive index contrast between SWW and its surrounding. The PbS with a refractive index of 4.1[146] has much larger refractive index contrast with air than sapphire (~1.7). As shown in Fig. 5.1, most of the as-grown PbS SWW is surrounded by air except one small end in contact with Si substrate; while the dispersed PbS SWW has a large contact area with the sapphire substrate. Thus larger cavity loss is expected for the dispersed SWWs, which is consistent with the reported result that the cavity losses increase with the increase of the contact between NW and substrate.[147] Fig. 5.6 shows the temperature-dependent PL spectra from an as-grown PbS SWW, which clearly shows how the lasing mode shifts with temperature. The single mode lasing can be observed up to the temperature of 115 K. When temperature increases from 77 K to 115 K, the lasing peak has a continuous blue shift from 3910 nm to 3526 nm.

So the lasing mode can be tuned continuously by controlling the temperature, which is very useful to make optical sources for high-resolution spectrometers.

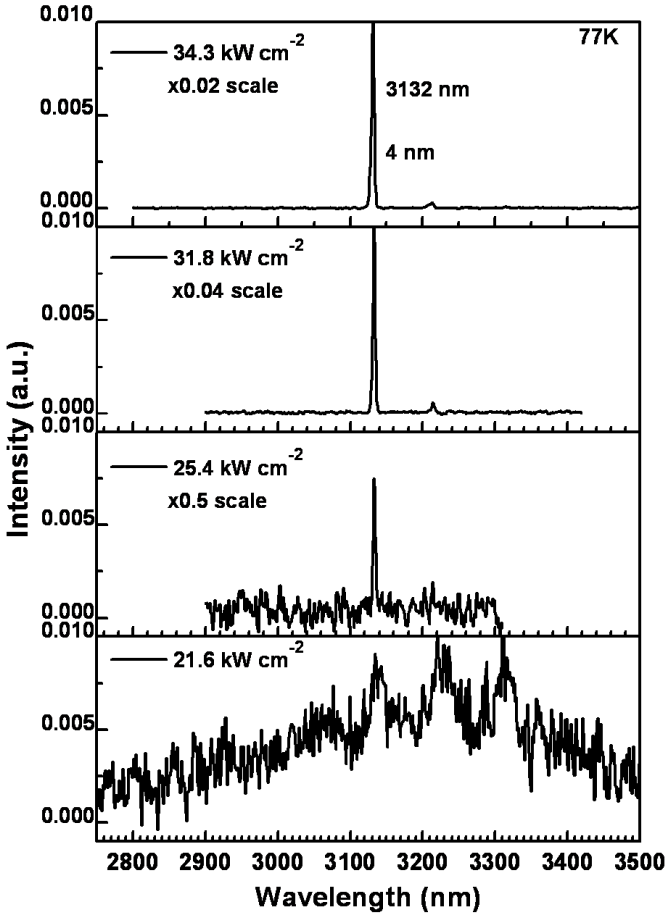

FIG. 5.5 Power dependent PL spectra from an as-grown PbS SWW at 77 K.

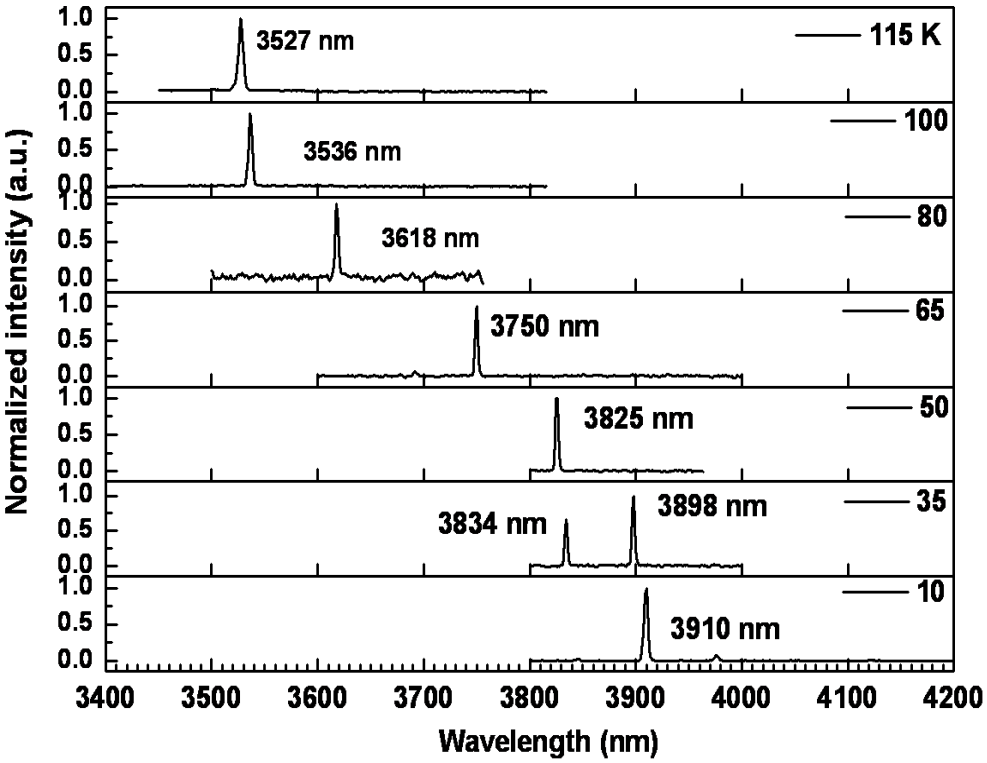

FIG. 5.6 Temperature-dependent PL spectra from an as-grown PbS SWW.

5.4 Summary

Very high quality PbS SWWs were grown on silicon substrate using CVD method, which shows very strong band-edge emission even at temperature as high as 420 K. Single mode MIR lasing at wavelength of 3~4 μm was observed up to 115 K from as-grown PbS SWW. The lasing mode can be tuned continuously by controlling the temperature, which is very useful to make optical sources for high-resolution spectrometers and other related applications. Our results represent a very important step towards fabricating electrically-driven high-temperature infrared lasers. The strong optical confinement in SWWs grown on silicon substrate allows for high-density integration of MIR SWW lasers in photonic integrated circuits. We believe that the future research will lead to exciting advances in infrared SWW optoelectronic and photonic devices. A paper is being prepared related with these results.[148]

CHAPTER 6

PL CHARACTERIZATION OF InP NWs AND InGaAs/InP COMPOSITION-GRADED HETEROSTRUCTURE NWs

6.1 Introduction to top-down grown NWs

Bottom-up and top-down are two main approaches to fabricate NWs. Though bottom-up approach is playing very important role in growing NWs, there are some problems existing such as difficult control of longitudinal structures and doping profiles, poor surface states and metal catalyst contamination. For the methods such as electrochemical deposition using anodic alumina oxide (AAO) or polymer templates, the process is relatively complicated and the crystal quality is poor. The top-down method is good for controlled fabrication of high density, vertically oriented NWs with desired vertical structures, which is critical to integrate NWs into any application platform including LEDs, transistors, sensors, solar cells and lasers. The inductively coupled plasma reactive ion etching (ICP-RIE) is an easy and large scale top-down fabrication method starting from MOCVD grown wafer which can incorporate very complicated complex longitudinal structures and doping profiles built in during the growth. In this way, the advantages of the well developed heterostructure growth technology and advanced ICP-RIE fabrication capability are combined. To examine the damages made by etching process and to check the crystal quality and luminescence efficacy of these NWs, PL measurements are necessary and very critical. The MIR micro-PL setup was utilized to do the PL measurements on the NWs.

6.2 Growth and characterization methods

Very dense vertical arrays of InP NWs and InGaAs/InP composition-graded heterostructure NWs were grown by Hua using ICP-RIE due to micro-masking effects.[149] Two wafer samples were used for NWs fabrication. The first one is a commercial n-type InP (S-doped) wafer (InPACT Inc, France) and the second one is a custom-made epitaxial sample grown by a commercial vendor (Landmark Technologies, Taiwan) based on InP (100) substrate. The designed wafer has a complex layers structures and doping profile with a core layer structure of InGaAsP (p) /InGaAs (i) /InGaAsP (n).

The NWs were obtained from the wafer pieces by etching in an ICP-RIE system. An etching cycle consists of one-minute of etching using a gas mixture of methane (CH_4) and hydrogen (H_2), followed by 10 s of O_2 plasma treatment in the same chamber. The cycle was repeated for tens of times in order to get desired length of the NWs. During the CH_4/H_2 etching, coil power was set at 125 W, while platen power was set at 75 W. Both RF power supplies are operated at 13.56 MHz. CH_4 and H_2 were introduced into the chamber at 30 sccm and 20 sccm flow rate, respectively. The process pressure during the CH_4/H_2 etching was 15 mTorr. The O_2 plasma flow rate was 49.5 sccm, the process pressure was 40 mTorr, and the coil power and platen power were 1000 W and 30 W respectively.

The representative InP NWs have cylindrical shapes as shown in Fig. 6.1. The diameter of the NWs are around 20-40 nm and the lengths are determined by the

numbers of etching cycles. The density of as-grown NWs is around 1.7×10^{14} cm^{-2}.

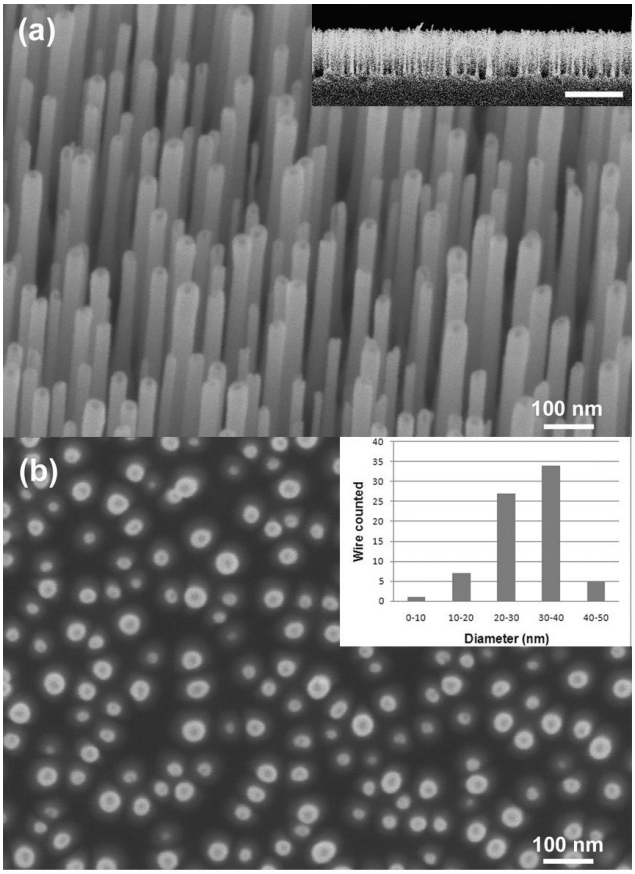

FIG. 6.1 SEM images of InP NWs. (a) titled view, inset of (a) cross-section view; (b) top view. Diameter variation of NWs is shown in inset of (b). The scale bar in inset of (a) is 1 μm.[149]

The wafer used for NWs growth has a complex longitudinal heterostructure as shown in Fig. 6.2 (a). There are around 14 different epitaxial layers grown on the Fe-doped semi-insulating InP substrate. Fig. 6.2 (b) shows the schematic of NWs etched from the epitaxial multilayer shown in Fig. 6.3 (a). Fig. 6.2 (c) shows the band-edge profiles of conduction and valence band across the layers (along the wire axis direction after etching). The PL measurements were performed using MIR micro-PL setup in our lab. The same measurement methods with InAs NWs are utilized here.

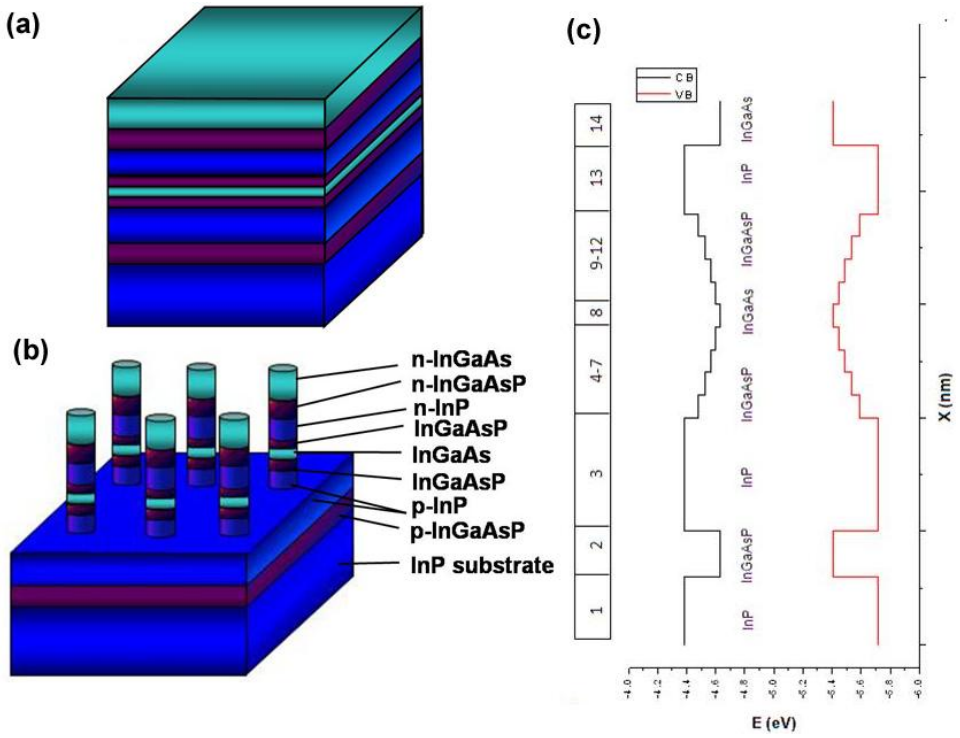

FIG. 6.2 (a) Schematic of the heterostructure wafer on InP substrate, (b) NWs after etching, and (c) band-edge profiles of conduction and valence band across the layers (along the wire axis direction after etching) and the schematic of multilayer of the NW. The relative thickness of each layer was shown. The following is the chemical details of each layer. layer1: InP substrate; layer2: highly doped p-type InGaAsP; layer 3: p-type InP buffer layer; from layer 4 to 7: p-type InGaAsP with different compositions; layer 8: $In_{0.53}Ga_{0.47}P$; from layer 9 to 12: n-type InGaASP with different compositions; layer 13: n-type InP; and 14: InGaAs layer.[149]

6.3 PL tests for crystal quality

PL measurements were performed to verify the quality of InP NWs. The InP NWs are scratched and dispersed onto quartz substrate to avoid the signal of InP substrate. The PL measurements were also done on the InP wafer, which is same as the wafer used for producing the NWs. Fig. 6.3 showed the PL spectra of InP NWs and wafer at room temperature. Both the PL peaks from NWs and wafer agree with each other perfectly at the wavelength of 936 nm. PL peak width is often a direct measurement of optical quality of samples. The large peak width may indicate the existence of surface states which is related to surface damages formed during the top-down growth process. The FWHM of the PL peak from these NWs is around 53 nm (75 meV), while it is around 28 nm (40 meV) for the wafer. Therefore, there should be surface damages caused by the etching process. Such surface states can be largely removed as I will show later for the case of InGaAsP NWs. Even without additional treatments, the peak width of our etched NWs is much smaller than the reported InP NWs grown using bottom-up approaches such as MOCVD system, which showed FWHM around 119 meV,[150] 90 meV,[150] and 84 meV.[152] This means that our NWs have much less surface states and thus the top-down etching process is a promising approach for producing high quality NW arrays.

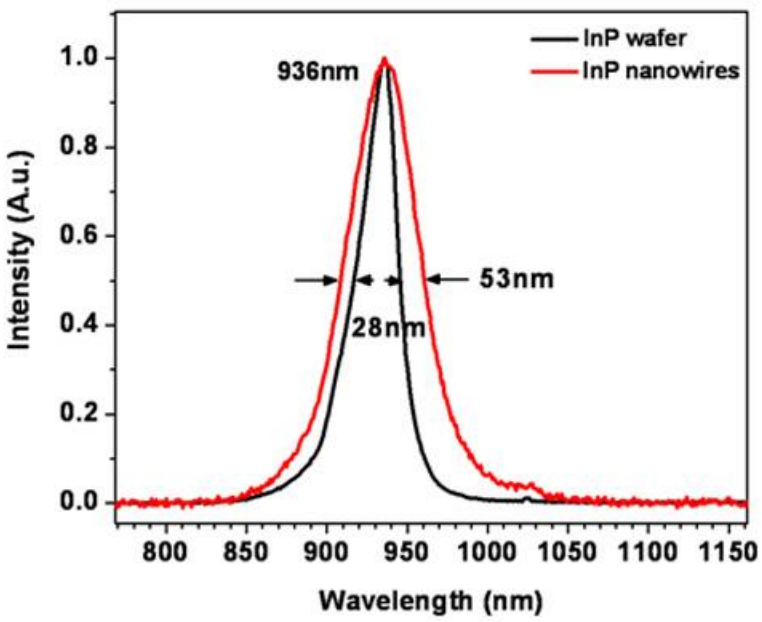

FIG. 6.3 Room-temperature PL spectra of InP NWs and wafer.

PL measurements of these heterostructure NWs and the wafer which is same as the wafer used for producing the NWs were performed at the temperature of 77 K. As shown in Fig. 6.4, the PL peak from the wafer is very narrow with FWHM of 35 nm (19 meV) at the wavelength around 1.530 μm, which originates from the InGaAs core. The FWHM of PL Peak from the NW is around 63 nm (33 meV), which is also very narrow though wider than that of the wafer. The increase of PL peak width of NWs compared to that of the wafer may be caused by the damages occurred during the etching process including possible changes in surface chemistry and ion collision induced surface damages. A series of chemical treatments were done to remove the damages by etching: 1) 5 minute oxygen plasma in Asher; 2) 1 minute wet etching in 1% HF; 3) Wet etching in H_3PO_4: H_2O=1:10 for 2 min; Repeat above step 1 to step 3 for 5 more cycles; and

followed by repeating step 1 and step 3 for 3 more cycles. After all these treatments, the PL spectra were recollected and shown in black line in Figure 6.4. The FWHM of PL peak from NWs after such treatments is around 35 nm (19 meV), which is almost indistinguishable that of the wafer. Obviously the PL peak was greatly narrowed. So these chemical treatments work very well to improve the quality of heterostructure NWs. The PL width of InGaAs NWs obtained using MOCVD[153-155] or MBE[156] are generally larger even at lower temperature: 15-30 meV at 4.5 K,[153] 30-60 meV[155] at 4 K, 87 meV at 14 K for InGaAs/GaAs core-shell NWs and the peak width is even larger for pure InGaAs NWs.[156] So our top-down approach of combining etching and subsequent treatments can produce very high-quality heterostructure NWs.

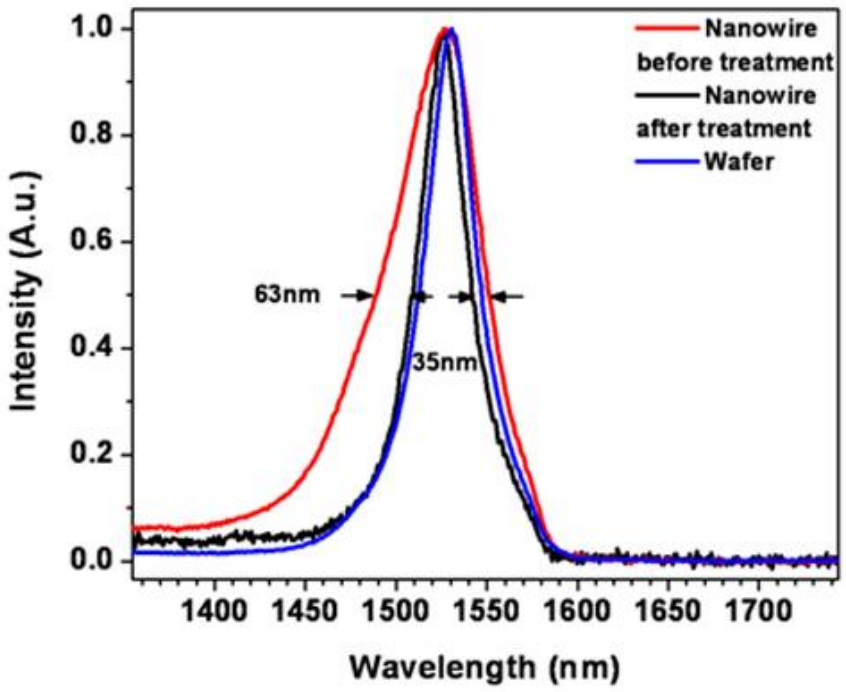

FIG. 6.4 PL spectra at the temperature of 77 K from the heterostructure wafer (blue line), heterostructure NWs before (red line) and after (black line) chemical treatments.

6.4 Summary

Vertical array of InP NWs and InGaAs/InP composition-graded heterostructure NWs were fabricated using ICP-RIE with a CH_4/H_2 gas mixture. The PL spectra from the InP NWs and InGaAs/InP heterostructure NWs were comparable to those from InP wafer and InGaAs/InP epitaxial wafer which are same as the wafers used for producing NWs. Moreover, the PL spectra from the InP and InGaAs/InP heterostructure NWs showed the narrowest linewidth compared to similar NWs of similar materials grown by bottom-up approaches such as MOCVD or MBE. All of these indicate the very high optical quality of our etched NWs, so this is an important alternative top-down approach for producing high quality NWs compared to the bottom-up approaches. It combined the best of the heterostructure wafer growth with the advanced fabrication techniques to solve the challenges in NW fabrication. In addition, the compatibility with the standard III-V fabrication and the related scalability make this approach appealing as a large scale operatable way of producing NW-based electronic and optoelectronic devices.

CHAPTER 7

TEM CHARACTERIZATION OF ERBIUM CHLORIDE SILICATE/Si AND ERBIUM SILICATE/Si CORE-SHELL NWS

7.1 Introduction to erbium chloride silicate (ECS) and erbium silicate (ES)

A new material with core-shell structure was synthesized via an Au-catalyzed CVD route,[157] which has high crystal quality without high-temperature annealing and shows very strong light emission at 1.53 μm. The wires have a diameter from several tens of nanometers up to around 250 nm, with their length from several to more than 10 μm. The XRD spectra[157] showed two patterns simultaneously existed. One was orthorhombic crystal structure with lattice parameters of a= 0.682 nm, b = 1.765 nm, and c = 0.616 nm, which agrees with the previously reported data (JCPDS card: No. 00-042-0365) of bulk ECS [Er_3 $(SiO_4)_2Cl$] and the other was cubic silicon (JCPDS card: No. 00-026-1481). These NWs were annealed at temperature of 1050 ℃ for 12 hours. The chloride was found to disappear after annealing. The XRD spectra[157] of these after-annealing NWs showed two structures, one was bulk ES (Er_2O_5Si, JCPDS card: No. 01-070-3279) with monoclinic structure and other was cubic silicon. So the annealing treatments transfer the material from ECS to ES. There are also some solid NWs existing among the core-shell NWs. We performed TEM-related measurements on these NWs before and after annealing to figure out their crystal structure and element composition, including STEM dark and bright field images, EDX element mapping in STEM mode, HRTEM images and SAD patterns.

7.2 Microanalysis of core-shell and solid NWs

Fig. 7.1 shows the low-Mag TEM, dark and STEM bright field images of the NWs, which clearly demonstrate the core-shell structure of these NWs. Fig. 7.2 (a) showed the bright field STEM image of a typical core-shell NWs. The EDX-TEM spectrum (See Fig. 7.2 (b)) collected from the shell and core regions of the NW (see the white square mark in Fig. 7.2 a) shows the peaks of elements Er, O, Cl, Si and Cu (from the copper grid). Fig. 7.2 (c)-(f) demonstrates the 2D EDX element mappings in STEM mode of this wire for the detected elements O, Er, Si, Cl, respectively. The results show that the concentration of Si in the core region is much larger than that in the shell region, whereas elements Cl, O, and Er are mainly distributed in the shell parts along the wires.

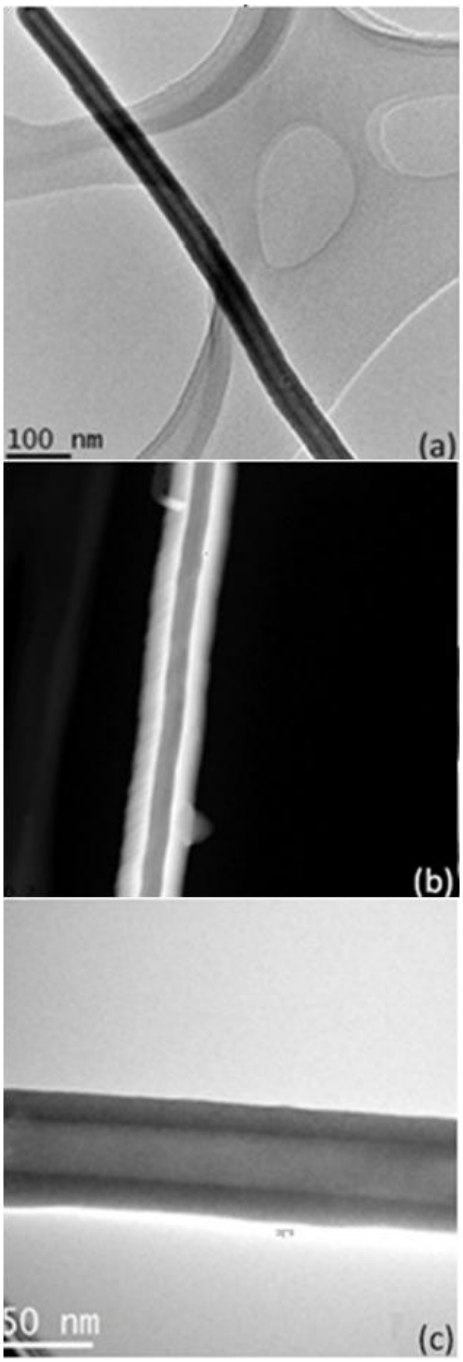

FIG. 7.1 Low-Mag TEM (a), dark-field (b) and bright-field (c) STEM images of the core-shell NWs.

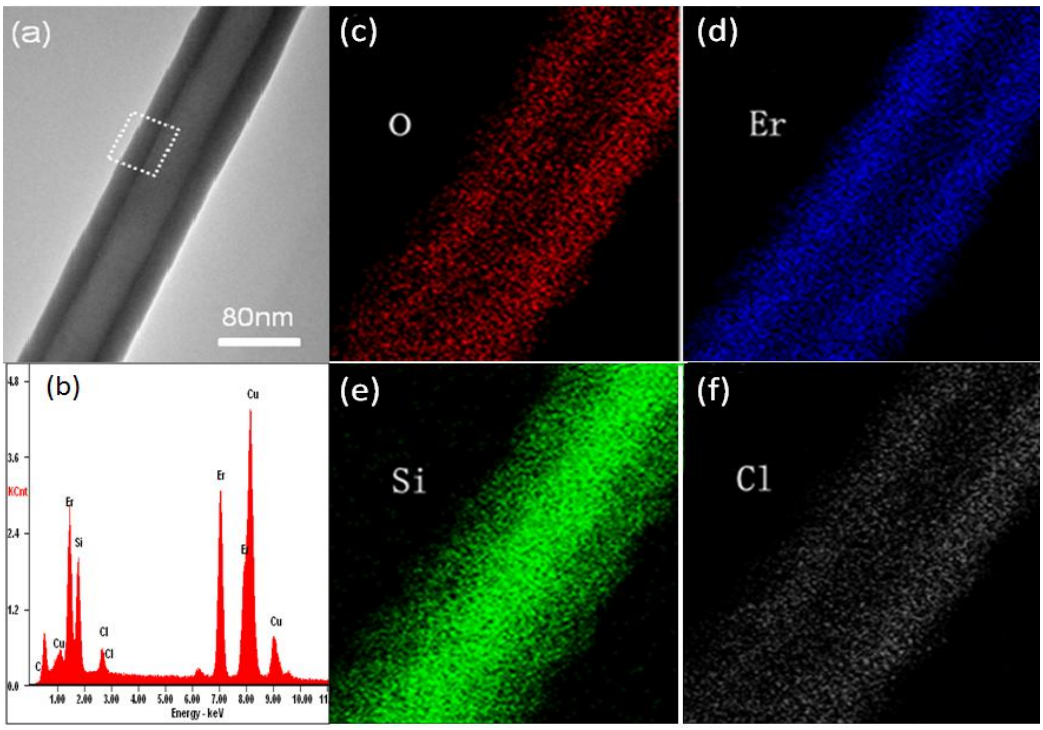

FIG. 7.2 STEM image of a typical core-shell NW without annealing (a) and its 2D element mapping (c)-(f) for the detected four elements, O, Er, Si, and Cl, respectively. (b) is the EDX spectrum collected from the shell and the core regions (see the white square mark in (a)).

Fig. 7.3 shows the HRTEM image taken from the interface domain between the core and the shell (see the marked area in Fig. 7.2 (a)), which demonstrate that both the core and the shell are of high-quality single crystalline with their interface sharp at the atomic scale. The core has a lattice spacing of 0.312 nm, consistent with the interplanar spacing of the {111} lattice planes of the diamond-cubic Si. The measured lattice spacing of the shell is 0.298 nm which is in good agreement with the {060} interplanar distance of orthorhombic structured ECS. Therefore, according to the combination of HRTEM images, EDX element mapping and XRD results, it was concluded that the investigated NWs were ECS/Si core-shell structure with the Si in the core and the ECS compound in the shell. There are some solid ECS NWs existing among the core-shell NWs, which show same crystal structure with shell as shown in Fig. 7.5 (a).

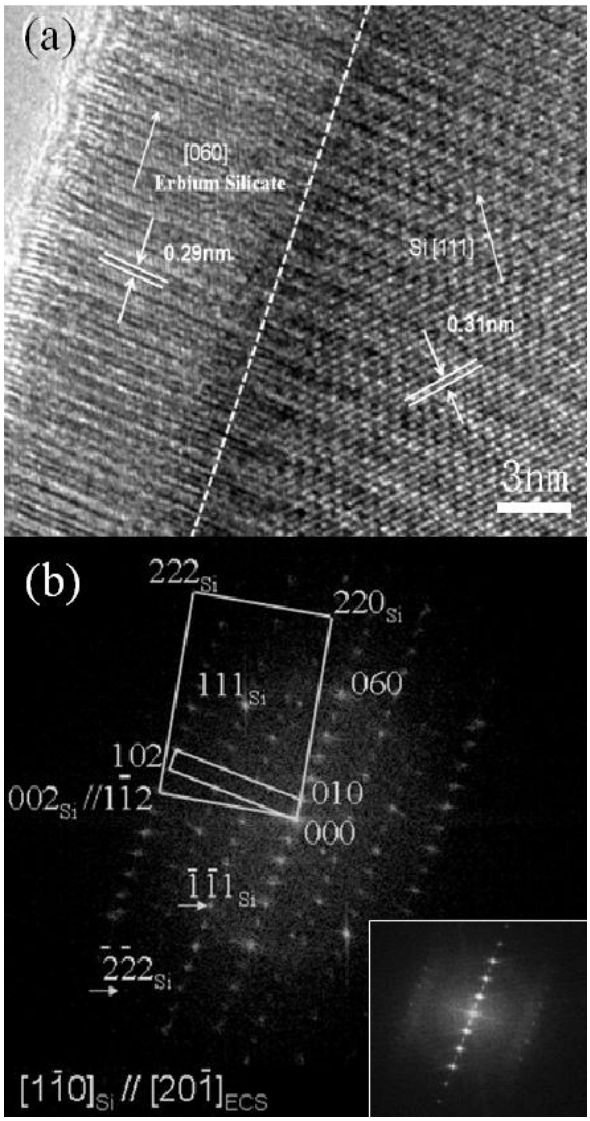

FIG. 7.3 HRTEM and corresponding FFT image of ECS/Si core-shell NW.

These core-shell NWs were annealed at 1050 ℃ for 12 hours, then HRTEM and SAD pattern were measured and shown in Fig. 7.4. The core and shell are still very good single crystalline after so high temperature annealing. The shell shows monoclinic structure, which consistent with ES instead of ECS. EDX analysis demonstrated the existence of Er, Si, O elements and the disappearance of chloride element. Therefore, the shell has changed from ECS to ES after the annealing. There are some solid NWs existing among the core-shell NWs. According to the HRTEM image and the corresponding FFT pattern shown in Fig. 7.5 (b), these NWs have the same crystal structure as the shell part, so they are ES NWs.

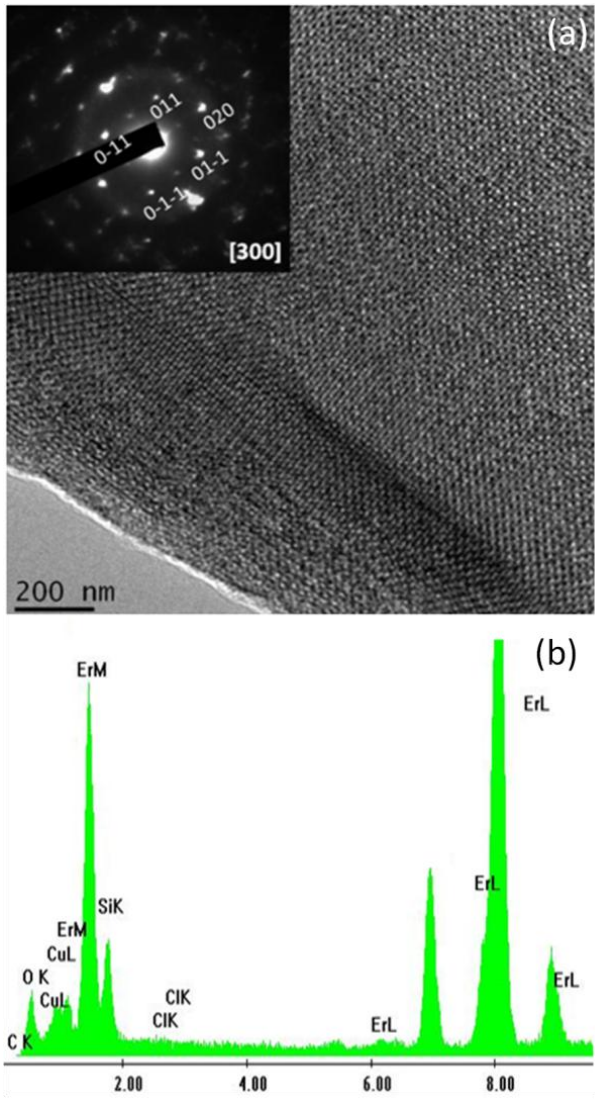

FIG. 7.4 ES/Si core-shell NW: (a) HRTEM image and corresponding SAD pattern of shell; (b) EDX spectrum.

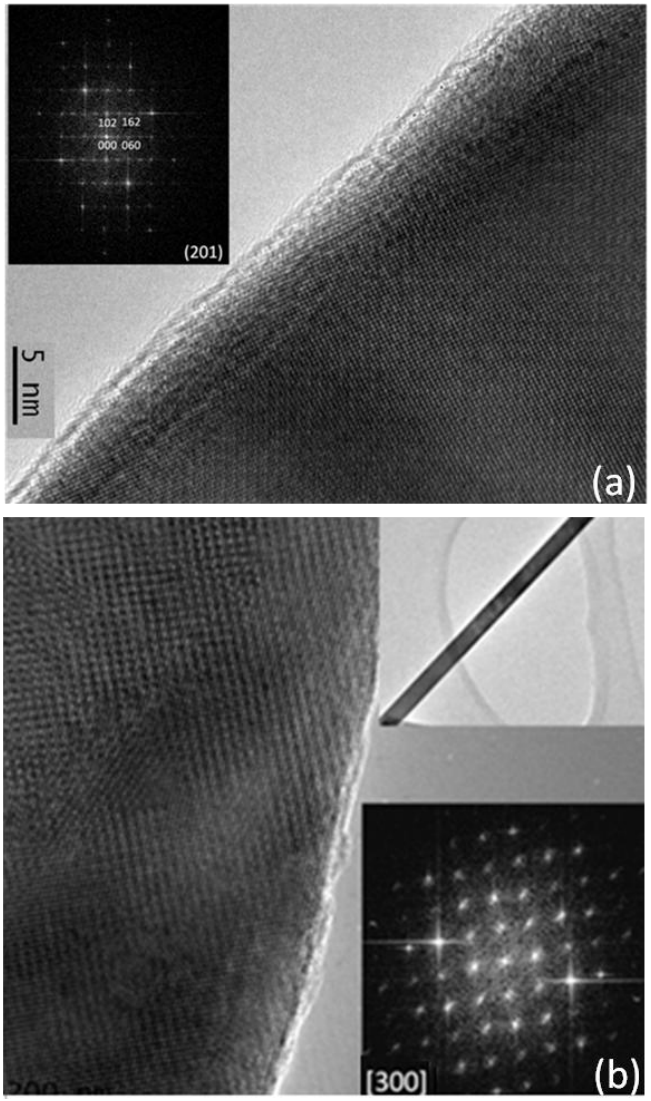

FIG. 7.5 HRTEM and corresponding FFT images of Solid ECS NW (a) and ES NW (b).

7.3 Summary

HRTEM, SAD pattern, EDX analysis and STEM images were utilized together to characterize the crystal structure and element composition of the new-developed ECS/Si, ECS/Si core-shell NWs and solid ECS, ES NWs. The core-shell NWs consist of orthorhombic-structured ECS shell and cubic-structured Si core. After annealing at 1050 ℃ for 12 hours, the chloride element disappeared and the ECS shell changed to monoclinic-structured ES shell. Solid ECS and ES NWs were respectively observed among the core-shell NWs before and after annealing. These ECS NWs provides a unique Si-compatible material for emission at 1.53 μm for optical communications and many other applications such as lasers.

CHAPTER 8

CONCLUSION AND OUTLOOK

8.1 Conclusion

The research reported in this dissertation involves the optical and microstructural characterization of various infrared nanowires (NWs) using micro-PL and TEM. The overall theme of this research is attempting to correlate the optical properties with the underlying microstructures of the crystals.

First, various InAs NWs with different crystal structures were systematically characterized using micro-PL and TEM, which is a part of a large overall effort in developing MIR optoelectronic NW devices by our group. Three types of PL peaks are observed: the band-edge peak, above- and below-band-edge peaks, which are related to the surface states and various donor or acceptor bound states. It turns out that the synthesis methods and growth substrates play an important role in crystal structures, growth mechanism, crystallinity and photoluminescence properties of InAs NWs. For MBE-grown InAs NWs, the ones grown on GaAs substrates have a WZ crystalline structure while the ones on Si substrates have a ZB structure. Usually, the InAs NWs grown on GaAs substrates have higher quality than those grown on Si substrates and both of them have higher quality than MOCVD-grown ones.

Recognizing the significant effects of surfaces states in InAs NWs, many efforts are made to develop an optimized recipe for passivating the NW surfaces. This is also related to the overall theme of relationship between optical properties

and surface microstructures. Surface microstructure can be modified to eliminate the unwanted features and to obtain the desired optical properties. The InAs NWs are successfully passivated by depositing a very stable octadecanethiol (ODT) self assembled monolayer (SAM) on surfaces. The surface states are greatly reduced and the band-edge emission is greatly recovered after passivation. Our studies show that the surface passivation greatly suppresses surface states recombination and inhibits the reoxidation of reactive InAs surfaces for long-time exposure in air, humidity and heat. The successful surface passivation of InAs NWs represents a very important step to extend their applications in optoelectronic and electrical devices.

Narrow-band-gap semiconductors were studied, which find their applications in MIR devices. It is difficult to achieve MIR lasing due to various inherent problems. Single mode lasing at wavelength of 3~4 μm was successfully obtained from as-grown single PbS wire with subwavelength diameter at temperature as high as 115 K. A very important aspect to note is that the lasing modes are continuously tuned by controlling temperature, which can be used as optical sources for high-resolution spectrometer for gas detection and other related applications. The strong optical confinement in PbS microwires (MWs) grown on silicon substrates allows for high-density integration of MIR subwavelength-wire (SWW) lasers in photonic integrated circuits.

When a new NW material is obtained, both micro-PL and TEM are very important methods to systematically characterize it for the optimum growth recipe and potential applications. Many different types of NWs have been successfully

characterized such as vertical array of InP NWs, InGaAs/InP composition-graded heterostructure NWs, ECS/Si core-shell NWs. Such characterizations provide important feedback for material growths and for future device developments.

8.2 Outlook

Although the optical properties and microstructures of the InAs NWs have been systematically studied, there are still some unsolved problems. For example, according to the theoretical calculation, the bandgap of WZ-structured InAs should be 50 meV larger than that of ZB-structured InAs. But we could not confirm this conclusively in our measurements. More research will be needed to fully understand these two different structured InAs NWs. Further improvement in the growth of InAs NWs is also essential to finally resolve this issue. This is also an ongoing issue within the community for other materials such as InP and GaAs.

Although there may be some surface states remained after ODT passivation and the passivation method can be further optimized, these passivated InAs NWs are ready for further device fabrications, such as detectors, sensors and high speed electrical devices, which will be explored in the future.

Although our experiments have demonstrated the capability of fabricating MIR lasers using PbS MWs, but there still a long way to finally achieve electrically-driven high-temperature infrared subwavelength lasers. In our future research, the lasing mechanism in these PbS MWs will be extensively studied, such as the lasing modes and their mode shift with temperature. More researches

are needed to determine an optimum design and eventually fabricate electrically pumped laser using these wires in MIR wavelength range, where there are many important applications in gas detections.

REFERENCES

[1]E. J. Menke, M. A. Thompson, C. Xiang, L. C. Yang, and R. M. Penner, "Lithographically patterned nanowire electrodeposition", Nature Materials **5**, 914 - 919 (2006)

[2]W. Lu and C. M. Lieber, "Nanoelectronics from the bottom up", Nature Materials **6**, 841 - 850 (2007)

[3]C. M. Lieber and Z. L. Wang, "Functional nanowires", MRS Bulletin, **32** (2007)

[4]Y. Li, F. Qian, J. Xiang, and C. M. Lieber, "Nanowire electronic and optoelectronic devices", Materials Today **9**, 18-27 (2006)

[5]J. Xiang, W. Lu, Y. Hu, Y. Wu, H. Yan, and C. M. Lieber, "Ge/Si nanowire heterostructures as high-performance field-effect transistors", Nature **441**, 489-493 (2006)

[6]Y. Cui, Z. Zhong, D. Wang, W. U. Wang, and C. M. Lieber, "High performance silicon nanowire field effect transistors" , Nano Lett. **3**, 149-152 (2003)

[7]B. Tian, X. Zheng, T. J. Kempa, Y. Fang, N. Yu, G. Yu, J. Huang, and C. M. Lieber, "Coaxial silicon nanowires as solar cells and nanoelectronic power sources", Nature **449**, 885-889 (2007)

[8]M. Law, L. E. Greene, J. C. Johnson, R. Saykally, and P. Yang, "Nanowire dye-sensitized solar cells", Nature Materials **4**, 455-459 (2005)

[9]E. Stern, J. F. Klemic, D. A. Routenberg, P. N. Wyrembak, D. B. Turner-Evans, A. D. Hamilton, D. A. LaVan, T. M. Fahmy, and M. A. Reed, "Label-free immunodetection with CMOS-compatible semiconducting nanowires", Nature **445**, 519-522 (2007)

[10]M. C. McAlpine, H. Ahmad, D. Wang, and J. R. Heath, "Highly ordered nanowire arrays on plastic substrates for ultrasensitive flexible chemical sensors", Nature Materials **6**, 379-384 (2007)

[11]G. Zheng, F. Patolsky, Y. Cui, W. U. Wang, and C. M Lieber, "Multiplexed electrical detection of cancer markers with nanowire sensor arrays", Nature Biotechnology **23**, 1294-1301 (2005)

[12]C. M. Lieber, "Nanowire superlattice", Nano Lett. **2**, 81-82 (2002)

[13]X. Duan, Y. Huang, R. Agarwa, and C. M. Lieber, "Single-nanowire electrically driven lasers", Nature **421**, 241-245 (2003)

[14]M. H. Huang, S. Mao, H. Feick, H. Yan, Y. Wu, H. Kind, E. Weber, R. Russo, and P. Yang, "Room-temperature ultraviolet nanowire nanolasers", Science **292**, 1897-1899 (2001)

[15]K. M. Rosfjord, J. K. W. Yang, E. A. Dauler, A. J. Kerman, V. Anant, B. M. Voronov, G. N. Goltsman, and K. K. Berggren, "Nanowire single-photon detector with an integrated optical cavity and anti-reflection coating", Optics Express **14**, 527-534 (2006)

[16]G. Zheng, F. Patolsky, Y. Cui, W. U. Wang, and C. M. Lieber, "Multiplexed electrical detection of cancer markers with nanowire sensor arrays", Nature Biotechnology **23**, 1294-1301 (2005)

[17]M. Lee, J. Im, B. Y. Lee, S. Myung, J. Kang, L. Huang, Y. K. Kwon, and S. Hong, "Linker-free directed assembly of high-performance integrated devices based on nanotubes and nanowires", Nature Nanotechnology **1**, 66-71 (2006)

[18]R. S. Friedman, M. C. McAlpine, D. S. Ricketts, D. Ham, and C. M. Lieber, "Nanotechnology: high-speed integrated nanowire circuits", Nature **434**, 1085 (2005)

[19]H. Kind, H. Yan, B. Messer, M. Law, and P. Yang, "Nanowire ultraviolet photodetectors and optical switches", Adv. Mater. **14**, 158 (2002)

[20]C. Thelander, H. A. Nilsson, L. E. Jensen, and L. Samuelson, "Nanowire single-electron memory", Nano Lett. **5**, 635-638 (2005)

[21]M. Law, J. Goldberger, and P. Yang, "Semiconductor nanowires and nanotubes", Annu. Rev. Mater. Res. 34, 83-122 (2004)

[22]P. J. Pauzauskie and P. Yang, "Nanowire photonics", Materials Today **9**, 10 (2006)

[23]X. Duan and C. M. Lieber, "General synthesis of compound semiconductor nanowires", Adv. Mater. **12**, 298-302 (2000)

[24]F. Wang, A. Dong, J. Sun, R. Tang, H. Yu, and W. E. Buhro, "Solution-liquid-solid growth of semiconductor nanowires", Inorg. Chem **45**, 7511-7521 (2006)

[25]M. J. Bierman, Y. K. Albert Lau, A. V. Kvit, A. L. Schmitt, and S. Jin, "Dislocation-driven nanowire growth and eshelby twist", Science **320**, 5879, 1060-1063 (2008)

[26]Y. Wang, V. Schmidt, S. Senz, and U. Gösele, "Epitaxial growth of silicon nanowires using an aluminium catalyst", Nature Nanotechnology **1**, 186-189 (2006)

[27]P. Mohan, J. Motohisa, and T. Fukui, "Controlled growth of highly uniform, axial/radial direction-defined, individually addressable InP nanowire arrays", Nanotechnology **16**, 2903-2907 (2005)

[28]Y. Wu and P. Yang, "Direct observation of vapor-liquid-solid Nanowire Growth", J. Am. Chem. Soc. **123**, 3165-3166 (2001)

[29] X. Zhao, C. M. Wei, L. Yang, and M. Y. Chou, "Quantum confinement and electronic properties of silicon nanowires", Phy. Rev. Lett. **92**, 236805 (2004)

[30] J. Wang, M. S. Gudiksen, X. Duan, Y. Cui, and C. M. Lieber, "Highly polarized photoluminescence and photodetection from single indium phosphide nanowires", Science **293**, 1455-1457 (2001)

[31] A. V. Maslov and C. Z. Ning, "Reflection of guided modes in a semiconductor nanowire laser", Appl. Phys. Lett. **83**, 1237 (2003)

[32] H. C. Hsu, C. Y. Wu, and W. F. Hsieha, "Stimulated emission and lasing of random-growth oriented ZnO nanowires", J. App. Phys. **97**, 064315 (2005)

[33] B. Zou, R. Liu, F. Wang, A. Pan, L. Cao, and Z. L. Wang, "Lasing mechanism of ZnO nanowires/nanobelts at room temperature", J. Phys. Chem. B **110**, 12865-12873 (2006)

[34] P. Yang, H. Yan, S. Mao, R. Russo, J. Johnson, R. Saykally, N. Morris, J. Pham, R. He, and H. Choi, "Controlled growth of ZnO nanowires and their optical properties", Adv. Funct. Mater. **12**, 323 (2002)

[35] A. L. Pan, W. Zhou, E. S. P. Leong, R. Liu, A. H. Chin, B. Zou, and C. Z. Ning, "Continuous alloycomposition spatial grading and superbroad wavelength-tunable nanowire lasers on a single chip", Nano Lett. **9**, 784 (2009)

[36] R. Agarwal, C. J. Barrelet, and C. M. Lieber, "Lasing in single cadmium sulfide nanowire optical cavities", Nano Lett. **5**, 917-920 (2005)

[37] S. Gradečak, F. Qian, Y. Li, H. G. Park, and C. M. Lieber, "GaN nanowire lasers with low lasing thresholds", Appl. Phys. Lett. **87**, 173111 (2005)

[38] J. C. Johnson, H. J. Choi, K. P. Knutsen, R. D. Schaller, P. Yang, and R. J. Saykally, "Single gallium nitride nanowire lasers", Nature Materials **1**, 106, (2002)

[39] A. H. Chin, S. Vaddiraju, A. V. Maslov, C. Z. Ning, M. K. Sunkara, and M. Meyyappan, "Near-infrared semiconductor subwavelength-wire lasers", Appl. Phys. Lett. **88**, 163115 (2006)

[40] Y. Xiao, C. Meng, P. Wang, Y. Ye, H. Yu, S. Wang, F. Gu, L. Dai, and L. Tong, " Single-Nanowire Single-Mode Laser", Nano Lett. **11**, 1122-1126 (2011)

[41] R. Chen, T. D. Tran, K. W. Ng, W. S. Ko, L. C. Chuang, F. G. Sedgwick, and C. Chang-Hasnain, "Nanolasers grown on silicon", Nature Photonics **5**, 170 (2011)

[42] Y. P. Varshini, "Temperature dependence of the energy gap in semiconductors", Physica **34**, 149 (1967)

[43] T. Schmidt and K. Lischka, "Excitation-power dependence of the near-band-edge photoluminescence of semiconductors", Phys. Rev. B **45**, 8989 (1992)

[44] D. Li and C. Z. Ning, "Peculiar features of confinement factors in a metal-semiconductor waveguide", Appl. Phys. Lett. **96**, 181109 (2010)

[45] C. Z. Ning, "Semiconductor nanolasers", Phys. Stat. Sol. B, **247**, 774-788 (2010)

[46] S. L. Chuang, Physics of optoelectronic devices, Wiley, 1995

[47] J. Singh, optoelectronics: an introduction to materials and devices, McGraw-Hill, 1996

[48] Transmission electron microscopy: a textbook for materials science. Basics, Part 1, by David Bernard Williams and C. Barry Carter.

[49] A. L. Efros and M. Rosen, "The electronic structure of semiconductor nanocrystals", Ann. Rev. Mater. Sci. **30**, 475-521 (2000)

[50] Z. Zanolli, M. E. Pistol, L. E. Fr ̈oberg, and L. Samuelson, "Quantum-confinement effects in InAs-InP core-shell nanowires", J. Phys.: Condens. Matter **19**, 295219 (2007)

[51] M. Tchernycheva, L. Travers, G. Patriarche, F. Glas, J. C. Harmand, G. E. Cirlin, and V. G. Dubrovskii, "Au-assisted molecular beam epitaxy of InAs nanowires: growth and theoretical analysis", J. Appl. Phys. **102**, 094313 (2007)

[52] S. A. Dayeh, E. T. Yu, and D. Wang, "Growth of InAs nanowires on SiO2 Substrates: nucleation, evolution, and the role of Au nanoparticles", J. Phys. Chem. C **111**, 13331 (2007)

[53] S. G. Ihn and J. I. Song, "InAs nanowires on Si substrates grown by solid source molecular beam epitaxy", Nanotechnology **18**, 355603 (2007)

[54] X. Zhang, J. Zou, M. Paladugu, Y. Guo, Y. Wang, Y. Kim, H. J. Joyce, Q. Gao, H. H. Tan, and C. Jagadish, "Evolution of epitaxial InAs nanowires on GaAs (111)B", Small **5**, 366-369 (2009)

[55] T. Akiyama, K. S. K. Nakamura, and T. Ito, "An empirical potential approach to wurtzite-zinc-blende polytypism in group III-V semiconductor nanowires", Jpn. J. Appl. Phys **45**, 275-278 (2006)

[56] K. Tomioka, J. Motohisa, S. Hara, and T. Fukui, "Crystallographic structure of InAs nanowires studied by transmission electron microscopy", Jpn. J. Appl. Phys. **46**, 1102-1104 (2007)

[57] A. I. Persson, L. E. Froberg, L. Samuelson, and H. Linke, "The fabrication of dense and uniform InAs nanowire arrays", Nanotechnology **20**, 225304 (2009)

[58] T. Mårtensson, J. B. Wagner, E. Hilner, A. Mikkelsen, C. Thelander, J. Stangl, B. J. Ohlsson, A. Gustafsson, E. Lundgren, L. Samuelson, and W. Seifert, "Epitaxial growth of indium arsenide nanowires on silicon using nucleation templates formed by self-assembled organic coatings", Adv. Mater. **19**, 1801-1806 (2007)

[59] V. G. Dubrovskii, and N. V. Sibirev, "Growth thermodynamics of nanowires and its application to polytypism of zinc blende III-V nanowires ", Phys. Rev. B **77**, 035414 (2008)

[60] M. Moewe, L. C. Chuang, V. G. Dubrovskii, and C. Chang-Hasnain, "Growth mechanisms and crystallographic structure of InP nanowires on lattice-mismatched substrates ", J. Appl. Phys. **104**, 044313 (2008)

[61] F. Glas, J. C. Harmand, and G. Patriarche, "Why does wurtzite form in nanowires of iii-v zinc blende semiconductors", Phys. Rev. Lett. **99,** 146101 (2007)

[62] V. G. Dubrovskii, N. V. Sibirev, J. C. Harmand, and F Glas, "Growth kinetics and crystal structure of semiconductor nanowires", Phys. Rev. B **78**, 235301 (2008)

[63] Z. F. Zanolli, F. G. Furthmüller, U. V. Barth, and F. Bechstedt, "Model GW band structure of InAs and GaAs in the wurtzite phase", Phys. Rev. B **75**, 245121 (2007)

[64] A. C. Ford, J. C. Ho, Y. L. Chueh, Y. C. Tseng, Z. Fan, J. Guo, J. Bokor, and A. Javey, "Diameter-dependent electron mobility of InAs nanowires", Nano Lett. **9**, 360-365 (2009)

[65] T. Tanaka, K. Tomioka, S. Hara, J. Motohisa, E. Sano, and T. Fukui, "Vertical surrounding gate transistors using single InAs nanowires grown on Si substrates," Appl. Phys. Exp. **3**, 025003 (2010)

[66] W. Wei, X. Bao, C. Soci, Y. Ding, Z. Wang, and D. Wang, "Direct heteroepitaxy of vertical InAs nanowires on Si substrates for broad band photovoltaics and photodetection", Nano Lett. **9**, 2926-2934 (2009)

[67] R. Gupta, Q. Xiong, G. D. Mahan, and P. C. Eklund, "Surface optical phonons in gallium phosphide nanowires", Nano Lett. **3**, 1745 (2003)

[68] L. C. Chuang, M. Moewe, C. Chase, N. P. Kobayashi, C. Chang-Hasnain, and S. Crankshaw, "Critical diameter for III-V nanowires grown on lattice-mismatched substrates", Appl. Phys. Lett. **90**, 043115 (2007)

[69] Z. M. Fang, K. Y. Ma, D. H. Jaw, R. M.Cohen, and G. B. Stringfellow, "Photoluminescence of InSb, InAs, and InAsSb grown by organometallic vapor phase epitaxy", J. Appl. Phys. **67**, 7034-7039 (1990)

[70] Y. Lacroix, C. A. Tran, S. P. Watkins, and M. L. W. Thewalt, "Low-temperature photoluminescence of epitaxial InAs", J. Appl. Phys. **80**, 6416-6424 (1996)

[71] R. D. Grober, H. D. Drew, J. I. Chyi, S. Kalem, and H. Morkoc, "Infrared photoluminescence of InAs epilayers grown on GaAs and Si substrates", J. Appl. Phys. **65**, 4079-4081 (1989)

[72] M. Fisher and A. Krier, "Photoluminescence of epitaxial InAs produced by different growth methods", Infrared Phys. & Tech. **38**, 405-413 (1997)

[73] B. Theys, A. Lusson, J. Ctievallier, C. Grattepain, S. Kalema, and M. Stutzmann, "Hydrogenation of InAs on GaAs heterostructures", J. Appl. Phys. **70**, 1461-1466 (1991)

[74] P. Gladkov, D. Nohavica, Z. Sourek, A. P. Litvinchunk, and M. N. Iliev, "Growth and characterization of InAs layers obtained by liquid phase epitaxy from Bi solvents", Semicond. Sci. Technol. **21**, 544-549 (2006)

[75] S. Ichikawa, N. Sanada, N. Utsumi, Y. Fukuda, "Surface structures and electronic states of clean and $(NH_4)_2S_x$-treated InAs (111) A and (111) B", J. Appl. Phys. **84**, 3658-3663 (1998)

[76] L. Ö. Olsson, C. B. M. Andersson, M. C. Håkansson, J. Kanski, L. Ilver, and U. O. Karlsson, "Charge accumulation at InAs surfaces," Phys. Rev. Lett. **76**, 3626-3629 (1996)

[77] M. Noguchi, K. Hirakawa, and T. Ikoma, "Intrinsic electron accumulation layers on reconstructed clean InAs(100) surfaces", Phys. Rev. Lett. **66**, 2243-2246 (1991)

[78] A. H. Chin, T. S. Ahn, H. Li, S. Vaddiraju, C. J. Bardeen, C. Z. Ning, and M. K. Sunkara, "Photoluminescence of GaN nanowires of different crystallographic orientations," Nano Lett. **7**, 626-631 (2007)

[79] W. Nakwaski, "Effective masses of electrons and heavy holes in GaAs, InAs, AlAs and their ternary compounds ", Physica B **210**, 1-25 (1995)

[80] G. E. Cirlin, V. G. Dubrovskii, I. P. Soshnikov, N. V. Sibirev, Yu. B. Samsonenko, A. D. Bouravleuv, J. C. Harmand, and F. Glas, "Critical diameters and temperature domains for MBE growth of III–V nanowires on lattice mismatched substrates", Phys. Status Solidi RRL **3**, 112-114 (2009)

[81] M. H. Sun, E. S. P. Leong, A. H. Chin, C. Z. Ning, G. E. Cirlin, Yu B. Samsonenko, V. G. Dubrovskii, L. Chuang, and C. Chang-Hasnain, "Photoluminescence properties of InAs nanowires grown on GaAs and Si substrates", Nanotechnology **21**, 335705 (2010)

[82] S. Song, W. Hong, S. Kwon, and T. Lee, "Passivation effects on ZnO nanowire field effect transistors under oxygen, ambient, and vacuum environments", Appl. Phys. Lett. **92**, 263109 (2008)

[83] T. Moon, M. Jeong, B. Oh, M. Ham, M. Jeun, W. Lee, and J. Myoung, "Chemical surface passivation of HfO_2 films in a ZnO nanowire transistor", Nanotechnology **17**, 2116 (2006)

[84] L. Shi, Y. Xu, S. Hark, Y. Liu, S. Wang, L. Peng, K. Wong, and Q. Li, "Optical and electrical performance of SnO_2 capped ZnO nanowire arrays", Nano Lett. **7**, 3559, (2007)

[85] E. C. Garnett and P. Yang, "Silicon nanowire radial p-n junction solar cells", J. Am. Chem. Soc. **130**, 9224 (2008)

[86] T. Hanrath and B. A. Korgel, "Chemical surface passivation of Ge nanowires", J. Am. Chem. Soc. **126**, 15466-15472 (2004)

[87] L. K. Vugt, S. J. Veen, E. P. A. M. Bakkers, A. L. Roest, and D. Vanmaekelbergh, "Increase of the photoluminescence intensity of InP nanowires by photoassisted surface passivation", J. Am. Chem. Soc. **127**, 12357 (2005)

[88] M. Dion źio Moreira, P. Venezuela, and T. M. Schmidt, "The effects of oxygen on the surface passivation of InP nanowires", Nanotechnology **19**, 065203 (2008)

[89] V. N. Bessolov and M. V. Lebedev, "Chalcogenide passivation of III–V semiconductor surfaces", Semiconductors **32**, 1141 (1998)

[90] C. J. Sandroff, R. N. Nottenburg, J. C. Bischoff, and R. Bhat, "Dramatic enhancement in the gain of a GaAs/AlGaAs heterostructure bipolar transistor by surface chemical passivation", Appl. Phys. Lett. **51**, 33 (1987)

[91] K. C. Hwang, S. S. Li, C. Park, and T. J. Anderson, "Schottky barrier height enhancement of n-$In_{0.53}Ga_{0.47}As$ by a novel chemical passivation technique", J. Appl. Phys. **67**, 6571 (1990)

[92] M. S. Carpenter, M. R. Melloch, M. S. Lundstrom, and S. P. Tobin, "Effects of Na_2S and $(NH_4)_2S$ edge passivation treatments on the dark current-voltage characteristics of GaAs pn diodes", Appl. Phys. Lett. **52**, 2157 (1988)

[93] T. Tamanuki, F. Koyama, and K. Iga, "Ammonium sulfide passivation for AlGaAs/GaAs buried heterostructure laser fabrication process", Jpn. J. Appl. Phys. **30**, 499 (1991)

[94] L. F. DeChiaro and C. J. Sandroff, "Improvements in electrostatic discharge performance of InGaAsP semiconductor lasers by facet passivation", IEEE Trans. Electron Devices ED **39**, 561 (1992)

[95] D. Y. Petrovykh, J. P. Long, and L. J. Whitman, "Surface passivation of InAs(001) with thioacetamide", Appl. Phys. Lett. **86**, 242105 (2005)

[96] T. Baum, Shen Ye, and Kohei Uosaki, "Formation of self-assembled monolayers of Alkanethiols on GaAs surface with in situ surface activation by ammonium hydroxide", Langmuir **15**, 8577 (1999)

[97] Q. Hang, F. Wang, P. D. Carpenter, D. Zemlyanov, D. Zakharov, E. A. Stach, W. E. Buhro, and D. B. Janes, "Role of molecular surface passivation in electrical transport properties of InAs nanowires", Nano Lett. **8**, 49-55 (2008)

[98] H. A. Budz, M. C. Biesinger, and R. R. LaPierrea, "Passivation of GaAs by octadecanethiol self-assembled monolayers deposited from liquid and vapor phases", J. Vac. Sci. Technol. B **27**, 637-648 (2009)

[99] W. Knoben, S. H. Brongersma, and M. Crego-Calama, "Preparation and characterization of octadecanethiol self-assembled monolayers on indium arsenide (100)", J. Phys. Chem. C **113**, 18331-18340 (2009)

[100] H. J. Joyce, J. Wong-Leung, Q. Gao, H. H. Tan, and C. Jagadish, "Phase perfection in zinc blende and wurtzite III−V nanowires using basic growth parameters", Nano Lett. **10**, 908-915 (2010)

[101] S. Adachi and D. Kikuchi, "Chemical etching characteristics of gaas(100) surfaces in aqueous hf solutions", J. Electrochem. Soc. **147**, 4618-4624 (2000)

[102] R. E. Alen, T. J. Humphreys, J. D. Dow, and O. F. Sankey, "Theory of surface defect states and Schottky barrier heights: application to InAs", J. Vac. Sci. Technol. B **2**,449-452 (1984)

[103] W. E. Spicer, P. W. Chye, P. R. skeath, C.Y. Su, and I. Lindau, "New and unified model for Schottky barrier and III–V insulator interface states formation", J. Vac. Sci. Technol. **16**, 1422-1433 (1979)

[104] Z. M. Fang, K. Y. Ma, D. H. Jaw, R. M. Cohen, and G. B. Stringfellow, "Photoluminescence of InSb, InAs, and InAsSb grown by organometallic vapor phase epitaxy", J. Appl. Phys. **67**, 7034-7040 (1990)

[105] H. A. Budz, M. C. Biesinger, and R. R. LaPierrea, "Passivation of GaAs by octadecanethiol self-assembled monolayers deposited from liquid and vapor phases ", J. Vac. Sci. Technol. B **27**, 637 (2009)

[106] D. Y. Petrovykh, J. C. Smith, T. D. Clark, R. Stine, L. A. Baker, and L. J. Whitman, "self-assembled monolayers of alkanethiols on InAs", Langmuir **25**, 12185-12194 (2009)

[107] T. Ohno and K. Shiraishi, "First-principles study of sulfur passivation of GaAs (001) surfaces", Phys. Rev. B **42**, 11194-11197 (1990)

[108] T. Ohno, "Sulfur passivation of GaAs surfaces", Phys. Rev. B **44**, 6306-6311 (1991)

[109] C. J. Spindt and W. E Spicer, "Sulfur passivation of GaAs surfaces: A model for reduced surface recombination without band flattening", Appl. Phys. Lett. **55**, 1653-1655 (1989)

[110] I. K. Han, E. K. Kim, J. I. Lee, S. H. Kim, K. N. Kang, Y. Kim, H. Lim, and H. L. Park, "Stability of sulfur-treated InP surface studied by photoluminescence and x-ray photoelectron spectroscopy", J. Appl. Phys. **81**, 6986-6892 (1997)

[111] S. D. Lester, T. S. Kim, and B. G. Streetman, "A proposed mechanism for radiative recombination through surface states on InP" J. Appl. Phys. 62, 2950 (1987)

[112] J. M. Moison and M. Bensoussan, "Surface recombination, surface states and Fermi level pinning", Revue Phys. Appl. **22**, 293-297 (1987)

[113] L. Geelhaar, R. A. Bartynski, F. Ren, M. Schnoes, and D. N. Buckley, "Photoluminescence and x-ray photoelectron spectroscopy study of S-passivated InGaAs(001)", J. Appl. Phys. **80**, 3076-3082 (1996)

[114] C. L. McGuiness, A. Shaporenko, C. K. Mars, S. Uppili, M. Zharnikov, and D. L. Allara, "Molecular self-assembly at bare semiconductor surfaces: preparation and characterization of highly organized octadecanethiolate monolayers on GaAs(001)", J. AM. Chem. Soc. **128**, 5231-5243 (2006)

[115] D. Y. Petrovykh, J. M. Sullivan, and L. J. Whitman, "Quantification of discrete oxide and sulfur layers on sulfur-passivated InAs by XPS", Surf. Interface Anal. **37**, 989-997 (2005)

[116] M. H. Sun, et al, "Recovery of Bandedge Emission of InAs Nanowires by Surface Passivation Using Octadecylthiol Self-Assembled Monolayer", in preparation

[117] H. Preier, "Recent advances in lead-chalcogenide diode lasers", Appl. Phys. A **20**, 189-206 (1979)

[118] Y. I. Ravich, B.A. Efimova, and I. A. Smirnov, "Semiconducting lead chalcogenides", Plenum Press, New York, 1970

[119] H. A. Washburn, J. R. Sites, and H. H. Wieder, "Electronic profile of *n*-InAs on semi-insulating GaAs", J. Appl. Phys. **50**, 4872-4878 (1979)

[120] Evan O. Kane, "Band structure of indium antimonide", J. Phys. Chem. Solids **1**, 249-261 (1957)

[121] J. Wu, W. Walukiewicz, W. Shan, K. M. Yu, J. W. Ager, III, E. E. Haller, H. Lu, and W. J. Schaff, "Effects of the narrow band gap on the properties of InN", Physical Review B **66**, 201403-201406 (2002)

[122] P. C. Findlay, C. R. PidgeonR. Kotitschke, A. Hollingworth, B. N. Murdin, C. J. G. M. Langerak, A. F. G. van der Meer, C. M. Ciesla, J. Oswald, A. Homer, G. Springholz, and G. Bauer, "Auger recombination dynamics of lead salts under picosecond free-electron-laser excitation", Phys. Rev. B **58**, 12908–12915 (1998)

[123] F. A. Junga, K. F. cuff, J. S. Blakemore, and E.R. Washwell, "Significance of band structure in determining radiative recombination and laser action in the lead salt semiconductors", Physics Letters B **13**, 103-105 (1964)

[124] A. R. Beattle and P. T. Landsberg, "Auger effect in semiconductor", Proc. R. Soc. Lond. A **249**, 16-29 (1958)

[125] R. Dalven, in "Solid State Physics", H. Ehrenreich, F. Seitz, D. Turnbull (eds.) New York: Academic Press, **28**, 179 (1973)

[126] H. Holloway and J.N. Walpole, "MBE techniques for IV-VI optoelectronic devices", Prog. Crystal Growth Charact. **2**, 49-94 (1979)

[127] Maurus Tacke, "Lead-salt lasers", Phil. Trans. R. Soc. Lond. A **359**, 547-566 (2001)

[128] J. F. Butler and A. R. Calawa, "PbS diode laser", J. Electrochem. Soc. **112**, 1056 (1965)

[129] R. W. Ralston, J. N. Walpole, A. R. Calawa, T. C. Harman, and J. P. McVittie, "High cw output power in stripe-geometry PbS diode lasers", J. Appl. Phys. **45**, 1323 (1974)

[130] A. Ishida, K. Muramatsu, K.Takashiba, and H. Fujiyasu, "$Pb_{1-x}Sr_xS$/PbS double-heterostructure lasers prepared by hot-wall expitaxy**"**, Appl. Phys. Lett. **55**, 430 (1989)

[131] K. Vilhelmsson, B. Valk, M. M. Salour, and T. K. Chu, "Optically pumped mode locked $PbS_{1-x}Se_x$ lasers", Appl. Phys. Lett. **50**, 807 (1987)

[132] N. Koguchi and S. Takahashi, "Double-heterostructure $Pb_{1-x-y}Cd_xSr_yS$/PbS/$Pb_{1-x-y}Cd_xSr_yS$ lasers grown by molecular beam epitaxy**",** Appl. Phys. Lett. **58**, 799 (1991)

[133] A. H. Chin, S. Vaddiraju, A. V. Maslov, C. Z. Ning, M. K. Sunkara, and M. Meyyappan "Near-infrared semiconductor subwavelength-wire lasers", App. Phys. Lett. **88**, 163115 (2006)

[134] X. Duan, Y. Huang, R. Agarwal, and C. M. Lieber, "Single-nanowire electrically driven lasers", Nature (London) **421**, 241 (2003)

[135] M. H. Huang, S. Mao, and H. Feick, H. Yan, Y. Wu, H. Kind, E. Weber, R. Russo, and P. Yang, "Room-Temperature Ultraviolet Nanowire Nanolasers", Science **292**, 1897-1899 (2001)

[136] A. V. Maslov and C. Z. Ning, "Modal gain in a semiconductor nanowire laser with anisotropic band structure", IEEE J. Quantum Electron. **40**, 1389 (2004)

[137] S. Y. Jang, Y. M. Song, et al., "Three synthetic routes to single-crystalline PbS nanowires with controlled growth direction and their electrical transport properties", ACS Nano **4,** 2391-2401 (2010)

[138] J. P. Ge, J. P. Ge, J. Wang, H. X. Zhang, X. Wang, Q. Peng, and Y. D. Li, "Orthogonal PbS nanowire arrays and networks and their raman scattering behavior", Chem. Eur. J. **11**, 1889-1894 (2005)

[139] I. Patla, S. Acharya, L. Zeiri, J. Israelachvili, S. Efrima, and Y. Golan, "Synthesis, two-dimensional assembly and surface pressure-indenced coalescence of ultranarrow PbS nanowires", Nano Lett. **7**, 1459-1462 (2007)

[140] M. J. Bierman, Y. K. Albert Lau, and S. Jin, "Hyperbranched PbS and PbSe Nanowires and the Effect of hydrogen gas on their synthesis", Nano Lett. **7**, 2907 (2007)

[141] M. Fardy, A. I. Hochbaum, J. Goldberger, M. M. Zhang, and P. Yang, "Synthesis and thermoelectrical characterization of lead chalcogenide nanowires", Adv. Mater. **19**, 3047-3051 (2007)

[142] M. J. Bierman, Y. K. Albert Lau, A. V. Kvit, A. L. Schmitt, and S. Jin, "Dislocation-driven nanowire growth and eshelby twist", Science **320**, 1060 (2008)

[143] Y. Wang, A.Suna, W. Mahler, and R. Kasowski, "PbS in polymers. From molecules to bulk solids", J. Chem. Phys. **87,** 7315 (1987)

[144] K. K. Nanda, F. E. Kruis, and H. Fissan, and S. N. Behera, "Effective mass approximation for two extreme semiconductors: Band gap of PbS and CuBr nanoparticles", J. App. Phys. **95**, 5015 (2004)

[145] A. Kreissl, Bohnertv, G. Lyssenk, and C. Klingshirn, "Experimenta1 investigation on the complex dielectric function of CdS in the exciton and in the plasma limit", Phys. Stat. Sol. (B) **114**, 637 (1982)

[146] Handbook of Optics, 2nd edition, Vol. 2. McGraw-Hill 1994

[147] J. C. Johnson, H. Yan, R. D. Schaller, L. H. Haber, R. J. Saykally, and P. Yang, "Single nanowire lasers", J. Phys. Chem. B **105** 11387-11390 (2001)

[148] M. H. Sun, et al. “Mid-Infrared Lead Sulfide Subwavelength-Wire Lasers Grown on Silicon Substrate”, in preparation

[149] H. Wang, M.H. Sun, K. Ding, M. T. Hill, and C. Z. Ning, “A top-down approach to fabrication of vertical InP and InGaAsP/InP heterostructrue nanowire arrays”, Nano Lett. **11**, 1646 (2011)

[150] L. C. Chuang, M. Moewe, S. Crankshaw, and C. Chang-Hasnain, “Optical properties of InP nanowires on Si substrates with varied synthesis parameters”, Appl. Phys. Lett. **92**, 013121 (2008)

[151] M. Mattila, T. Hakkarainen, M. Mulot, and H. Lipsanen, “Crystal-structure-dependent photoluminescence from InP nanowires”, Nanotechnology **17**, 1580 (2006)

[152] S. Bhunia, T. Kawamura and Y. Watanabe, S. Fujikawa, and K. Tokushima, “Metalorganic vapor-phase epitaxial growth and characterization of vertical InP nanowires”, Appl. Phys. Lett. **83**, 3371 (2003)

[153] M. Yoshimura, K. Tomioka, K. Hiruma, S. Hara, J. Motohisa, and T. Fukui, “Growth and characterization of InGaAs nanowires formed on GaAs(111)B by selective-area metal organic vapor phase epitaxy”, Jpn. J. Appl. Phys. **49**, 04DH08 (2010)

[154] Y. Kim, H. J. Joyce, Q. Gao, H. Hoe Tan, C. Jagadish, M. Paladugu, J. Zou, and A. Suvorova, “Influence of nanowire density on the shape and optical properties of ternary InGaAs nanowires”, Nano Lett. **6**, 599 (2006)

[155] M. Moewe, L.C. Chuang, S. Crankshaw, K.W. Ng, and C. Chang-Hasnain, “Core-shell InGaAs/GaAs quantum well nanoneedles grown on silicon with silicon-transparent emission”, Optical Express **17**, 7831 (2009)

[156] F. Jabeen, S Rubini, V Grillo, L. Felisari, and F. Martellib, “Room temperature luminescent InGaAs/GaAs core-shell nanowires”, Appl. Phys. Lett. **93**, 083117 (2008)

[157] A. Pan, L. Yin, Z. Liu, M. Sun, P. Nichols, and C. Ning, “Single-crystal erbium chloride silicate nanowires as a novel silicon based light emitting material at 1.53 μm”, submitted